Dissertation
submitted to the
Combined Faculty of Natural Sciences and Mathematics
of the Ruperto Carola University Heidelberg, Germany
for the degree of
Doctor of Natural Sciences

Presented by
M.Sc. Anna Schönrock
born in: Schwetzingen, Germany
Oral examination: 11.08.2021

Characterization of the transcription factor MEOX2 as a potential oncogene in gliomas

Referees:

Prof. Dr. Stefan Wiemann

Dr. Sevin Turcan, PhD

Declarations

I hereby declare that I have written and submitted the dissertation „Characterization of the transcription factor MEOX2 as a potential oncogene in gliomas“ myself and in this process have not used any other sources than those expressly indicated.

I hereby declare that I have not applied to be examinated at any other institution, nor have I used the dissertation in this or any other form at any other institution as an examination paper, nor submitted it to any other faculty as a dissertation.

Anna Schönrock

Contents

List of figures

List of tables

Abbreviations

ACT-seq	Antibody-guided Chromatin Tagmentation sequencing
ACTB	Actin
AKT	V-akt murine thymoma viral oncogene homolog
APS	Ammonium persulfate
ARID1A	AT-rich interactive domain-containing protein 1A
AS	Antisense
ATRX	Adenosine triphospate (ATP) dependent helicase
BBS9	Bardet-Biedl Syndrome 9
BCA	Bicinchoninic acid assay
bFGF	human recombinant fibroblast growth factor
BHLHE40	Basic Helix-Loop-Helix Family Member E40
BLI	Bioluminescence imaging
BSA	Bovine serum albumin
CDK	Cyclin-dependent kinase
CDKN2A	Cyclin-dependent kinase inhibitor 2A
CGGA	Chinese Glioma Genome Atlas
CIC	Capicua Transcriptional Repressor
CLSM	Confocal laser scanning microscopy
CLU	Clusterin
CNS	Central nervous system
CO	Cerebral organoids
CRISPR	Clustered Regularly Interspaced Short Palindromic Repeats
CTCF	Corrected total cell fluorescence
CUT&Tag sequencing	Cleavage Under Targets and Tagmentation sequencing
DAPI	4′,6-diamidino-2-phenylindole
DKFZ	German Cancer Research Center
DMEM	Dulbecco's Modified Eagle's medium
DMSO	Dimethylsulfoxid
DNA	Desoxyribonucleic acid
dsDNA	Double stranded DNA
DTT	Dithiothreitol
DUSP	Dual-specificity phosphatase
EB	Embryoid body
ECM	Extracellular matrix
EGF	Human recombinant epidermal growth factor
EGFLAM	EGF-like, fibronectin type-III and laminin G-like domain-containing protein
EGFR	Epithelial growth factor receptor
EMT	Epithelial-mesenchymal transition
ERK	Extracellular signal-regulated kinases
ETV	ETS transcription factor
F-actin	Filamentous actin

FBS	Fetal bovine serum
FUBP1	Far Upstream Element Binding Protein 1
GAPDH	Glyceraldehyde 3-phosphate dehydrogenase
GBM	Glioblastoma multiforme
GDP	Guanosin diphosphate
GIC	Glioma initiating cells
GP6	Glycoprotein VI
GTP	Guanosin triphosphate
H3	Histone 3
HEK293	Human embryonic kidney cells 293
HEK293TN	Human embryonic kidney cells 293 expressing SV40 large T antigen
HIF-1α	Hypoxia-inducible factor 1-alpha
HOTAIR	HOX Transcript Antisense RNA
HOX	Homeobox-related gene
HRP	Horseradish peroxidase
i.p.	Intraperitoneal injection
IDH	Isocytrat dehydrogenase
IF	Immunofluorescence
IgG	Immunoglobulin G
IHA	Immortalized human astrocytes
IHC	Immunohistochemistry
IP	Immunoprecipitation
IPA	Ingenuity pathway analysis
IPSC	Induced pluripotent stem cells
IRCCS	Istituto di ricovero e cura a carattere scientifico (Institute name)
KD	Knockdown
kDa	Kilodalton
KO	Knockout
LAP	Latency-associated peptide
LARS2	Leucyl-TRNA Synthetase 2, Mitochondrial
LB	Lysogeny broth
LGG	Lower grade glioma
LLC	Large latent complex
LOH	Loss of heterozygosity
LTBP	Latent Transforming Growth Factor Beta Binding Protein
MAP2	Microtubule Associated Protein 2
MAPK	Mitogen-activated protein (MAP) kinase
MDM	Mouse double minute
MEK	Mitogen-activated protein kinase kinase
MEOX2	Mesenchyme Homeobox 2
MRI	Magnetic resonance imaging
mRNA	Messenger RNA
MSKCC	Memorial Sloan Kettering Cancer Center
mTOR	Mechanistic target of rapamycin

mTORC	Mechanistic target of rapamycin complex
mV	Millivolt
Myf	Myogenic factor
MyoD	Myoblast determination protein 1
NCT	National Center for Tumor Diseases
NDRG1	N-Myc Downstream Regulated gene 1
NEAA	Non-essential amino acids
NF1	Neurofibromin 1
NRCAM	Neuronal Cell Adhesion Molecule
NSCLC	Non-small cell lung carcinoma
NTC	Non-targeting control
ODCF	Omics IT and data management core facility at DKFZ
OE	Overexpressed/overexpression
ON	Over night
p14(ARF)	Cyclin-dependent kinase inhibitor 2A
p16(INK4a)	Cyclin-dependent kinase inhibitor 2A
p21	Cyclin-dependent kinase inhibitor 1
p53	Tumor Protein 53
Pax3	Paired box gene 3
PB	phosphate buffer
PBS	Phosphate buffered saline
PCR	Polymerase chain reaction
PCV	Procarbazine, lomustine, vincristine
PDGFR	Platelet Derived Growth Factor Receptor
PDK1	Phosphoinositide-dependent kinase 1
PEG	Polyethylene glycol
PFA	Paraformaldehyde
PI3K	Phosphatidylinositol 3-kinase
PIP2	Phosphatidylinositol bisphosphate
PIP3	Phosphatidylinositol 3,4,5-triphosphate
PKB	Akt/protein kinase B
PTEN	Phosphatase and tensin homolog
pTPM	transcripts per million protein coding genes
qPCR	Quantitative polymerase chain reaction
RAS	Ras sarcoma
RB	Retinoblastoma
RICTOR	RPTOR Independent Companion Of mTOR Complex 2
RNA	Ribonucleic acid
RNA-seq	RNA sequencing
RNF10	RING finger protein 10
ROCK	Rho-associated protein kinase
RPGC	Reads per genome coverage
RPTOR	Regulatory Associated Protein Of mTOR Complex 1
RSEM	RNA-seq Expectation-Maximization

RT	Room temperature
RT	Room temperature
RTK	Receptor tyrosine kinase
s.c	Subcutan
S100A6	S100 Calcium Binding Protein A6
S155A	Serine at position 155 converted to Alanine at position 155
SDS	Sodium dodecyl sulfate
Ser	Serine
sg	Single guide
Snail	Snail Family Transcriptional Repressor
SNHG10	Small Nucleolar RNA Host Gene 10
SPRY	Sprouty
SWI/SNF complex	SWItch/Sucrose Non-Fermentable complex
TAGLN3	Transgelin 3
TCGA	The Cancer Genome Atlas
TEMED	Tetramethylethylenediamine
TERT	Telomerase Reverse Transcriptase
TGFB	Transforming growth factor beta
Thr	Threonin
TM4SF	Transmembrane 4 superfamily
TP53	Tumor Protein 53
TPM	Transcripts per million
Tween 20	Polysorbate 20
TWIST1	Twist Family BHLH Transcription Factor 1
Tyr204	Tyrosine 204
UTR	Untranslated region
v/v	Volume to volume
VEGF	Vascular endothelial growth factor
Vol%	Percent by volume
WHO	World Health Organisation
Wt	Wild type
xg	Number of times (x) the gravitational force (g)

Summary

Glioblastoma (GBM) is the most aggressive tumor of the central nervous system. Median survival time is 15 months from diagnosis. Standard of care for GBM patients includes surgery, radiation and chemotherapy. All known therapies for GBM patients do not lead to prolonged survival. Some targeted therapies can lead to a prolonged progression free survival. Overall survival of patients however is not increased by any available therapy option. MEOX2 is a homeobox-transcription factor. It is highly upregulated during embryogenesis and responsible for the development of muscles, angiogenesis and limb development. MEOX2 can regulate the epithelial-mesenchymal transition of cells via cyclin dependent kinase signaling. MEOX2 is not expressed in the adult brain tissue however is significantly upregulated in GBM and correlates with tumor grade. High MEOX2 expression in gliomas is generally correlated with a worse clinical prognosis for patients, underlining the potential role of MEOX2 in tumorigenesis. As current therapy options can not provide a cure for GBM, it is crucial to understand the role of MEOX2 and reveal candidates connected to the malignant transformation of gliomas for further investigations. In a lower grade progression free state, glioma could be treated like a chronic disease. Therefore, I identified *MEOX2* regulatory effect on cancer associated pathways and unraveled the target genes of MEOX2 in two GBM patient-derived tumorsphere lines. I also identified an ERK phosphorylation site in MEOX2 in the GBM tumorsphere line (S155) and elucidated the nuclear MEOX2 protein distribution depending on its phosphorylation status. I was also able to identify MEOX2 as an oncogene *in vivo*, using a xenograft mouse model where I observed increased proliferation upon MEOX2 overexpression in a GBM tumorsphere line that exhibits slower growth kinetics. Lastly, I observed MEOX2 knockdown in one of two GBM tumorsphere lines reduced sensitivity to EGF activated ERK phosphorylation that was reversed by a MEK inhibitor. All results indicate a role of MEOX2 as an oncogene in gliomas, and MEOX2 may serve as a future prognostic marker in gliomas. It is favourable to identify GBM in an early state which is currently not possible due to diagnosis based on MRI scans, this way GBM has a lower amount of lesions and accumulated mutations, which are gained in tumor development.

Zusammenfassung

Das Glioblastom (GBM) ist der aggressivste Tumor des zentralen Nervensystems. Die mediane Überlebenszeit beträgt 15 Monate ab Diagnose. Die Standardversorgung für GBM-Patienten umfasst Operation, Bestrahlung und Chemotherapie. Einige zielgerichtete Therapien können zu einem verlängerten progressionsfreien Überleben führen. Das Gesamtüberleben der Patienten wird jedoch durch keine verfügbare Therapieoption erhöht. MEOX2 ist ein Homöobox-Transkriptionsfaktor. Es wird während der Embryogenese stark hochreguliert und ist für den Muskelaufbau, die Angiogenese und die Entwicklung der Gliedmaßen verantwortlich. MEOX2 kann den epithelial-mesenchymalen Übergang von Zellen über cyclinabhängige Kinasen regulieren. MEOX2 wird im adulten Hirngewebe nicht exprimiert, ist jedoch in GBM signifikant hochreguliert und korreliert mit dem Tumorgrad von Gliomen. Eine hohe MEOX2-Expression bei Gliomen korreliert im Allgemeinen mit einer schlechteren klinischen Prognose für Patienten, was die potenzielle Rolle von MEOX2 bei der Tumorentstehung unterstreicht. Da die derzeitigen Therapieoptionen keine Heilung für GBM bieten können, ist es entscheidend, die Rolle von MEOX2 zu verstehen und potentielle Kandidaten für die Forschung an der malignen Transformation von Gliomen zu finden. In einem niedrigeren progressionsfreien Zustand könnte das Gliom wie eine chronische Krankheit behandelt werden. Daher identifizierte ich die regulatorische Wirkung von MEOX2 auf krebsassoziierte Signalwege und entschlüsselte direkte DNA Bindungspartner von MEOX2 in zwei von GBM-Patienten stammenden Tumorsphärenlinien. Ich habe auch eine ERK-Phosphorylierungsstelle in MEOX2 (S155) in einer GBM-Tumorsphärenlinie identifiziert, und die nukleäre MEOX2-Proteinverteilung in Abhängigkeit von ihrem Phosphorylierungsstatus aufgeklärt. Ich konnte MEOX2 auch *in vivo* als Onkogen identifizieren, indem ich ein Xenograft-Mausmodell verwendete, bei dem ich eine erhöhte Proliferation bei MEOX2-Überexpression in einer GBM-Tumorsphärenlinie beobachtete, die eine langsame Wachstumskinetik zeigt. Schließlich beobachtete ich, dass der MEOX2-Knockdown in einer von zwei GBM-Tumorsphärenlinien die Empfindlichkeit gegenüber EGF-aktivierter ERK-Phosphorylierung verringerte, die durch einen MEK-Inhibitor rückgängig gemacht wurde. Alle Ergebnisse weisen auf eine Rolle von MEOX2 als Onkogen bei Gliomen hin, und MEOX2 könnte als zukünftiger prognostischer Marker bei Gliomen dienen. Es ist vorteilhaft, GBM in einem frühen Stadium zu identifizieren, was aufgrund der Diagnose auf Basis von MRT-Scans derzeit nicht möglich ist, damit GBM eine geringere Anzahl von Läsionen und akkumulierten Mutationen aufweist, welche in der Tumorentwicklung akkumulieren.

1 Material and Methods

1.1 Material

1.1.1 Patient Material

We received fresh frozen tumor samples of GBM patients from Dr. K. Ozduman, Acibadem Maslak Hospital, Istanbul, Turkey. Samples were stored in liquid nitrogen until use.

1.1.2 Cell lines

1.1.2.1 Glioma initiating cells (GICs)

The primary GIC cultures TS667 and TS600 were kindly provided by the Chan Lab, MSKCC New York, USA. Each line has been modified using CRISPR/Cas9 single guide (sg) technique to knockdown (KD) the *MEOX2* gene, generating the lines TS667 sg1, TS667 sg2, TS667 NTC (non-targeting control), TS600 sg1, TS600 sg2, TS600 NCT.

The primary GIC cultures 080125 and 080512 were kindly provided by Rosella Galli, IRCCS Ospedale San Raffaele, Milan, Italy. Each line has been modified to overexpress *MEOX2* or control plasmid to generate the following lines: 080125 MEOX2, 080125 control, 080512 MEOX2 and 080512 control. All of these lines were engineered to overexpress luciferase for *in vivo* experiments.

1.1.2.2 Non-tumor cell lines

Human embryonic kidney cells (HEK293) and human embryonic kidney cells with a SV40 promoter (HEK293TN) were kindly provided by the Chan Lab, MSKCC New York, USA. Immortalized human astrocytes (IHA) were kindly provided by the Chan Lab, MSKCC New York, USA. For cerebral organoid experiments, Human CD34+ umbilical cord blood cell derived induced pluripotent stem cells (IPSC) were purchased from Lonza by the Mall lab at DKFZ.

Table 1: Modified and parental cell lines

Cell line	**Description**
TS667	Parental line
TS667 sg1	*MEOX2* KD cell line, transduced with lentiCRISPR v2-MEOX2-sg1 plasmid
TS667 sg2	*MEOX2* KD cell line, transduced with lentiCRISPR v2-MEOX2-sg2 plasmid
TS667 NTC	Non-targeting control cell line, transduced with lentiCRISPR v2-NTC

TS667 sg1 Luciferase	*MEOX2* KD and luciferase OE cell line, transduced with lentiCRISPR v2-MEOX2-sg1 plasmid and pLenti-PGK-V5-LUC Neo
TS667 sg2 Luciferase	*MEOX2* KD and luciferase OE cell line, transduced with lentiCRISPR v2-MEOX2-sg2 plasmid and pLenti-PGK-V5-LUC-Neo
TS667 NTC Luciferase	Non-targeting control and luciferase OE cell line, transduced with lentiCRISPR v2-NTC and pLenti-PGK-V5-LUC Neo
TS600	Parental line
TS600 sg1	*MEOX2* KD cell line, transduced with lentiCRISPR v2-MEOX2-sg1 plasmid
TS600 sg2	*MEOX2* KD cell line, transduced with lentiCRISPR v2-MEOX2-sg2 plasmid
TS600 NTC	Non-targeting control cell line, transduced with lentiCRISPR v2-NTC
TS600 sg1 Luciferase	*MEOX2* KD and luciferase OE cell line, transduced with lentiCRISPR v2-MEOX2-sg1 plasmid and pLenti-PGK-V5-LUC Neo
TS600 sg2 Luciferase	*MEOX2* KD and luciferase OE cell line, transduced with lentiCRISPR v2-MEOX2-sg2 plasmid and pLenti -PGK-V5-LUC
TS600 NTC Luciferase	Non-targeting control and luciferase OE cell line, transduced with lentiCRISPR v2-NTC and pLenti-PGK-V5-LUC -LUC Neo
080125	Parental line
080125 MEOX2	*MEOX2* OE cell line, transduced with pLVX-puro-MEOX2-FLAG
080125 control	Control cell line, transduced with pLVX-puro
080125 MEOX2 Luciferase	*MEOX2* and luciferase OE cell line, transduced with pLVX-puro-MEOX2-FLAG and pLenti-PGK-V5-LUC Neo
080125 control Luciferase	Luciferase OE control cell line, transduced with pLVX-puro and and pLenti-PGK-V5-LUC Neo
080512	Parental line
080512 MEOX2	*MEOX2* OE cell line, transduced with pLVX-puro-MEOX2-FLAG
080512 control	Control cell line, transduced with pLVX-puro
080512 MEOX2 Luciferase	*MEOX2* OE and luciferase OE cell line, transduced with pLVX-puro-MEOX2-FLAG and pLenti-PGK-V5-LUC Neo
080512 control Luciferase	Luciferase OE control cell line, transduced with pLVX-puro and and pLenti-PGK-V5-LUC Neo
HEK293	Parental line
HEK293 MEOX2 Flag	*MEOX2* and Flag OE cell line, transiently transfected with pLVX-puro-MEOX2-FLAG

HEK293 MEOX2 S155A Flag	*MEOX2 S155A* and Flag OE cell line, transiently transfected with pLVX-puro-MEOX2-S155A-FLAG
HEK293 control	Control cell line, transiently transfected with pLVX puro
HEK293TN	Parental line
HEK293TN MEOX2 Flag	*MEOX2* and Flag OE cell line, transiently transfected with pLVX-puro-MEOX2-FLAG
HEK293TN MEOX2 S155A Flag	*MEOX2 S155A* and Flag OE cell line, transiently transfected with pLVX-puro-MEOX2-S155A-FLAG
HEK293TN control	Control cell line, transiently transfected with pLVX puro
IHA	Parental line
IHA MEOX2	*MEOX2* OE cell line, transiently transfected with pLVX-puro-MEOX2
IHA control	Control cell line, transiently transfected with pLVX puro
IPSC	Parental line

1.1.3 Cell culture media and supplements

GIC lines were cultured as tumorspheres using ultralow attachment flasks and NeuroCult NS-A Proliferation Kit (STEMCELL technologies) medium supplemented with 2 mg/mL heparin (STEMCELL technologies), 20 ng/mL human recombinant epidermal growth factor (EGF, STEMCELL technologies) and 20 ng/mL human recombinant fibroblast growth factor (bFGF, STEMCELL technologies). Medium was changed once per week. TS600 were additionally incubated for 5 min in Accutase, after centrifugation, to separate tumorspheres. HEK293, HEK293TN and IHA cell lines were cultured in coated flasks and DMEM high glucose (Sigma-Aldrich) medium supplemented with 10% (v/v) Fetal Bovine Serum (Sigma-Aldrich). Medium was changed once per week. Cells were incubated in Accutase for 5 min, after removing old medium and washing once using PBS, to collect attached cells. IPSCs were treated with TripleLE dissociation reagent to obtain single cells and were plated in ultra-low-binding 96-well plates in mTeSR™1 medium containing Rho-associated protein kinase (ROCK) inhibitor (1:200). The mTeSR™1 medium was changed every day and once the embryoid bodies (EB) reached a diameter size of around 500 µm, medium was replaced by cortical induction medium. After three days, EBs, now induced to form cerebral organoids (COs), were pooled into a 6 cm dish containing fresh cortical induction medium. Nucleofected COs were embedded into Geltrex and transferred to a low-attachment 6 cm dish containing cortical induction medium and incubated at 37 °C. One day after embedding, COs were transferred to the orbital shaker.

From the following day, medium was replaced by differentiation medium with regular medium change every three to four days. Organoids were cultured for four weeks until analysis.

1.1.4 Animals

Female arythmic nude mice were kept at the central animal facility of the German Cancer Research Center Heidelberg under 12/12 hour light-dark cycle conditions. Food and water were offered *ad libitum*.

1.1.5 Reagents

Table 2: Reagents

Name	**Company**
2-Mercaptoethanol	Sigma-Aldrich
2-Propanol	Sigma-Aldrich
A83-01	StemGent
Accutase solution	Biolegend
Acrylamide (30%)	Bio-Rad
Agarose	Carl Roth
Ampicillin	Carl Roth
Ampure Beads	Beckman Coulter
APS	Bio-Rad
B27 Supplement	Gibco
Bepanthen eyecream	Beyer
bFGF	STEMCELL technologies
Bovine Serum Albumin (BSA)	Carl Roth
Bromphenol blue	Carl Roth
Bupivacain	Jenapharm
Carprofen (Rimadyl)	Zoetis
Cell-dissociation reagent (TrypLE Express)	Gibco
Chloroform	Clinic Pharmacy, Heidelberg University Clinic
Cyclic adenosine monophosphate (cAMP)	Sigma-Aldrich

Cycloheximide	Selleckchem
D-Glucose	Carl Roth
Dithiothreitol (DTT)	Carl Roth
DMEM high glucose	Sigma-Aldrich
DMEM-F12 L-Glutamin	Gibco
DMSO	Carl Roth
Donkey serum	Sigma-Aldrich
Dulbecco's Phosphate Buffered Saline (PBS)	Sigma-Aldrich
ECL Western Blotting Substrate	Thermo Fisher
EGF	STEMCELL technologies
Embedding molds (Tissue-Tek Cryomold)	Sakura Finetek
Erlotinib	Selleckchem
Esp3I	NEB
Ethanol	Sigma-Aldrich
Fetal Bovine Serum	Sigma-Aldrich
Formaldehyde	Carl Roth
FuGene	Promega
Galunisertib	Selleckchem
Geltrex	Gibco
Geneticin®	Gibco
Glucose	Carl Roth
Glycerin	Carl Roth
Glycerol	Carl Roth
Glycin	Carl Roth
Heparin	STEMCELL technologies
HEPES	Sigma-Aldrich
Hyperactive pA-MNase for CUT&RUN	Vazyme
Hyperactive pG-Tn5 Transposase for CUT&Tag	Vazyme
Inhibitor of WNT response (IWR-1)	Enzo Life Science

Insulin	Sigma-Aldrich
KCl	Carl Roth
Ketamin	Zoetis
KH2PO4	Carl Roth
L-alanyl-L-glutamine (GlutaMax)	Gibco
Laminin	Corning
LB Agar	Carl Roth
LB Medium	Carl Roth
LDN-193189	Miltenyi Biotec
Luciferin in vivo grade	Promega
Mercaptoethanol	Bio-Rad
Methanol	Sigma-Aldrich
Midori Green	Nippon Genetics Europe GmbH
Milk powder	Carl Roth
mTeSR™1 medium	STEMCELL technologies
N2 Supplement	Gibco
Na2HPO4	Carl Roth
Na2HPO42H2O	Carl Roth
NaCl	Carl Roth
NaH2PO4H2O	Carl Roth
NaOH	Carl Roth
NEAA	Thermo Fisher
Non-essential amino acids	Gibco
NP40 buffer	Thermo Fisher
Opti-Mem	Gibco
Paraformaldehyd (PFA)	Sigma Aldrich
PEG	Carl Roth
Pierce Protein A/G Magnetic Beads	Thermo Fisher
Plastic paraffin film (Parafilm)	BRAND GMBH + CO KG
Powdered milk	Carl Roth

Puromycin (100 mg/mL)	Invivogen
PVDF membrane	Merck Millipore
Restore PLUS Western Blot-Stripping-Buffer	Thermo Fisher
ROCK inhibitor Y-27632	Cell Guidance Systems
Sodium dodecyl sulfate (SDS)	Carl Roth
Sodiumchoride (NaCl)	Sigma-Aldrich
Sucrose	Sigma-Aldrich
T4 ligase	NEB
T4 ligation buffer	NEB
T4 PNK	NEB
Tetramethylethylenediamine (TEMED)	Carl Roth
Tissue-Tek® O.C.T.™ Compound	Sakura
Trametinib	Selleckchem
Tris	Carl Roth
Triton X-100	AppliChem
TRIzol	Thermo Fisher
Trypan Blue Stain (0,4%)	Gibco
Tween 20	Carl Roth
Xylazin	Bayer

1.1.6 Bacteria

Table 3: Competent bacteria

Name	**Company**
Stable3	Thermo Fisher

1.1.7 Plasmids

Table 4: Plasmids

Name	Vector type	Provider
PB-linker-CAG_MCS_T2A_mNeonGreen	mammalian expression	Mall Lab, DKFZ
PB-linker-CAG_MCS_T2A_MEOX2_mNeonGreen	mammalian expression	A. Schönrock, Turcan Lab, NCT
PB-Transposase	mammalian expression	Mall Lab, DKFZ
lentiCRISPRv2-hNF1	lentivirus	Mall Lab, DKFZ
lentiCRISPRv2-hPTEN	lentivirus	Mall Lab, DKFZ
lentiCRISPRv2-hp53	lentivirus	Mall Lab, DKFZ
lentiCRISPRv2-B3	lentivirus	Mall Lab, DKFZ
pLVX-puro	lentivirus	Chan Lab, MSKCC
pLVX-puro-MEOX2	lentivirus	A. Schönrock, Turcan Lab, NCT
pLVX-puro-MEOX2-FLAG	lentivirus	A. Schönrock, Turcan Lab, NCT
pLVX-puro-MEOX2-S155A-FLAG	lentivirus	A. Schönrock, Turcan Lab, NCT
pLenti-PGK-V5-LUC Neo	lentivirus	Addgene #21471
lentiCRISPRv2	lentivirus	Addgene #52961
lentiCRISPRv2-MEOX2-sg1	lentivirus	A. Schönrock, Turcan Lab, NCT
lentiCRISPRv2-MEOX2-sg2	lentivirus	A. Schönrock, Turcan Lab, NCT
lentiCRISPRv2-NTC	lentivirus	A. Schönrock, Turcan Lab, NCT
pCMV-dR8.2 dvpr	lentivirus	Addgene #8455
pCMV-VSV-G	lentivirus	Addgene #8454
rwpLX305-MEOX2-IRES-GFP	mammalian expression	Rainer Will

1.1.8 CRISPR/Cas9 single guide sequences

Table 5: CRISPR/Cas9 single guides

Target	Name	Top oligo sequence	Bottom oligo sequence
MEOX2	sg1	CACCgtcccgcgattatgcaagatg	AAACcatcttgcataatcgcgggaC
MEOX2	sg2	CACCgtgtgccgagccgcactcggt	AAACaccgagtgcggctcggcacaC
Non-targeting control	NTC	CACCgtattactgatattggt	AAACaccaatatcagtaataC
hNF1	hNF1	CACCgctcgtcgaagcggctgacca	AAACtggtcagccgcttcgacgagC
hPTEN	hPTEN	CACCgaacttgtcttcccgtcgtgt	AAACacacgacgggaagacaagttC
hp53	hp53	CACCgtcgacgctaggatctgactg	AAACcagtcagatcctagcgtcgaC
Nontargeting control	control	CACCgcgcccgtttatgtggctacc	AAACggtagccacataaacgggcgC

1.1.9 MEOX2 amino acid sequence

Table 6: MEOX2 amino acid sequence

Target	Sequence
MEOX2	ATGGAACACCCGCTCTTTGGCTGCCTGCGCAGCCCTCACGCCACGGCGCAAGGCT TGCACCCGTTCTCCCAATCCTCTCTCGCCCTCCATGGAAGATCTGACCATATGTCT TACCCCGAGCTCTCTACTTCTTCCTCATCTTGCATAATCGCGGGATACCCCAACGA AGAGGGCATGTTTGCCAGCCAGATCACAGGGGGCACCACCACCACCACCACCAC CACCACCATCACCACCATCAGCAGCAGCAGCACCAGGCTCTGCAAACCAACTGGC ACCTCCCGCAGATGTCTTCCCCACCGAGTGCGGCTCGGCACAGCCTCTGCCTCCA GCCCGACTCTGGAGGGCCCCCAGAGTTGGGGAGCAGCCCGCCCGTCCTGTGCTCC AACTCTTCCAGCTTGGGCTCCAGCACCCCGACTGGGGCCGCGTGCGCGCCGGGGG ACTACGGCCGCCAGGCACTGTCACCTGCGGAGGCGGAGAAGCGAAGCGGCGGCA AGAGGAAAAGCGACAGCTCAGACTCCCAGGAAGGAAATTACAAGTCAGAAGTCA ACAGCAAACCCAGGAAAGAAAGGACAGCATTTACCAAAGAGCAAATCAGAGAAC TTGAAGCAGAATTTGCCCATCATAATTATCTCACCAGACTGAGGCGATACGAGAT AGCAGTGAATCTGGATCTCACTGAAAGACAGGTGAAAGTCTGGTTCCAAAACAG GCGGATGAAGTGGAAGAGGGTAAAGGGTGGACAGCAAGGAGCTGCGGCTCGGG AAAAGGAACTGGTGAATGTGAAAAAGGGAACACTTCTCCCATCAGAGCTGTCGG GAATTGGTGCAGCCACCCTCCAGCAAACAGGGGACTCTATAGCAAATGAAGACA GTCACGACAGTGACCACAGCTCAGAGCATGCGCACTTATGA

1.1.10 Primers

Table 7: Primers for cloning

Target	Forward sequence	Reverse sequence	Restrictionenzymes
MEOX2-FLAG amplification from: rwpLX305-MEOX2-IRES-GFP cloned into: pLVX puro	5'TAAGCACTCG AGatggaacacccgctc tttggc 3'	5'tgcttaGGATCCttatttgtcatc gtcgtccttgtagtctaagtgcgcatgct ctga 3'	Xho1, BamHI
MEOX2 amplification from: rwpLX305-MEOX2-IRES-GFP cloned into: pLVX puro	5'TAAGCACTCG AGatggaacacccgctc tttggc3'	5'tgcttaGGATCCtaagtgcgca tgctctga3'	Xho1, BamHI
MEOX2 amplification from: rwpLX305-MEOX2-IRES-GFP cloned into: PiggyBac-linker-CAG-MCS-t2a-mneongreen	5'TAAGCACTCG AGatggaacacccgctc tttggc3'	5'tgcttaGGATCCtaagtgcgca tgctctga3'	Xho1, BamHI
Pointmutation of S155A in pLVX-puro-MEOX2-FLAG	5'CCGCCAGGCA CTGGCACCTGC GGAGGC 3'	5'GCCTCCGCAGGTGCC AGTGCCTGGCGG 3'	

Table 8: qPCR primer

Target	Forward sequence	Reverse sequence	Company
MEOX2	GCACCCGTTCTCCCAATCC	TCCCGCGATTATGCAAGATGA	Integrated DNA Technologies, Inc. (IDT)
18s	ACCCGTTGAACCCCATTCGTGA	GCCTCACTAAACCATCCAATCGG	

1.1.11 Antibodies

Table 9: Primary and secondary antibodies

Target	Source	Dilution	Company	Order no.	Method
Primary antibodies					
MEOX2	Rabbit	1:1000, 10 µg / 450 µL (IP)	Atlas Antibodies	HPA053793	Western Blot, IP, ACT-seq, IF
Phospho MAPK (Erk1/2) (Thr202/Tyr204)	Rabbit	1:2000	Cell Signaling	#9101	Western Blot
MAPK (Erk1/2)	Mouse	1:2000	Cell Signaling	#9107	Western Blot
P21	Rabbit	1:2000	Cell Signaling	#2947	Western Blot

GAPDH	Rabbit	1:2000	Cell Signaling	#2118	Western Blot
Actin	Rabbit	1:2000	Cell Signaling	#4967	Western Blot
H3	Rabbit	1:10000	Cell Signaling	#9715	Western Blot
Rabbit IgG	Rabbit	10 µg / 450 µL (IP)	Merck Millipore	PP64	IP, ACT-seq
Secondary antibodies					
Alexa Fluor 488	Donkey	2 µg/mL	Thermo Fisher	A-21206	IF
Alexa Fluor 594	Donkey	2 µg/mL	Thermo Fisher	A-21207	IF
Anti-mouse	Horse	1:5000	Cell Signaling	#7076	Western Blot
Anti-rabbit	Goat	1:5000	Cell Signaling	#7074	Western Blot

1.1.12 Buffers and solutions

Table 10: Buffers and solutions

Solution	**Composition**
Antibody Dilution Buffer (IF)	1 % (w/v) BSA, 1 % (v/v) donkey serum, 0,3 % (v/v) Triton X–100 in PBS
Blocking Buffer (IF)	10 % (v/v) donkey serum, 0,3 % (v/v) Triton X–100 in PBS
Blocking Buffer (Western Blot)	5 % (w/v) milk powder in TBS-T
Complex Formation Buffer, 4 x (ACT-seq)	2 mL Tris 1 M pH 7,5, 1,5 mL NaCl 4 M, 200 µL Triton X-100 10 %, 5 mL glycerol 100 %, 1,3 mL H_2O
Cortical induction medium, 100 mL (cerebral organoids)	96 mL DMEM-F12, 500 µL N2 (1:200), 1 mL B27 (1:100), 200 µL Glucose (0,2 mg/mL), 15 µL cAMP (0,15 µg/mL), 500 µL NEAA (0,5%), 1 mL Glutamaxx (0,5 %), 18 µL LDN (180 nM), 50 µL A83 (500 nM), 100 µL Wnt-Inhibitor (10 µg/mL), 1 mL Heparin (10 µg/mL)
Differentiation medium, 100 mL (cerebral organoids)	96,7 mL DMEM-F12, 500 µL N2 (1:200), 1 mL B27 (1:100), 200 µL Glucose (0,2 mg/ mL), 15 µL cAMP (0,15 µg/mL), 500 µL NEAA (0,5 %), 1 mL Glutamaxx (0,5 %), 40 µL Insulin (2,5 µg/mL)
Elution Buffer (IP)	0,1 M Glycine, pH 2,0
Lysis Buffer (Western Blot) 4 x	4 mL Glycerol, 3,2 mL of 1 M Tris pH 6,8, 4 mg Bromphenolblue, 0,8 g SDS, Volume: 10 mL, fill up with H_2O, dilute 1:4 and add 200 µL Mercaptoethanol / 4 mL of 1 x Lysis Buffer

PFA 8 % (cardiac perfusions)	500 mL H_2O at 60° C, 40 g Formaldehyde, 2 drops 10 N NaOH, filter at 0,22 µm, store at 4° C
PFA 4 % (cardiac perfusions)	500 mL PFA 8 %, 500 mL Phosphate Buffer 0,2 M
Phosphat Buffer 0,2 M (cardiac perfusions)	35,61 g $Na_2HPO_42H_2O$ in 1000 mL H_2O, 27,6 g $NaH_2PO_4H_2O$ in 1000 mL H_2O, mix 770 mL of $Na_2HPO_42H_2O$ and 230 mL $NaH_2PO_4H_2O$, pH 7,3
Neutralization Buffer (IP)	1 M Tris, pH 7,5-9
Phosphate buffered saline (PBS)	137 mM NaCl, 2,7 mM KCl, 9,2 mM Na_2HPO_4, 1,8 mM KH_2PO_4, pH 7,4
SDS Gel 10%	Stacking gel, 10 mL (4 gels): 6,8 mL H_2O, 1,7 mL acrylamide 30 %, 1,25 mL Tris 1 M pH 6,8, 100 µL SDS 10 %, 100 µL APS, 10 µL TEMED Separating gel, 40 mL (4 gels): 19,8 mL H_2O, 16,7 mL acrylamide 30 %, 1,5 mL Tris 1 M pH 8,8, 500 µL SDS 10 %, 500 µL APS, 20 µL TEMED
SDS Page running Buffer 10 x	60,6 g TRIS, 288,2 g Glycin, 20 g SDS, Volume: 2 L, fill up with H_2O, dilute 1:10 for 1 x concentration
Transfer Buffer (Western Blot)	72 g TRIS, 345,6 g Glycin, Volume: 2 L, fill up with H_2O, dilute 1:10 in 20 % (v/v) Methanol and 80 % H_2O for 1 x concentration
Tris-buffered Saline (TBS) 20 x	121 g TRIS, 175,2 g NaCl, Volume: 1 L, fill up with H_2O, pH 7,4, dilute 1:20 for 1 x concentration
Tris-buffered Saline-Tween (TBS-T)	500 mL 20 x TBS, 10 mL Tween 20, Volume: 10 L, fill up with H_2O
Virus precipitation solution	40 g PEG-8000, 7 g NaCl, 40 mL H_2O, 10 mL PBS, pH 7, Volume: 100 mL, fill up with H_2O, sterile filter using 22 µM filter
Wash Buffer, 10 mL (ACT-seq)	500 µL Tris 1 M pH 7,5, 386 µL NaCl 4 M, 50 µL Triton X-100 10 %, 9,064 mL H_2O
Wash Buffer (IF)	0,1 % (w/v) BSA in PBS
Wash Buffer (IP)	0,05 % (v/v) Tween20 in TBS

1.1.13 Ready-to-use premixes

Table 11: Ready-to-use premixes

Name	Company
4x Laemmli loading Buffer	Bio-Rad
6 x loading dye	NEB
Antifade Mounting Medium with DAPI	VECTASHIELD®
Halt Protease und Phosphatase Inhibitor Cocktail (100x)	Thermo Fisher
Page Ruler prestained protein marker	NEB
RNAzap	Thermo Fisher
SYBR™ Green PCR-Mastermix	Thermo Fisher
TAE electrophoresis buffer	Thermo Fisher

1.1.14 Kits

Table 12: Kits

Name	Company
Alt-R® Genome Editing Detection Kit	Integrated DNA Technologies, Inc. (IDT)
BCA Protein Assay	Thermo Fisher
Cell Proliferation Kit I (MTT)	Roche
Hyperactive In-Situ ChIP Library Prep Kit for Illumina（pG-Tn5)	Vazyme
iScript cDNA Synthesis Kit	Bio-Rad
Kappa Hi Fi Hotstart ReadyMix	Roche
NeuroCult NS-A Proliferation Kit	STEMCELL technologies
Nucleofector™ P3 Primary Cell 4D X_KitS (32 RCT)	Lonza
QIAprep Spin Miniprep Kit	Qiagen
QIAquick Gel Extraction Kit	Qiagen
QIAquick PCR Purification Kit	Qiagen
QuikChange Site-Directed Mutagenesis Kit	Agilent
RNeasy RNA Isolation kit	Qiagen
The Quick Ligation™ Kit	NEB

1.1.15 Equipment and devices

Table 13: Equipment and devices

Name	Company
4D-Nucleofector Core Unit, Fl1	Lonza
4D-Nucleofector X Unit, FL1	Lonza
Bioanalyzer	Agilent
Cell culture hood	Thermo Fisher
Cell incubator	Thermo Fisher
Centrifuge	Thermo Fisher
ChemiDoc XRS+ Gel Imaging System	Bio-Rad
CLSM Microscope	Leica
Cryotom	Thermo Fisher
Dissecting utensils set	Carl Roth
Electrophoresis chamber	Carl Roth
Hamilton syringe	Hamilton
Heatblock	Eppendorf
iBlot 2 Dry Blotting System	Thermo Fisher
Incubator	Binder
Induction chamber	Stoelting
Infinite® 200 PRO plate reader	Tecan
Isoflurane pump	Stoelting
IVIS luminescence imager	PerkinElmer
Luna Cell Counter	Logos Biosystems
Magnetic stand	3D printed
Microscope	Zeiss
Mini-PROTEAN® Tetra electrophoresis wet blot system	Bio-Rad
NanoDrop	Thermo Fisher
NucleofectorTM X-Unit	Lonza
Orbital shaker Taumelschüttler TL10	Thermo Fisher Scientific
Peristaltic pump	Instech

Pipettes	Eppendorf
qPCRLightCycler	Roche
Stereotactic frame	Stoelting
Table top centrifuge	Thermo Fisher
Tapestation	Agilent
Thermal cycler	Biometra

1.1.16 Consumables

Table 14: Consumables

Name	**Company**
BioMasher tubes	TaKaRa®
Cannulaes	B. Braun Melsungen AG
Cell culture dishes (⌀10 cm)	Greiner Bio-One GmbH, Frickenhausen, Germany
Cell culture flasks (25cm^2, 75 cm^2, 175 cm^2)	Greiner Bio-One GmbH, Frickenhausen, Germany
Cell culture plates (6-, 12-, 24-, 96-well)	Greiner Bio-One GmbH, Frickenhausen, Germany
Cell scraper	TPP Techno Plastic Products AG, Trasadingen, Schweiz
Cellcounting slides	Logos Biosystems
Class cover slips	Th. Geyer
Cryovials	Greiner Bio-One GmbH, Frickenhausen, Germany
Hamilton syringe	Hamilton Company, Reno, Nevada, USA
Low-adhesion 6 cm plates	Labomedic
Object slides SuperFrost Plus™	Thermo Fisher Scientific
Pipette filter tips	STARLAB
Pipette tips	STARLAB
PVDF membrane	Merck, Darmstadt, Germany
Reaction tubes (1,5 mL, 2 mL)	Eppendorf AG
Reaction tubes (15 mL, 50 mL)	Corning
Reagent reservoirs	Corning
Serological pipettes (5 mL, 10 mL, 25 mL)	Greiner Bio-One GmbH, Frickenhausen, Germany

Stericup filter (0,22 µM)	Merck-Millipore
Sterile filters (0,22 µM, 0,45 µM)	Merck-Millipore
SuperFrost™ cover slides	Thermo Fisher
Syringes	B. Braun Melsungen AG

1.1.17 Software and databases

Table 15: Software and databases

Name	**Company**
Central Brain Tumor Registry of the United States (CBTRUS)	https://cbtrus.org/cbtrus-fact-sheet-2020/
Chinese Glioma Genome Atlas (CGGA) Database	http://www.cgga.org.cn
Genotype-Tissue Expression (GTEx) Portal	https://www.gtexportal.org/home/
GPP sgRNA Design tool, Broad institute	https://portals.broadinstitute.org/gpp/public/analysis-tools/sgrna-design
GraphPad Prism 6	GraphPad Software Inc., La Jolla, CA, USA
FIJI	http://fiji.sc/
ImageJ	http://imagej.nih.gov./ij/
Ingenuity Pathway Analysis	Qiagen
Integrative Genomics Viewer (IGV)	https://software.broadinstitute.org/software/igv/home
Leica Las X software	Leica
Microsoft Office	Microsoft Corporation, Redmond, WA, USA
PubMed	http://www.ncbi.nlm.nih.gov/pubmed
R	http://r-statistics.com
The Cancer Genome Atlas (TCGA) Database 2013	http://cancergenome.nih.gov/
The Human Protein Atlas	https://www.proteinatlas.org

1.2 Methods

1.2.1 Cell culture

1.2.1.1 GIC

TS667, TS600, TS543, 080125, 080512 cell lines and hNSC were kept under standard conditions at 37°C and 5% CO_2. They were cultured as spheroids in neural stem cell medium. EGF and bFGF growth factors were supplemented fresh with each medium change. TS600, 080125, 080512 were dissociated using accutase solution for 5 minutes at 37°C.

1.2.1.2 Non-tumor cell culture

HEK293TN, HEK293, IHA were cultivated under standard conditions at 37°C and 5% CO_2 in DMEM-high glucose 10% FBS.

1.2.2 Determination of viable cells

Cells were collected and centrifuged at 900 rpm for 5 min. They were treated with accutase if applicable. Afterwards they were washed once using PBS. Cells were then resuspended in 1 mL of PBS. 10µL cell suspension was diluted 1:2 using 10 µL Trypan Blue Staining Solution 0,4 %. For cell counts a Luna cell counter (Logos Biosystems) was used under default settings to identify the number of viable cells.

1.2.3 Determination of cell growth rate

To measure cellular proliferation, cells were seeded at 100.000 cells per well in 6-well plates and counted 4 days later, using Luna (Logos Biosystems) automated cell counter. The values of doubling times were obtained applying the exponential growth formula $[t\ x\ (ln2)]/\left[\ln\left(\frac{b}{a}\right)\right]$ where t is time, a is the cell count on Day 0, b is the cell count on Day i, and further used for calculation of doublings per day.

1.2.4 Preparation of cells for xenotransplantation

Cells were collected and centrifuged at 900 rpm for 5 min. They were treated with accutase if applicable (TS600, 080125, 080512). Afterwards they were washed once using PBS. Cells were then centrifuged at 1000 rpm for 5 minutes and resuspended in PBS to a concentration of 50.000 cells/µL. Cells were kept on ice until intracranial implantation.

1.2.5 CRISPR/Cas9 single guide design

CRISPR/Cas9 single guides were designed using the online GPP sgRNA Design tool (now called CRISPick, and using the same algorithm, generating identical results) by Broad Institute, in December 2017.

1.2.6 Cloning of CRISPR/Cas9 single guides

LentiCRISPR v2 was digested with Esp3I at 37°C for 4 hours, inactivated at 65°C for 20 mins, and kept at 4°C. For the digest, DTT was added to a concentration of 1mM. Digest with 6 x loading dye (NEB) was run on a 1 % agarose gel at 100 V for 1 h. Band was extracted and cleaned up using QIAquick Gel Extraction Kit (Qiagen). Guide RNA oligo pairs were annealed and phosphorylated using a reaction mix of 1µl of each oligo pair (top and bottom, Table 5) at 100µM, 1µL 10 x T4 ligation buffer, 0,5 µL T4 PNK added up to 10 µL reaction volume using water. Reaction was run in a thermal cycler at 37°C for 30 mins, 95°C for 5 mins, ramped down to 25°C at 0,1°C/sec. Annealed oligos were diluted 1:500. Ligation was performed in a 1:5 ratio of digested and cleaned up back bone and annealed oligos. For reaction, 50 ng of vector were mixed with 1,5 µL of 10 x T4 ligation buffer, 1ul T4 ligase and 2 µL diluted oligos (1:500) and filled up to 15 µL using water. Reaction was incubated at RT for 2 hours. 50 µL of Stbl3 chemically competent cells were transformed using 5 µL of the ligated reaction. Stabl3 were thawed on ice for 20 min, mixed with 5 µL of ligated reaction and incubated on ice for 20 min. Cells were then heat shocked using a heatblock at 42°C for 45 seconds and reaction tube was put back on ice for another 2 min. Stabl3 were grown for 45 min at 37°C after addition of 250 µL SOC medium. Transformed Stbl3 cells were then plated on LB agar plates, containing 100 µg/mL ampicillin, and were kept at 37°C ON (over night). Colonies were picked and after ON incubation in LB medium at 37°C plasmids were preped using QIAprep Spin Miniprep Kit (QIAGEN). T7-endonuclease mismatch detection assay was performed following manufacturer's protocol using Alt-R® Genome Editing Detection Kit (IDT) to evaluate the activity of the site-specific nuclease.

1.2.7 Molecular cloning

MEOX2-FLAG or MEOX2 was cloned into pLVX-puro backbone and MEOX2 was cloned into PB-linker-CAG_MCS_T2A_mNeonGreen backbone by molecular cloning technique. Backbones were each double-digested for 4 h at 37°C, using restriction enzymes XhoI and BamHI (NEB, Table 7). Digests with 6 x loading dye (NEB) were run on a 1 % agarose gel at

100 V for 1 h. Bands were extracted and cleaned up using QIAquick Gel Extraction Kit (Qiagen). Inserts were amplified in a thermal cycler. Primers and templates are described in Table 7. Insert amplification was performed using the Kappa Hi Fi Hotstart ReadyMix (Roche). For a 25 µL reaction, 12,5 µL of Kappa Hi Fi Hotstart ReadyMix and each 0,75 µL (0,3 µM) of 10 µM forward and reverse primers was pipetted into a reaction tube. 70 ng of template DNA were added, and reaction volume adjusted to 25v µL using PCR-grade water. Thermal cycler protocol used is described in Table 16: PCR program for insert amplification. Amplifications were followed by column clean ups using QIAquick PCR Purification kit (Qiagen). Amplified inserts were each double-digested for 4 h at 37°C, using restriction enzymes XhoI and BamHI (NEB, Table 7). Like backbones, inserts were run on gel and cleaned up using QIAquick Gel Extraction Kit (Qiagen). Ligations were performed using Quick Ligation Kit (NEB). Reaction mixes used were: 2 µL Quick Ligation Reaction Buffer (10 x), 25 ng (1:3 reaction) or 17 ng (1:5 reaction) of backbone DNA, 75 ng (1:3 reaction) or 83 ng (1:5 reaction) of insert DNA, 1 µL of Quick Ligase in a total reaction volume of 20 µL (adjusted with nuclease-free water). Reaction mixes were incubated for 5 min at RT. Following transformations of Stabl3 competent E-coli were performed using 5 µL of reaction mix per 50 µL competent bacteria. Transformation of Stabl3 and following steps until plasmid prep were performed as previously described in paragraph „Cloning of CRISPR/Cas9 single guides“.

Table 16: PCR program for insert amplification

Step	**Temperature**	**Time**	**Cycles**
Initial denaturation	95°C	3 min	1
Denaturation	98°C	20 sec	30
Annealing	60°C	15 sec	
Extension	72°C	60 sec/	
Final extension	72°C	72 sec	1
Hold	4°C	Hold	1

1.2.8 Mutagenesis

Point mutation of pLVX-puro-MEOX2-FLAG plasmid at S155 was performed following manufacturer’s protocol using QuikChange Site-Directed Mutagenesis Kit by Agilent. Primers described in Table 7. 20 ng of dsDNA template were used for sample reaction.

1.2.9 Transient transfection of cells

Adherent cell lines were seeded in 6-well dishes. Tumorsphere cell lines were seeded in 6-well dishes previously coated using 20 ug/mL laminin diluted in PBS. 100.000 cells/dish in 2 mL of media were seeded. Transfection was performed using FuGene transfection reagent (Promega) according to manufacturer's protocol. 1 µg of nucleic acid (DNA) was used in a ratio of 3:1 to FuGene reagent. Transfection medium used was Opti-Mem (Gibco).

1.2.10 Viral transductions

CRISPR/Cas9 guides were introduced into pLVX-puro-MEOX2 plasmid by viral transductions using either lentiCRISPRv2-MEOX2-sg1, -MEOX2-sg2 or -NTC plasmids. MEOX2 was stably overexpressed (OE) in TS600, TS667, 080125 and 080512 cell line by viral transduction using pLVX-puro-MEOX2-FLAG or pLVX-puro-MEOX2-S155A-FLAG plasmid. Additional luciferase expression was stably induced by a second viral transduction using pLenti-PGK-V5-LUC Neo plasmid. For virus production, HEK293TN cells were seeded in 10 cm dishes and transiently transfected with plasmid of choice using FuGene transfection reagent. Cells were triple-transfected with packaging and envelope plasmids in a 10:1 ratio, for virus production, and expression plasmid in a ratio of 1:1 to packaging plasmid. After 24 h medium was changed. 48 h, 56 h and 72 h after transfection medium from transfected HEK293TN plates was collected and new medium was added. After the third harvest, per plate merged medium was mixed to a concentration of 10 % with PEG solution and incubated ON at 4°C. After 12 h, PEG/medium mix was centrifuged at 4000 xg for 45 min for virus collection. Supernatant was discarded and virus pellets were diluted in PBS. Virus was added to 10 cm dishes in a 1:1 ratio from collection plate to transduction plate over three days. Virus was stored at 4°C in the meantime. On day 4, medium was changed. On day 5 selection of stably transduced cells was started, facilitating either puromycin or neomycin (depending on resistence casette of plasmid) resistance of used plasmids. Antibiotic was added in a concentration of 0,5 µg/mL for puromycin selection and 400 g/mL Geneticin® for neomycin selection. Fresh medium containing antibiotic was added every three days for 12 days.

1.2.11 Xenograft surgery

GIC cells were cultured, harvested and diluted to a concentration of 50.000 cells/µL prior to surgery. Immunocompromised (athymic Nude) female mice at age of 8 weeks were used for orthotopic implantation. Each experimental group consisted of 8 mice; group sizes were

determined to provide statistical significance of results. Mice were weighed and injected with 5 mg/kg Carprofen s.c.. Mice were then put into an induction chamber with 1-3 Vol% Isoflurane for inhalation. Once mice did not show reflex to toe-pinching, mice were put into stereotactic frame, on a heatmat on 36°C, isoflurane was provided during following surgery via nose cone using 1-2 Vol% Isoflurane. Mouse eyes were covered with eye cream to prevent dryness. Mice were injected with 2 mg/kg Bupivacain near incision site for additional local anasthesia. Iodine solution was used on mouse head as a disinfectant for incision site. After 5 min, vertical incision starting at eye-level, until ear-level of mouse head was made using a scalpel. NaCl solution was added to prevent drying of the tissues. A hole was drilled oriented 2,5 mm right of Bregma. Hamilton syringe was filled with 50.000 GIC cells/µL cell solution. Injection of cells was performed using the previously drilled hole to access brain, syringe tip was positioned using stereotactic frame. 100.000 GIC cells were injected 3 mm deep into the striatum at a speed of 1 µL/min. Cells were allowed to settle for 5 min before syringe was removed. Incision site was closed using tissue glue, and mice were put into seperate cages once awake. Water and wet food were provided after surgery. The next day, mice were injected a second dose of 5 mg/kg Carprofen s.c.. Wounds were checked daily for healing.

1.2.12 IVIS imaging

Mice were injected i.p. (intraperitoneal) with 150 mg/kg luciferin 10 min prior to IVIS imaging. Mice were kept in isoflurane and on a 37° C heated table for measurements. IVIS was performed bi-weekly, starting from 7 days post-surgery and increased to weakly measurments once cell growth onset was observed. 1-3 Vol% Isoflurane was used for anesthesia of mice during imaging process.

1.2.13 Cardiac perfusion

Mice were injected 20 mg/kg Xylazin and 120 mg/kg Ketamin for deep anaesthesia. Mice were fixed to surface using needles, once reflexes were tested negative, and cut open laterally to expose the peritoneum. Afterwards the peritoneum and diaphragm was cut carefully followed by vertical lateral cuts to the sternum. Ribcage was lifted and heart was exposed by moving over the lung. Right atrium was opened through a small cut and left ventricle was punctured carefully, to not puncture the cardiac septum, using a cannulae. Cannulae was hold in place and pump was used to rinse the circulatory system of the mouse for 1 min using PBS at 9 mL/min. Afterwards mice were fixed using 4 % of paraformaldehyde for 5 min at 9 mL/min. Brains were

extracted and fixed in 4 % PFA for 72 h. PFA was changed to phosphate buffer (PB) after 72 h for storage until paraffin embedding.

1.2.14 Cerebral organoid model

To make cerebral organoids (COs) human induced pluripotent stem cells (IPSCs) were treated with TripleLE dissociation reagent to obtain single cells, and were plated in a concentration of 9.000 cells/well into an ultra-low-binding 96-well plate in mTeSR™1 medium containing Rho-associated protein kinase (ROCK) inhibitor (1:200). The mTeSR™1 medium was changed every day and once the embryoid bodies (EB) reached a diameter size of around 500 µm, medium was replaced by cortical induction medium. After three days, EBs, now induced to COs, were pooled into a 6 cm dish containing fresh cortical induction medium. The next day, COs were nucleofected to induce tumorigenic events and amplification of MEOX2. In order to initiate the brain tumors in the COs, tumor suppressor knockouts of Tumor Protein 53 (TP53), Phosphatase And Tensin Homolog (PTEN) and neurofibromin (NF1) were introduced using CRISPR-mediated deletion. Each nucleofection reaction also contained a stably integrating piggybac plasmid, expressing mNeonGreen with or without additional MEOX2 expression (Details in Table 17).

Briefly, 8-10 EBs were collected, resuspended in nucleofection reagent (Nucleofector™ kits for human stem cells P3, Lonza) containing plasmids and transferred into nucleofection vials. Nucleofection was performed according to the manufacturer's protocol using the NucleofectorTM X-Unit (Lonza) with the electroporation pulse program CB-150. After nucleofection, COs were carefully transferred to one well of a 24-well plate containing cortical induction medium and cultured at 37°C incubator overnight. Then, nucleofected COs were embedded into Geltrex and transferred to a low-attachment 6 cm dish containing cortical induction medium and incubated at 37 °C. One day after embedding, COs were transferred to the orbital shaker. From the following day, medium was replaced by differentiation medium with regular medium change every three to four days. Organoids were cultured for four weeks when mNeonGreen intensity was measured. The COs with significant overgrowth of mNeonGreen positive cells were selected for further analysis, such as qPCR and immunofluorescence staining.

Table 17: Nucleofection overview

Condition (µg/nucleofection)	**CRISPR construct (0,4 µg)**				**PB-mNeonGreen construct (0,2 µg)**		**Transposase (0,2 µg)**
	Control (µg)	**Nf1 (µg)**	**PTEN (µg)**	**P53 (µg)**	**mNeonGreen**	**MEOX2-mNeonGreen**	
Negative control	0,4				0,2		0,2
Nf1/PTEN/p53 loss (positive control)		0,133	0,133	0,133	0,2		0,2
PTEN/p53 loss	0,133		0,133	0,133	0,2		0,2
MEOX2 OE	0,4					0,2	0,2
PTEN/p53 loss MEOX2 OE	0,133		0,133	0,133		0,2	0,2

1.2.15 Immunofluorescence

Cells were seeded in a concentration of 5.000 cells/well in 24-well dishes in 500 µL of medium. Organoids were embedded in Tissue-Tek® O.C.T.™ Compound (Sakura) and cut using a cryotome into sections of 20 µm and collected on Thermo Scientific™ SuperFrost™ cover slides. For the staining, 24 h after seeding, medium was removed, and cells were washed twice using PBS. 400 µL 4 % PFA was added to each well and incubated for 20 min at room temperature. PFA was removed and cells were washed twice using PBS. Cells or organoid tissue were then permeabilized using 0,1 % of Triton X-100 for 15 min at room temperature. Afterwards cells were washed three times using PBS, followed by three gentle washes using washing buffer. Cells were blocked using 400 µL of blocking buffer for 45 min at room temperature. Finally, primary antibody was diluted in dilution buffer and added to the cells and incubated at room temperature for 1 h. Primary antibody was removed after incubating for 1 h and cells were washed twice using wash buffer. All following steps were performed without artificial lighting to prevent negative effect on signal intensity of the fluorescent protein labelled secondary antibody. Secondary antibody was added to the cells in 400 µL dilution buffer and incubated for 1 h at room temperature. Afterwards, cells were washed twice using wash buffer. Coverslips were dried off excess moisture on tissue papers, cells facing upwards. Dried coverslips were mounted to microscopy slides using 1 drop of mounting media containing DAPI (VECTASHIELD®) per coverslip. Slides were stored in 4°C for later microscopy.

1.2.16 Whole cell lysates

Plates containing attached cells were put on ice and washed once using PBS. Cells were then directly lysed in the well using 100µL–200µL of NP40 lysis buffer containing 1% Halt Protease und Phosphatase Inhibitor Cocktail (Thermo Fisher) or using lysis buffer (Table 10). Lysate was collected and directly boiled at 95°C for 5 minutes for Western Blot (lysis buffer used) or used for BCA Protein Assay (NP40 lysis buffer used) according to manufacturer's protocol (Thermo Fisher) followed by Western Blot.

1.2.17 SDS page and Western Blot

SDS gels were casted with a concentration of 10 % polyacrylamide. Protein was extracted from cells using lysis protocol. Equal amounts of protein, defined by BCA assay when using NP40 buffer, and defined by cell seeding numbers when using lysis buffer, were loaded on 10% polyacrylamide gels. Gels were run at 80 mV for 20 min, voltage was then increased to 100 mV for following 90 min. Blotting was performed using the Mini-PROTEAN® Tetra electrophoresis wet blot system by Bio-Rad at 100 mV for 90 min or by using the iBlot 2 Dry Blotting System system by Thermo Fisher in setting No2 for 7 min transfer at 60 mV for mixed protein sizes. Membranes were blocked for 30 min in 5 % milk (v/v). Primary antibodies were applied overnight at 4°C in 1° milk. Next day, excess was washed of using TBST buffer for three times 10 minutes each and secondary antibody coupled to HRP was incubated on membranes for 1 hour at room temperature. Membranes were washed 3 times 5 minutes to remove excess milk and protein signal was detected using Pierce ECL Western Blotting Substrate (Thermo Fisher) and ChemiDoc XRS+ Gel Imaging System (Bio-Rad). If further probing on same membranes was performed, membranes were reconstituted using Restore PLUS Western Blot-Stripping-Buffer (Thermo Fisher) for 2 times 15 minutes, followed by a TBST washing and incubation of membranes in 5 % milk before adding the next primary antibody ON at 4°C.

1.2.18 Cycloheximide stability assay

Cells were seeded and transiently transfected as stated before. For analysis of protein stability, cycloheximide was added in a concentration of 200 µg/mL to inhibit protein synthesis. Cells were harveste at different timepoints after cycloheximide exposure and lysed as stated before.

1.2.19 Immunoprecipitation

Whole cell lysates from three replicates per condition, each 5 x 10^6 cells, were prepared. 10 µg of MEOX2 antibody or 10 µg of IgG as a control were added to each of the samples. The reaction volumes were adjusted to 450 µL using NP40 lysis buffer. Reaction was incubated ON at 4°C on a mixer. 25 µL of Pierce Protein A/G Magnetic Beads (Thermo Fisher) were placed into each of 12 (two conditions, three replicates, MEOX2 and IgG antibody samples) 1,5 mL Eppendorf Tubes. 170 µL of Wash Buffer were added to the beads, tubes were rotated and after 5 minutes supernatants were removed while beads were collected on the sides of the tubes in a magnetic stand. Wash step was repeated using 1 mL of Wash Buffer in the second wash. Sample/antibody mixture from day 1 was added to the washed magnetic beads and incubated for 4 h at room temperature on a rotator. Beads were collected in a magnetic stand and flow-through of lysate was saved for later analysis. Beads were washed five times each, using 500 µL of Wash Buffer per tube. Last wash step was performed using H_2O instead of Wash Buffer. Lastly, protein of interest was removed from the Beads using 100 µL of Low pH Elution Buffer. Tubes were incubated for 10 minutes at room temperature and supernatant was collected in the magnetic stand and neutralized using 15 µL of Neutralization Buffer per tube.

1.2.20 RNA extraction

Cells were seeded in a concentration of 5 x 10^5 cells/well in 6-well dishes. Cells were harvested, centrifuged at 4°C and 900 rpm for 5 min. Supernatant was discarded and pellets were washed once with PBS and centrifuged at 900 rpm for 5 min again. RNA was then extracted using the RNeasy RNA isolation kit (QIAGEN) according to manufacturer's protocol. The COs were firstly mashed in 500 µL of Trizol using the TaKaRa® BioMasher tubes followed by RNA isolation according to manufacturer's instructions for TRIzol (Thermo Fisher) chloroform extraction.

1.2.21 RNA-seq

For RNA-seq experiements, biological triplicates of cell lines were seeded in concentration of 5 x 10^5 cells/well in 6-well dishes. RNA extraction was performed as described in paragraph „RNA extraction". Samples were stored at -80°C until submission to the DKFZ Genomics Core Facility.

1.2.22 qPCR

cDNA conversion of extracted RNA was performed using the iScript cDNA Synthesis Kit (Bio-Rad) according to manufacturer's protocol. 350 ng of RNA, identified by NanoDrop measurement, were used per reaction. QPCRs were performed using primers described in Table 8. QPCR reactions were pipetted into 384-well plates according to the SYBR™ Green PCR-Mastermix (Thermo Fisher) manufacturer's protocol. QPCR system used was LightCycler® 480 (Roche). QPCR protocol used is described in Table 18.

Table 18: qPCR program

Step	Temperature	Time	Cycles
Initial denaturation	94°C	2 min	1
Denaturation	94°C	15 sec	40
Annealing, extension and read fluorescence	60 °C	1 min	
Hold	4°C	Hold	1

1.2.23 Antibody-guided Chromatin Tagmentation sequencing (ACT-seq)

ACT-seq experiments were performed by me in collaboration with and under supervision by Dr. Dieter Weichenhan and Marion Bähr in the lab of Dr. Christoph Plass at DKFZ. Non commercially available required materials were kindly provided by the group of Dr. Christoph Plass. The experiments were performed according to the lab-internal protocol, following the protocol by (Carter et al., 2019). ACT-seq was used to identify DNA binding targets of MEOX2 in TS667 and TS600 cells. TS667-sg1/TS667sg-2 and TS600-sg1/TS600 sg2 cells were used as a control, as they obtained a MEOX2 KD. Biological triplicates of each cell line were seeded in a concentration of 1 x 10^6 cells /cell culture flask. They were harvested after 24 h, centrifuged at 4°C, 300 x g for 10 min. Cells were then resuspended in 1 mL of ice-cold PBS, following the referenced protocol steps.

1.2.24 Cleavage Under Targets and Tagmentation sequencing (CUT&Tag-seq)

CUT&Tag experiments were performed by Ashwin Narayanan. Nuclei isolation was performed according to the published protocol by (Narayanan et al., 2020) using a minimum of 1x10^5 cells. Isolated nuclei were washed and centrifuged at 0,6 xg for 4 min. Nuclei were resuspended in 200 µl antibody buffer containing 4 µg MEOX2 antibody or IgG for control, and incubated at

4°C ON. For following CUT&Tag experiments, Hyperactive In-Situ ChIP Library Prep Kit for Illumina（pG-Tn5) and Hyperactive pA-MNase for CUT&Tag (Vazyme) were used. The next day, cells were centrifuged and washed once using Dig-wash buffer. Nuclei were then incubated in 200 µl Dig-wash buffer containing 2 µg of secondary antibody and incubate at RT for 30 min. Cells were washed three times using 200 µL of Dig-wash buffer. Finally, cells were resuspended in Dig-300 buffer and counted. For following steps, nuclei were diluted to a concentration of 100.000 cells/100 µl Dig-300 buffer and 0,8 µl pA-Tn5 were added to the mix and incubated at RT for 1 h. Followed by three wash steps using Dig-300 buffer. 40 µl tagmentation buffer were added to the mix and was incubated in a thermal cycler for 1 h at 37°C. 10 µl of the diluted sample (≈10.000 nuclei), were mixed with 65 µl EB buffer, 0,5 µl 10% SDS and 0,5 µl Proteinase K. Mix was incubated at 50°C for 1 h. Samples were purified using ampure beads in a 1:1,4 ratio, incubated for 5 min at RT and placed on magnet followed by two wash steps using 200 µl of EtOH and 30 sec of incubation each. Supernatant was discarded and sample elute in 20 µl EB buffer. Next, bulk library was prepared using 30 µL of 2 x Kapa, 20 µL of bulk DNA, 5 µL of Index 1 (i5 10 µM) and 5 µL of index 2 (i7 10 µM) and run in a thermal cycler for 17 cycles following the protocol of Table 19. Concentrations were measured using Nano Drop. QC was performed using D1000 tapestation.

Table 19: Bulk library preparation PCR

Temperature	**Time**	**Cycles**
72°C	5 min	1
98°C	3 min	1
98°C	10 sec	16
63°C	30 sec	
72°C	30 sec	
72°C	30 sec	1
72°C	60 sec	1
4°C	Hold	1

1.2.25 EGF treatment of cell lines for pathway activation

GIC cells (TS667, TS600) were washed and seeded in neural stem cell media without EGF/bFGF supplementation. Cells were kept for 48 h; afterwards medium was changed to neural stem cell media containing 50 ng/mL EGF. Cells were then collected at different

timepoints (0 min, 10 min, 30 min, 2 h, 4 h, 6 h, 8 h) to observe pathway initiation by EGF treatment.

1.2.26 Trametinib treatment of cell lines

Cells were washed and seeded in DMEM-high glucose 10% FBS. Cells were transfected 24 h after seeding. Medium was changed to inhibitor containing medium 24 h after transfections. Cells were harvested after 24 h of inhibitor treatment.

1.2.27 MTT assay

Cells were harvested, washed and seeded in a concentration of 5.000 cells/100 µL medium in a 96-well plate. 10 µL MTT reagent (Roche) were added to each well after 24 h, 48 h or 72 h. Cells were then transferred back into the cell incubator for 4-7 h. Afterwards 100 µL of detergent reagent (Roche) were added to each well and plates were incubated ON at room temperature without light. The next day the cells 96-well plate was analysed using Infinite® 200 PRO plate reader (Tecan) at 570 nm absorbance and 670 nm absorbance for reference. Inhibitors were added with immediate seeding to following concentrations: Erlotinib (EGFR inhibitor): 10 µM; AC710 (PDGFR inhibitor): 150 nM; Galunisertib (TGFβ receptor I imhibitor): 10 µM; Trametinib (MEK inhibitor): 100 nM. For the control condition, DMSO was diluted to a concentration of 2 µL/mL.

1.2.28 Next generation sequencing and data analysis

1.2.28.1 Statistical analysis

Two-sided T-test with Welsh's correction was performed if not stated otherwise. Significance is indicated using following legend: ≥0,1234 (n.s.), ≤0,0332 (*), ≤0,0021 (**), ≤0,0002 (***), ≤0,0001 (****).

1.2.28.2 Gene expression profiling

TS667, TS600, 080125, 080512, IHA cells were seeded in a concentration of 5 x 10^5 cells/well in 6-well dishes and harvested 48 h after seeding, during growth phase. IHA cells were seeded in a concentration of 5 x 10^5 cells per well in 6-well dishes and transiently transfected using MEOX2-OE or control-plasmid. Cells were harvested 48 h after transfection. Total mRNA from biological triplicates of TS667-NTC/TS667-sg1/TS667-sg2/TS600-NTC/TS600-

sg1/TS600-sg2 or 080125-MEOX2/080125-control or 080512-MEOX2/080512-control or IHA-MEOX2/IHA-control was extracted using the QIAGEN RNeasy RNA isolation kit according to manufacturer's protocol. Extracted RNA was tested for quality using the Bioanalyzer system by Agilent, following manufacturer's instructions. Samples were stored at -80°C until submission. The sequencing of samples was performed by the DKFZ genomics and proteomics core facility. The sequencing performed was HiSeq 4000 Single-read 50 bp. The aligned bam files and counts were generated by the Omics IT and data management core facility at DKFZ (ODCF). Bioinformatic analysis was performed by Sevin Turcan, PhD. Differentially expressed genes were identified using DESeq2 R package. Values were plotted as transcripts per million (TPM) using normalised RNA-seq by Expectation-Maximization (RSEM) analysis. The RSEM algorithm uses the expectation-maximization technique. It can operate with and without a reference, and reports transcripts per million mapped reads (TPM). RSEM scales linearly with the amount of alignment quantity and uses the Bowtie tool for the read alignments.

1.2.28.3 ACT-seq and CUT&Tag Analysis

The fastq files were trimmed using trimmomatic and aligned to hg19 with bowtie2 using parameters --end-to-end --very-sensitive --no-mixed --no-discordant. Mitochondrial and blacklisted regions were removed from the aligned bam files using samtools. Duplicates were removed using Picard tools (MarkDuplicates). Low quality reads (quality score < 2) were removed using samtools. Peaks were called using MACS version 2.1.2. Differentially bound sites were identified using DiffBind (R statistical package). For visualization, the bam files were normalized to 1x depth using RPGC (reads per genome coverage). The reads within peak regions were plotted as a heatmap using deepTools and visualized using IGV tools.

1.2.28.4 Ingenuity Pathway Analysis (IPA)

For Ingenuity Pathway Analysis (IPA, Qiagen, Germany) the entire list of genes differentially expressed after MEOX2 KD, or MEOX2 OE was filtered for a log2 fold change of <-0,4, >0,4 (-0,8, 0,8 in TS667/TS600) and an adjusted p value of <0,05.

1.2.28.5 Determining mNeonGreen Fluorescence Intensity of organoids

After four weeks, organoids were imaged using a fluorescence microscope (Leica) and the Leica Las X software. For each organoid, three images in different Z-dimensions were acquired. The ImageJ software was used to measure the mNeonGreen intensity of each organoid by

calculating the corrected total cell fluorescence (CTCF). This method determines the corrected total fluorescence by subtracting out background signal, which is useful for comparing the fluorescence intensity between different organoids. Briefly, all three images of one organoid were stacked and maximum intensity projection was performed. Within the stacked organoid image, all fluorescent areas were outlined and integrated density and mean grey value were measured. Afterwards, for background subtraction, three small areas within the same image were selected that have no fluorescence and the mean fluorescence of background readings was calculated. Finally, the CTCF value was calculated using the following formula: CTCF = Integrated Density – (Area of Selected Cell x Mean Fluorescence of Background readings). The CTCF value for each organoid was normalised to the whole area of the corresponding organoid.

2 Introduction

2.1 Glioma

Glioma is a disease of the central nervous system (CNS). Glioma is the most common primary brain tumor in adults. The worldwide age-adjusted annual incidence of histologically verified glioma was 3,5 per 100.000 in 2018 (Central Brain Tumor Registry of the United States (CBTRUS). The name of glioma refers to similarities found between glioma tumor cells and normal glia cells of the brain. The class of glia cells includes astrocytes, microglia, oligodendrocytes and ependymal cells. Primary CNS tumors are graded based on tumor location, extent of tumor spread, genetic findings, patient's age, and tumor remaining after surgery, if surgery is possible. The World Health Organization (WHO) classifies glioma grade based on predicted clinical behaviour (Weller et al., 2021; Weller et al., 2015). Therefore, glioma subtypes include lower grade (WHO grade II) and anaplastic gliomas (WHO grade III) which are both less aggressive than Glioblastoma Multiforme (GBM, WHO grade IV). The distribution of tumor grade measured in Denmark (2009–2014) was 85 % high grade gliomas (WHO grade IV) and 15 % lower grade gliomas (WHO grade II and III, (Rasmussen et al., 2017)), making GBM the most common primary brain tumor found in adults.

2.2 Glioblastoma

2.2.1 Characterization and origin

GBM is an aggressive cancer of the CNS with high proliferative capacity and diffuse pattern of brain invasion. GBM is divided into two clinical subtypes: primary and secondary GBM, also known as WHO grade-IV astrocytoma. Primary GBM arises *de novo* in absence of a pre-existing low grade lesion, and secondary GBM progresses from a low grade glioma, generally over a period of 5-10 years ((Ohgaki & Kleihues, 2013), Figure 1). 95 % of diagnosed GBM are primary GBM, only 5 % are secondary GBM. Although most neurological tumors have a glial origin, it is unclear whether tumor cells result from the transformation of immature precursor cells or from de-differentiation of mature glial cells. The cell of origin is either a neuroglial stem cell or a progenitor cell. Beyond rare instances of genetic predisposition or irradiation exposure, there are no known glioblastoma risk factors (Le Rhun et al., 2019). However, there are common genetic alterations harboured during malignant transformation of cells to primary and secondary glioblastoma. Chromosome 7 is recurrently amplified in GBM, leading to frequent amplification of epithelial growth factor receptor gene (*EGFR*) located on chromosome 7. Another frequent alteration found in GBM is deletion of *CDKN2A-p16,* located

on chromosome 9. Other mutations include genetic alterations in Telomerase Reverse Transcriptase gene (*TERT*), *p53* and *PTEN* (Table 20). In secondary GBM, *IDH1* mutations are frequently found, which were acquired as a clonal early event in lower grade gliomas (LGG) (Figure 1). GBM is characterized by a high degree of cell heterogeneity, which is reflected in the definition "multiforme". Typical histological features of GBM include microvascular proliferation, areas of necrosis, increased mitoses, and pleiomorphic cells (Wen & Kesari, 2008).

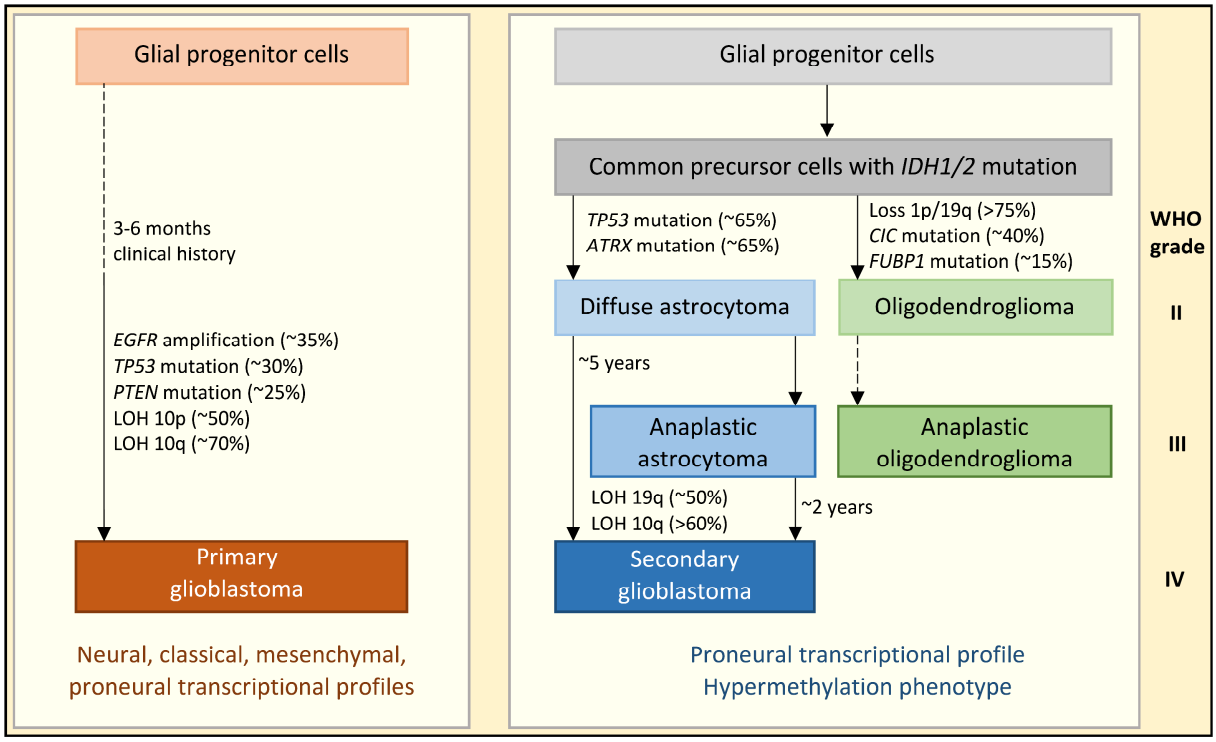

Figure 1: Genetic pathways to primary and secondary glioblastomas.
Modified after (Ohgaki & Kleihues, 2013). LOH = loss of heterozygosity. WHO = World Health Organisation.

Table 20: Frequent genetic alterations in glioblastoma.
IDH1 mutation (Jiao et al., 2012; Yan et al., 2009), *IDH2* mutation (Nobusawa, Watanabe, Kleihues, & Ohgaki, 2009; Yan et al., 2009), *TERT* mutation (Fujisawa et al., 2000; Ohgaki et al., 2004), *EGFR* amplification, *CDKN2A-p16* deletion, *TP53* mutation, *PTEN* mutation (Ohgaki et al., 2004).

Variable	Primary glioblastoma, % (95%)	Secondary glioblastoma, % (5%)
IDH1 mutation	5	67-85
IDH2 mutation	0	0
EGFR amplification	36-60	8
TERT mutation	58	28
CDKN2A-p16^{INK4a} deletion	31-79	19
TP53 mutation	28	65
PTEN mutation	25	4

2.2.2 Histological and molecular GBM classification

GBM can be classified by histological features. WHO grading, ranging from grade I to grade IV, was previously based on malignant characteristics like presence and degree of atypia and mitotic activity, as well as hallmarks for specific subtypes such as microvascular proliferation and/or pseudopalisading necrosis in GBM which is classified as a grade IV tumor. Histopathologic-based glioma classification is however composed of multiple molecular subtypes with distinct differences in biology and prognosis. As a result, the diagnosis and classification of gliomas have been updated in recent years by the WHO to incorporate and classify based on molecular alterations. Integrating phenotypic and genotypic parameters for tumor classification adds objectivity to the diagnostic process. The goal is that this attempt will allow for a more biologically homogeneous and defined diagnosis than in prior histopathological classifications. This should lead to greater diagnostic accuracy and improve patient management with a more accurate determination of prognosis and treatment response. Since 2016, WHO changed the classification system and included molecular alterations into their classification system (Louis et al., 2016). Molecular analysis reveals commonly harboured mutations in the *IDH1* and *IDH2* gene as a main marker for grade II and III gliomas. In diagnosis process, diffuse gliomas are evaluated for *IDH*-mutation status via immunohistochemistry (IHC) or polymerase chain reaction (PCR). *IDH* mutations mainly correlate with a loss of nuclear adenosine triphospate (ATP) dependent helicase (ATRX) or a partial or co-deletion of the 1p/19q chromosomal arms (Figure 2) marking the classes of astrocytomas and oligodendrogliomas. The nuclear ATRX expression can be determined by

IHC. In *IDH*-mutant patients, further analysis of the 1p/19q status is performed. *IDH*-wildtype gliomas with a midline location (mainly in pediatric patients), which can be identified via magnetic resonance imaging (MRI), are additionally tested for H3.3.K27M mutation, a marker for diffuse midline glioma. Glioblastomas are *IDH*-wildtype grade IV gliomas. Glioma classification is constantly adapted by the WHO according to latest research. For the next adaptation of WHO classification, *IDH*-mutant GBM will likely be classified as grade IV astrocytoma (Brat et al., 2020).

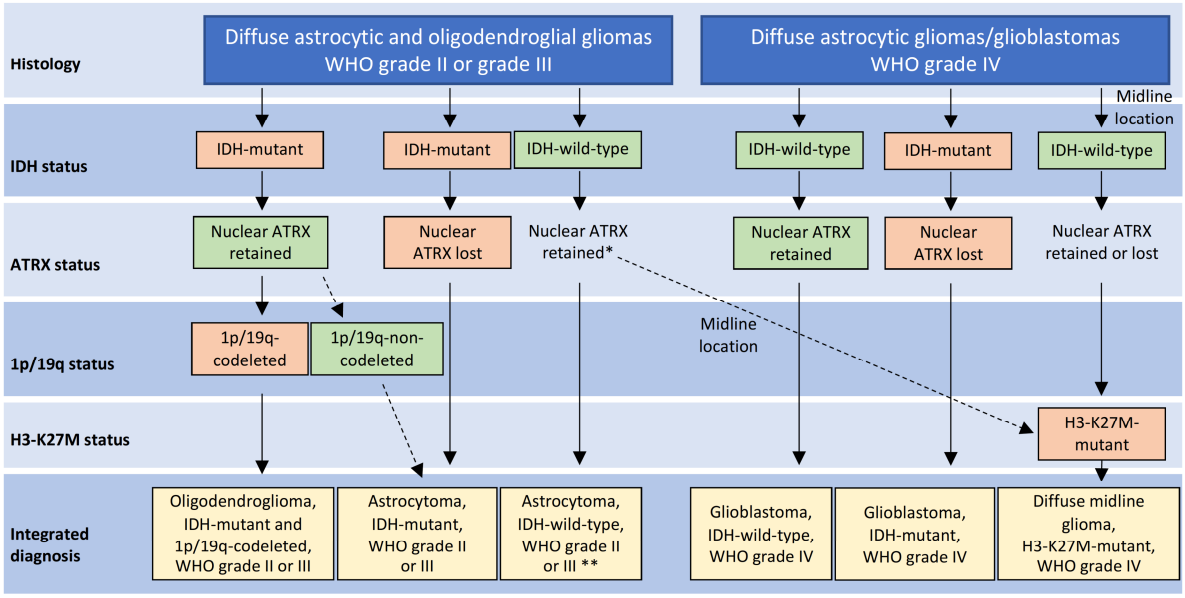

Figure 2: Histological and molecular classifications of gliomas according to the 2016 WHO classification.
*Nuclear ATRX expression is retained in most *IDH*-wildtype WHO grade II and III astrocytic glioma, which demonstrates the molecular proximity to glioblastoma. **WHO grade II or III *IDH*-wildtype astrocytoma is a provisional classification in the 2016 WHO classification system. Glioblastoma, *IDH*-mutant, WHO grade IV is suggested to be updated to astrocytoma grade IV in upcoming terminology. Modified after (Reifenberger, Wirsching, Knobbe-Thomsen, & Weller, 2017).

2.2.3 Frequently altered signaling pathways in GBM

GBM has a complex pathogenesis. Mutations and alterations of several key players of cellular pathway regulation are involved, resulting in increased proliferation, survival, migration and angiogenesis of cells. Understanding of commonly altered pathways is essential to the development of efficient therapies to extend patient survival (Pearson & Regad, 2017).

2.2.3.1 Receptor tyrosine kinases

Receptor tyrosine kinases (RTKs) form a family of receptors located in the cell mebrane. Ligands include growth factors, hormones, cytokines, neurotrophic factors and other extracellular signaling molecules (Regad, 2015). The most relevant signaling pathways involved in GBM include growth factor RTK-triggered pathways, including the RAS sarcoma

(RAS) pathway, as well as the phosphatidylinositol 3-kinase (PI3K)/phosphatase and tensin homolog (PTEN)/v-akt murine thymoma viral oncogene homolog (AKT), retinoblastoma (RB)/cyclin-dependent kinase (CDK) N2A-p16INK4a, and the TP53/mouse double minute 2 (MDM2)/MDM 4/CDKN2A-p14ARF pathways. These pathways are involved in the regulation of cell proliferation, survival, differentiation and angiogenesis, all known drivers of cancer. Therefore, RTKs and their ligands are promising therapeutic targets for the treatment of GBM (Crespo et al., 2015; Montano, D'Alessandris, Izzo, Fernandez, & Pallini, 2016).

2.2.3.2 The RAS/MAP/ERK pathway

Activated by cell surface receptors, the RAS/MAP/ERK pathway regulates angiogenesis, cell proliferation, migration and survival. The activation of RAS protein by the exchange of guanosin diphosphate (GDP) with guanosin triphosphate (GTP), results in the activation of MAP kinases, and a direct phosphorylation of ERK by MEK (Figure 3) (McCubrey et al., 2007). Activation of the RAS/MAP/ERK pathway also leads to activation of Hypoxia-inducible factor 1-alpha (HIF-1α), which promotes tumorigenesis and activation of vascular endothelial growth factor (VEGF) (Crespo et al., 2015; Tuncel & Kalkan, 2018).

2.2.3.3 The RAS/PI3K/AKT/mTOR pathway

RAS/PI3K/AKT/mTOR pathway was found to be altered in 86–90% of GBM (Brennan et al., 2013). Activation of the signaling cascade is induced by transmembrane RTK receptors, transmembrane integrins and G-protein-coupled receptors. Upon receptor activation, functional PI3K translocates to the plasma membrane and leads to the production of phosphatidylinositol 3,4,5-triphosphate (PIP3) from phosphatidylinositol bisphosphate (PIP2). PIP3 recruits AKT to the plasma membrane where it is activated by phosphorylation at threonine 308. PTEN acts to counteract PI3K signaling, acting as a tumor suppressor, by dephosphorylating PIP3 to PIP2 (Figure 3) (Crespo et al., 2015; Pearson & Regad, 2017; Tuncel & Kalkan, 2018)

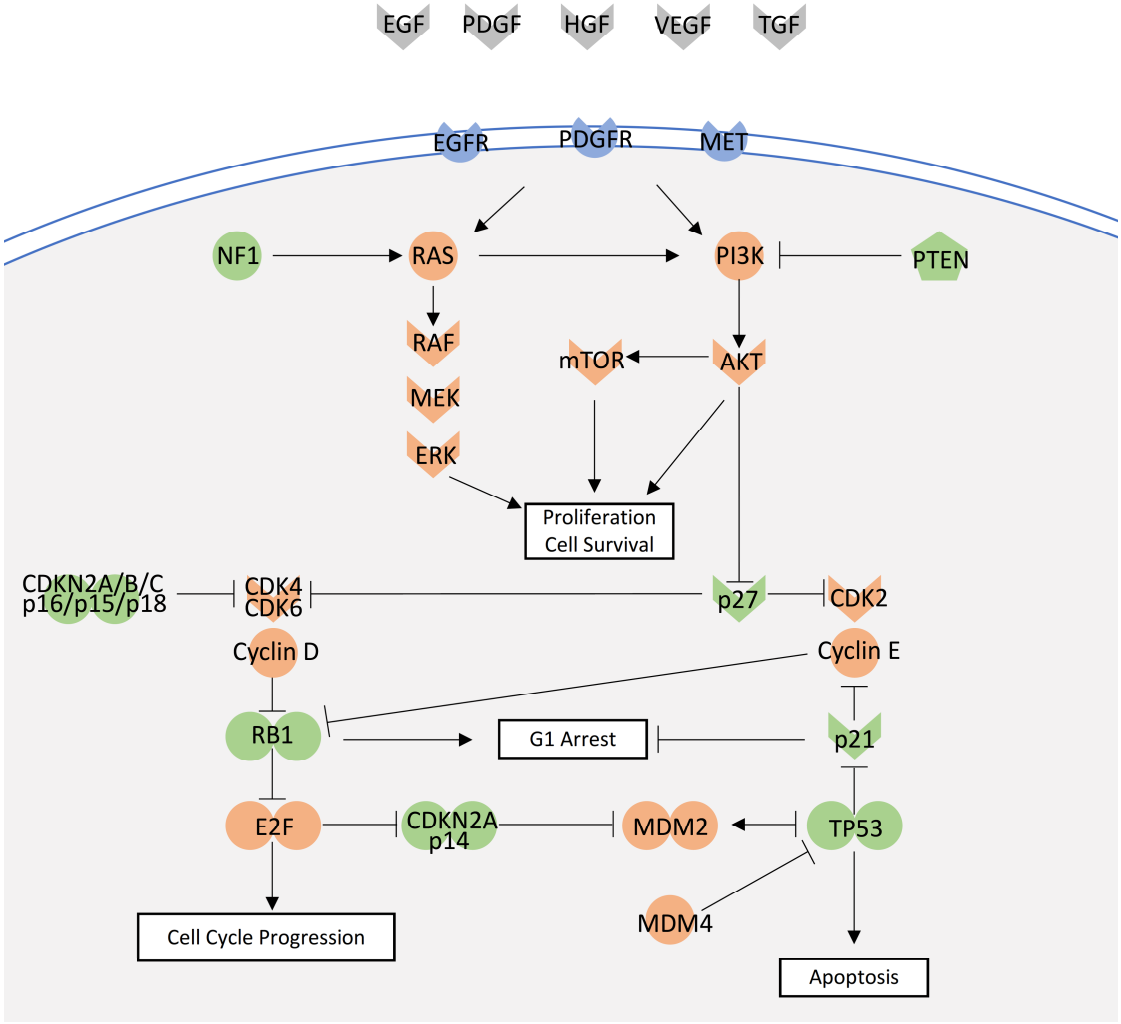

Figure 3: Major signaling pathways involved in pathogenesis of glioblastoma.
Genes that are inactivated (green) or hyperactivated (orange) by different mechanisms are shown in green and orange, respectively. Modified after (Crespo et al., 2015).

2.2.4 Course of disease and therapy

With high infiltration, and limited therapy options, median survival time remains at an average of 15 months for GBM patients, even after radiotherapy and temozolomide treatment (Stupp et al., 2005). No early detection for GBM is available. When lesions are identified via MRI, the tumor, in case of GBM, is usually in an advanced state. Concomitant symptoms include neurological focal deficits, cognitive and behavioural changes, headaches and seizures (Rasmussen et al., 2017). Standard of care includes surgery and non-specific targeting of proliferating cells using alkylating agents temozolomide or PCV (procarbazine, lomustine, vincristine) chemotherapy (Schmidt et al., 2006) and radiation. Due to highly infiltrative growth patterns, GBM is usually not surgically removed completely, leading inevitably to recurrence. A first targeted therapy against VEGF using an antibody, bevacizumab, can lead to prolonged progression-free survival, however, can not increase overall survival (Diaz et al., 2017). No

drug treatment has been shown to change course of disease in patients. Until now, targeting frequently altered cellular pathways, such as previously mentioned PI3K/AKT/mammalian target of rapamycin (mTOR), the p53 and the RB pathways, or EGFR gene amplification or mutation, have failed to improve outcome in GBM (Le Rhun et al., 2019; Pearson & Regad, 2017). This is likely due to unwanted compensatory mechanisms in cancer as well as insufficient target coverage (also related to the blood brain barrier) or poor tolerability and safety of drugs (de Vries et al., 2012; Haas-Kogan et al., 2005)

2.3 MEOX2

MEOX2 is a human homeobox transcription factor first isolated and described in 1995 (Grigoriou et al., 1995). The protein consists of 304 amino acids, the mass of protein is 33,6 kDa. Chimpanzee, Rhesus monkey, dog, cow, mouse, rat, chicken, zebrafish and frog all have a highly conserved regions of human MEOX2 gene: a 180 bp DNA binding homeobox sequence, the 12 amino acid polyhistidine stretch in N-terminal region of protein, and a number of potential serine/threonine phosphorylation sites. The homeodomain of MEOX2 protein is identical to other vertebrate species' (Candia, Kovalik, & Wright, 1993; Gorski et al., 1993). Conserved sequences outside the homeodomain show a small differences in amino acid sequence between human and rodent polypeptides (Grigoriou et al., 1995). The chromosomal position of MEOX2 was assigned to chromosome 7, 7p22.1–p21.3. Chromosome 7 is frequently amplified in GBM leading to amplifications of genes located of chromosome 7, like EGFR amplification (Lopez-Gines et al., 2005).

2.3.1 Role of MEOX2 in development

MEOX2 is a vertebrate homeobox-containing transcription factor. It is expressed during development where it plays essential roles in the differentiation of developing tissues. MEOX2 is a mesenchymal signaling molecule. It plays a role in the determination of the soft palatal epithelium as well as inhibition of keratinization and in bone formation (Jin & Ding, 2006; Kim et al., 2020). Although some functions of MEOX2 are known, the exact mechanisms of MEOX2 in regulation of vascular smooth muscle cell proliferation, differentiation and migration are not yet known (Lin et al., 2005). It was shown that it can affect skeletal muscle satellite cell differentiation and apoptosis via the PI3K/AKT pathway (Yin et al., 2020). MEOX1 and MEOX2 homeobox genes are closely related and are expressed in overlapping patterns in the paraxial mesoderm and its derivatives. In MEOX2-deficient limb buds, downregulation of paired box gene 3 (Pax3) and myogenic factor 5 (Myf5) but not of nomyoblast determination protein 1 (MyoD) were observed, suggesting a role for MEOX2 as an important regulator of

vertebrate limb myogenesis. It is essential for normal appendicular muscle formation and for normal regulation of myogenic genes however not needed for migration of myogenic precursors into the limb bud (Mankoo et al., 1999).

2.3.2 Known targets of MEOX2

MEOX2 was found to bind and activate transcription of p16 (INK4a); it also directly activates transcription of p21 (CIP1/WAF1), in a DNA binding independent manner (Douville, Cheung, Herbert, Moffatt, & Wigle, 2011; Smith et al., 1997). These cyclin dependent kinase inhibitors regulate vascular cell proliferation by regulating the G(1)/S cell cycle checkpoint, that defines whether a cell enters into an arrested state of senescence (Terzi, Izmirli, & Gogebakan, 2016). Cell cycle arrest can be associated with endothelial cell dysfunction and atherosclerosis. MEOX2 and MEOX1, also a member of the homeobox-transcription factor family, were described to partially share functions during development, suggesting they might regulate similar target genes *in vivo*. Increased expression of MEOX2 or MEOX1 both lead to cell cycle arrest and endothelial cell senescence (Douville et al., 2011). Additionally, binding of MEOX2 to RING finger protein 10 (RNF10) has been observed. RNF10 overexpression lead to increased p21 promoter activation via MEOX2 (Lin et al., 2005).

2.3.3 MEOX2 in cancer

Expression of MEOX2 was observed to be lower in larynx carcinoma tissue than in normal tissue, correlating with cancer progression. Overexpression of MEOX2 in laryngeal cancer cells reduced cell viability and increased apoptosis. Mechanistic studies using laryngeal cancer cells showed PI3K/AKT pathway was affected by MEOX2 expression. Hence in the context of laryngeal carcinoma, MEOX2 was reported as a potential therapeutical gene (Tian et al., 2018). Homeobox-related gene transcription factors, such as MEOX2, have been associated with drug resistance and malignant progression in lung cancer patients (Armas-López et al., 2017). The mechanisms involved have yet to be elucidated. In non-small cell lung carcinomas (NSCLC) MEOX2 expression was found to positively modulate Hedgehog-GLI1 gene expression and induce the mTOR pathway resulting in overall poorer survival of NSCLC patients, as well as Twist Family BHLH Transcription Factor 1 (TWIST1) and Snail Family Transcriptional Repressor (Snail) activation, linked to the Hedgehog pathway, inducing a more chemoresistant stem cell-like phenotype (Armas-López et al., 2017).

2.3.4 MEOX2 in GBM

The function of MEOX2 in context of GBM has not been elucidated. However, analysis of The Cancer Genome Atlas (TCGA) LGG and GBM cohorts have shown a strong correlation between the tumor grade and MEOX2 expression. High MEOX2 expression is linked to poor survival. Same was observed with MEOX2 staining of glioma tissues. Hence significance of MEOX2 for GBM prognosis was reported (Tachon et al., 2019). These results raise an interest in understanding the function of MEOX2 in glioma.

3 Aim of the study

MEOX2 expression has been shown to correlate with tumor grade in the analysis of TCGA dataset, indicating a prognostic significance of MEOX2 for glioma patients (Tachon et al., 2019). For GBM patients, besides the standard of care, no therapy is found that can significantly change overall survival of patients. Only limited prolongation of progression-free survival can be maintained using standard of care therapies like surgery, radiation and chemotherapy. Targeted therapies remain with limited effects as tumor cells have compensatory mechanisms. In case of MEOX2 transcription factor, the strong correlation of expression with clinical outcome and significance for prognosis arises interest in characterization of MEOX2 role in GBM. Therefore, with this study, my goal is to contribute to MEOX2 characterization in GBM. Aim is to identify, whether MEOX2 is a potential oncogene in gliomas. Therefore, I investigate phenotypic changes in cell growth initiated by MEOX2 expression *in vivo*. I also investigate whether MEOX2 alters cell proliferation in context of additional loss of tumor suppressors (such as PTEN, p53) in a cerebral organoid model. Furthermore, I identify an ERK/MAPK-related phosphorylation site in MEOX2 protein. In addition, I identified potential binding targets of MEOX2 in GBM tumorspheres and primary tumors using ACT-seq and CUT&Tag. To determine the transcriptional alterations induced by MEOX2, I generated RNA-seq data from GBM tumorspheres with MEOX2 KD and identified deregulated genes and pathways.

4 Results

4.1 *MEOX2* expression correlates with glioma grade and *IDH* status

MEOX2 is a homeobox transcription factor known to activate p16 and p21 cyclin dependent kinase inhibitors. By direct activation of G(1)/S cell cycle checkpoint regulators, MEOX2 induces endothelial cell cycle arrest (Douville et al., 2011). In humans, *MEOX2* is upregulated during embryonic development in several organs including the placenta (Quinn, Latham, & Kalionis, 2000) and it is detected in early cardiomyocytes, lateral plate mesoderm and somitic mesoderm (Skopicki et al., 1997). In addition, MEOX2 regulates the differentiation of human fibroblasts to myofibroblasts (Noizet et al., 2016) in smooth muscle cells and acts as a driver of endothelial cell proliferation and endothelial-to-mesenchymal transition (Valcourt, Thuault, Pardali, Heldin, & Moustakas, 2007). MEOX2 has also been shown to play a role in different cancers. It is upregulated in tissues that do not express MEOX2 in their healthy states and downregulated in tissues with high endogenous expression. The contribution of MEOX2 to tumorigenesis may be tissue-dependent, and a clear role for MEOX2 in cancers is lacking.

We have previously shown that overexpression of IDH mutation in IHA cells led to a persistent *MEOX2* downregulation (Turcan et al., 2018). Furthermore, *MEOX2* expression levels correlated with glioma tumor grade (Tachon et al., 2019). Similar analyses were performed at the Turcan Lab, giving a first indication of *MEOX2* as a potential oncogene. I re-analyzed the formerly shown data, using the latest publicly available LGG and GBM cohorts of TCGA (Tomczak, Czerwińska, & Wiznerowicz, 2015) and CGGA (Z. Zhao et al., 2021) datasets. Interestingly, *MEOX2* expression correlates with tumor subtypes (Figure 4A). The highest *MEOX2* expression is found in GBM (log_2 TPM: 8,4 ± 2,3 SD), oligodendroglioma (log_2 TPM: 2,5 ± 2,0 SD), oligoastrocytoma (log_2 TPM: 3,0 ± 2,5 SD) and astrocytoma (log_2 TPM: 3,3 ± 3,4 SD) show significantly lower expression of *MEOX2*. Furthermore, I separated the cohorts by IDH1 status. IDH wild-type (wt) status is a marker used to identify GBM, and IDH mut status is correlated with a better prognosis and LGG. When I separate TCGA cohorts by IDH status, *MEOX2* expression is significantly increased in the IDH wt samples within each subtype over IDH mut samples (Figure 4A). IDH mut secondary GBM (log_2 TPM: 3,0 ± 1,0 SD), oligodendroglioma (log_2 TPM: 2,1 ± 1,3 SD), oligoastrocytoma (log_2 TPM: 2,3 ± 1,5 SD) and astrocytoma (log_2 TPM: 1,6 ± 1,4 SD) have significantly lower *MEOX2* expression than IDH wt GBM (log_2 TPM: 8,7 ± 2,0 SD), oligodendroglioma (log_2 TPM: 3,7 ± 3,3 SD), oligoastrocytoma (log_2 TPM: 7,0 ± 3,2 SD) and astrocytoma (log_2 TPM: 6,7 ± 3,8 SD). As IDH mutation is a marker for LGGs (WHO II, III), and only found in secondary GBM, whereas primary GBM are classified by IDH wt status (Figure 1) the observation of increased *MEOX2*

expression correlating with IDH wt status is striking. When I separate the GBM cohort of the Chinese Glioma Genome Atlas (CGGA) dataset by IDH status, I identify the same significant increase in *MEOX2* expression correlating with IDH wt status (Figure 4B, log_2 TPM: IDH mut GBM: 0,4 ± 1,6, IDH wt GBM: 5,6 ± 11,9).

To determine which cell type in gliomas have increased *MEOX2* expression, we queried publicly available single cell RNA-seq datasets. These datasets allow for a correlation analysis between *MEOX2* expression and cell types of surgically dissected glioma samples. We used the single cell RNA-seq dataset obtained from adult GBM (Neftel et al., 2019) and stratified gene expression by cell identities. By this I was able to show that *MEOX2* was highly expressed in the malignant cells of the tumor samples (Figure 4C) and is not or low expressed in the tumor microenvironment (including macrophages, oligodendrocytes and T-cells). These analyses show that MEOX2, a transcription factor that is not expressed in the normal brain (≤ 0,5 pTPM, Table 22) (Uhlén et al., 2015), is upregulated in malignant brain tumor cells, especially in IDH wt GBM versus IDH mut LGG.

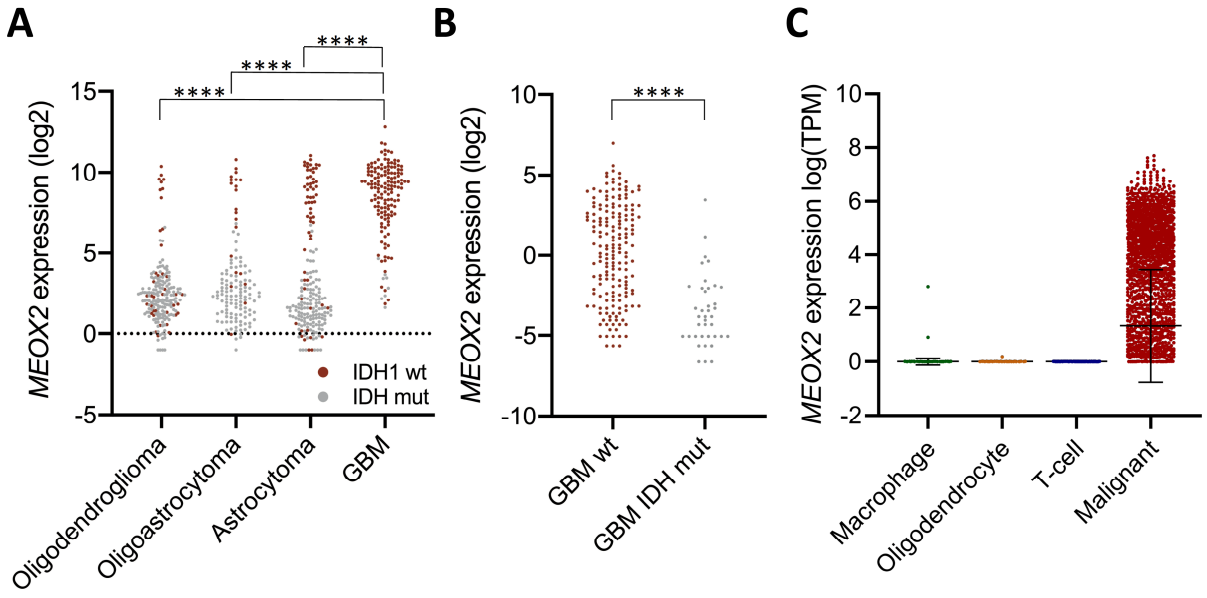

Figure 4: *MEOX2* expression in glioma. Analysis of TCGA and CGGA datasets.
A) *MEOX2* gene expression analysis of *IDH1* wildtype (wt) and IDH1R132H-positive (mut) gliomas sorted by glioma subtype. IDH wt: Oligodendroglioma n = 39, Oligoastrocytoma n= 21, Astrocytoma n = 62, GBM n = 144, IDH mut: Oligodendroglioma n = 152, Oligoastrocytoma n= 109, Astrocytoma n = 132, GBM n = 8; mean ± SD; Two-sided Welsh's test; raw data from TCGA database 2013. B) *MEOX2* gene expression analysis of *IDH1* wildtype (wt) and IDH1R132H-positive (mut) gliomas. IDH wt n = 190, IDH1R132H n = 49; mean ± SD; Two-sided Welsh's test; raw data from CGGA database. C) *MEOX2* expression in single cell data (Neftel et al., 2019) sorted by macrophages (n = 536), oligodendrocytes (n = 210), T-cells (n = 80) and malignant cells (n = 4916); mean ± SD; Two-sided Welsh's test.

4.2 *MEOX2* OE deregulates cancer associated pathways in IHA

To find out whether *MEOX2* upregulation alone will be sufficient to induce a malignant gene expresion program in non-cancer cells, I transiently overexpressed MEOX2 in immortalized human astrocytes (IHAs) and performed RNA-seq after 48 hours to compare control transfected and MEOX2 transfected IHAs. 49 genes were significantly deregulated, of which 38 were upregulated and 11 downregulated after MEOX2 OE. Ingenuity pathway analysis revealed multiple deregulated pathways following MEOX2 OE (38 gene networks) in IHAs. The IPA analysis database is curating genes connected to cellular functions into networks. To identify genes associated with MEOX2 in both IHAs and primary GBMs, I identified the top 50 genes that were correlated with MEOX2 in the TCGA GBM dataset. Using IPA, I identified 17 gene networks correlating with MEOX2 expression. 12 networks were found commonly deregulated between IHA after transient MEOX2 overexpression and the top 50 genes that were correlated with MEOX2 in the TCGA GBM dataset (Figure 5, left). Overlapping networks include MEOX2 regulated pathways like the cell cycle, cellular development and tissue development. Other networks such as cancer, cellular growth and proliferation and cell death and survival, all connected to the hallmarks of cancer (Hanahan & Weinberg, 2011), were identified (Figure 5, right). Overall, my results indicate that at a transcriptional level, MEOX2 overexpression leads to deregulation of several cancer-related networks in a non-cancer cell line setting.

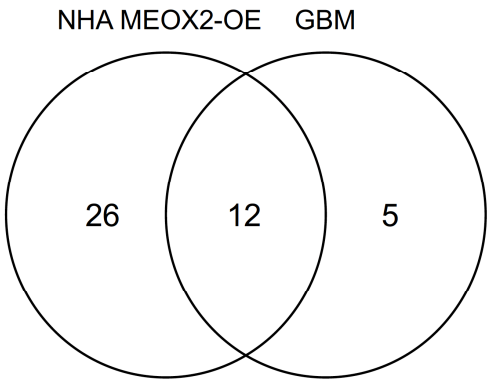

Common networks
Cancer
Cell Cycle
Cell Death and Survival
Cellular Assembly and Organization
Cellular Development
Cellular Function and Maintenance
Cellular Growth and Proliferation
Hereditary Disorder
Neurological Disease
Organismal Injury and Abnormalities
Post-Translational Modification
Tissue Development

Figure 5: Pathway analysis of IHA transiently expressing MEOX2. Comparison to pathways of top 50 deregulated genes correlating with MEOX2 upregulation in TCGA dataset.
Left: 38 networks were found deregulated in IHA cells upon transient MEOX2 OE, log2 fold change of >0,4, adjusted p value of <0,05. 17 networks were found significantly deregulated in TCGA data correlating with MEOX2 upregulation in glioma. 12 of identified natworks overlap between TCGA dataset and in vitro experiment using IHA cells. Right: list of overlapping deregulated pathways.

4.3 MEOX2 OE induces growth phenotype in *in vivo* GIC xenograft model

To further investigate the effect of MEOX2 in cancer, I identified two patient-derived GBM cell lines that show low endogenous MEOX2 expression levels (080125, 080512). As I identified before, IDH wt status in GBM significantly correlated with high expression of *MEOX2* (Figure 4A, B). GBM lines with low endogenous MEOX2 expression allows for a study comparing cells with low endogenous MEOX2 expression to exogenously increased MEOX2 levels in the same heterogeneous tumour cell environment. Therefore, I stably overexpressed MEOX2 in both of these cell lines (referred to as 125-MEOX2 and 512-MEOX2) (Figure 6A). MEOX2 expression was successfully introduced and confirmed by Western Blotting. The levels of overexpressed MEOX2 expression remain lower than endogenous levels, shown in cell line TS667 on same Western Blot for reference. The newly created cell lines with MEOX2 OE were labeled with luciferase for *in vivo* bioluminescence imaging (BLI). I orthotopically implanted the luciferase-labeled MEOX2 OE lines in the striatum of immunocompromised mice, with the help of my colleague A. Narayanan, PhD. After 8 weeks, BLI indicated the first significant differences observed in cell growth. Cell proliferation was measured in luminescence intensity difference induced by luciferin injections and active luciferase in the implanted cell lines (Figure 6). Cell line 125-MEOX2 showed a constantly significantly increased growth over 125-control starting from week 10 until end of measurements at week 16 (Figure 6B, C). At the endpoint measurement, 125-MEOX2 mice showed an average total flux of 1,2 x 10^6 p/s whereas 125-control averaged at less than half of this intensity at 5 x 10^5 p/s. MEOX2 induced a faster growth phenotype when overexpressed in 125 cell line, visible in the average over all mice (Figure 6B) as well as in all individual observations (Figure 6C). The signal measured was not only denser but also spread over a larger area when comparing 125-MEOX2 (Figure 6 D, top) versus 125-control (Figure 6D, bottom). 512-MEOX2 and 512-control lines present no difference in growth dynamic. Overall growth of 125 line had an earlier onset (week four, Figure 6E) compared to 125-MEOX2 line (week eight, Figure 6B) and a higher slope in luminescence signal intensity. This trend stays until the end of experiment at week 16. Different to the 125 cell line, in the 512 cell line, there was no difference observed in growth between 512-MEOX2 and 512-control, neither in average values (Figure 6E) in individual measurements (Figure 6F) or in area of tumor growth (Figure 6G, top versus bottom). MEOX2 affected the growth phenotype *in vivo* only in the slower growing cell line model (080125). In the faster growing cell line (080512) MEOX2 did not induce a faster growth phenotype. Similar results were observed before, when I transplanted GBM cell lines with high endogenous MEOX2 expression (TS667, TS600) versus same lines after MEOX2 KD generated by CRISPR/Cas9 single guides (Figure 17). Both cell lines showed fast growth

dynamics and no difference in cell growth could be observed between the parental lines, expressing MEOX2, and the CRISPR/Cas9 modified MEOX2 KD lines (data not shown).

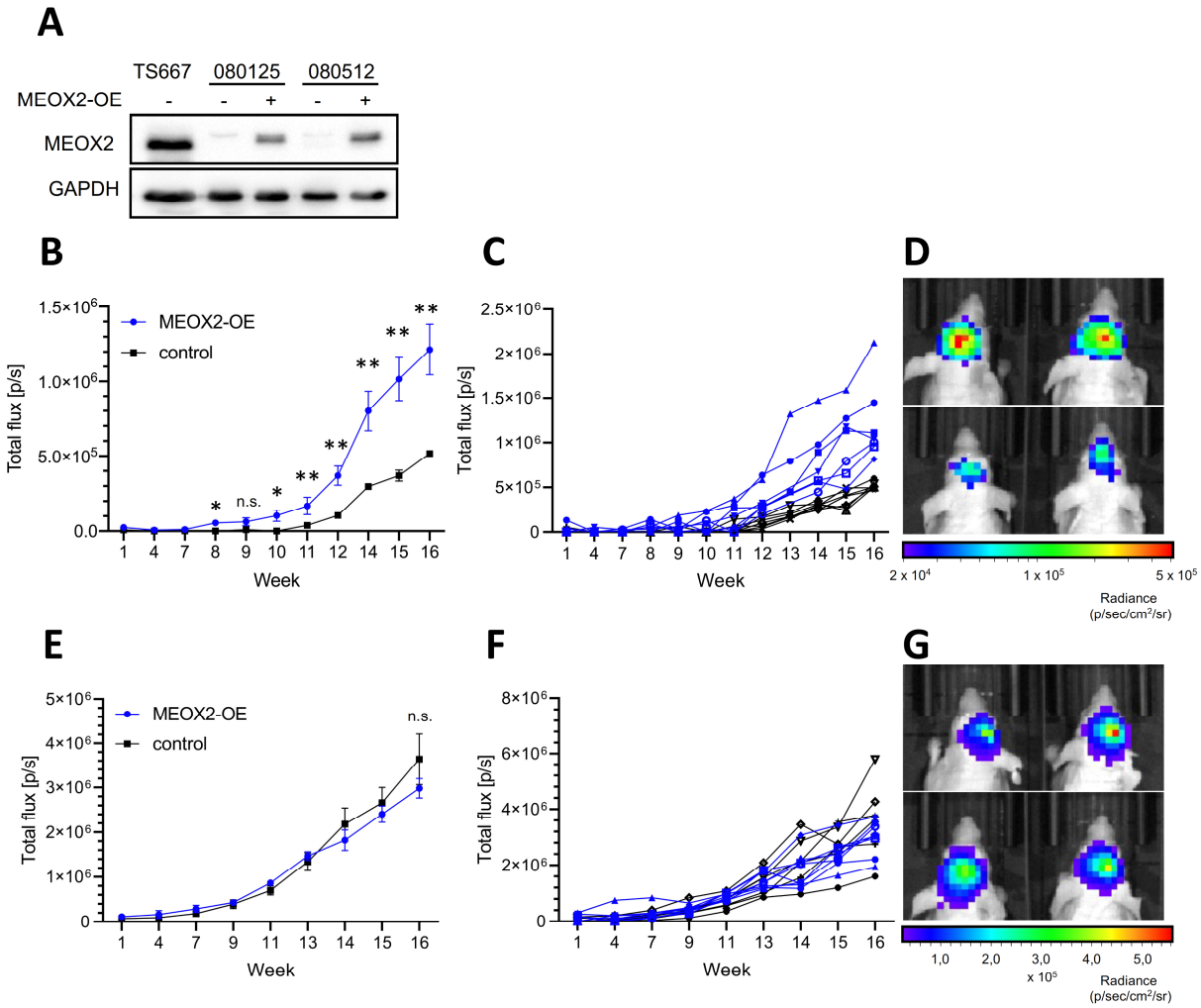

Figure 6: *In vivo* xenograft of GIC stably overexpressing MEOX2.
A) MEOX2 levels in patient derived tumorsphere cell lines (TS667, 080125, 080512) after stable transduction using MEOX2 plasmid (+) versus control plasmid (-). B) Average luminescence measurement of xenograft transplanted mice. 080125 cell line OE MEOX2 (blue, n = 7) versus OE control plasmid (black, n = 7, mean ± SD, Two-sided Welsh's test, x-axis = week, y-axis = total flux (p/s)). C) Individual luminescence measurements of xenograft transplanted mice. 080125 cell line OE MEOX2 (blue, n = 7) versus OE control plasmid (black, n = 7, mean ± SD, Two-sided Welsh's test, x-axis = week, y-axis = total flux (p/s)). D) Luminescence distribution in two representative mice per group, each xenograft transplanted with MEOX2 OE 080125 cells (top) versus control plasmid OE 080125 cells (bottom), scale: radiance in p/sec/cm^2/sr. E) Average luminescence measurement of xenograft transplanted mice. 080512 cell line OE MEOX2 (blue, n = 7) versus OE control plasmid (black, n = 7, mean ± SD, Two-sided Welsh's test, x-axis = week, y-axis = total flux (p/s)). F) Individual luminescence measurements of xenograft transplanted mice. 080512 cell line OE MEOX2 (blue, n = 7) versus OE control plasmid (black, n = 7, mean ± SD, Two-sided Welsh's test, x-axis = week, y-axis = total flux (p/s)). G) Luminescence distribution in two representative mice per group, each xenograft transplanted with MEOX2 OE 080125 cells (top) versus control plasmid OE 080512 cells (bottom), scale: radiance in p/sec/cm^2/sr.

4.4 MEOX2 OE induces growth phenotype in cerebral organoids

As MEOX2 OE only increased *in vivo* tumor growth in the GBM cell line with slow basal *in vivo* growth dynamics (080125), and not in the line with fast growth dynamics (080512); along with the observation that MEOX2 KD of endogenous MEOX2 did not decrease tumor growth in GBM cell lines with an already fast *in vivo* growth dynamics (TS667, TS600; data not shown), I hypothesized that MEOX2 could be involved in tumor initiation. To find out whether MEOX2 played a role in tumor initiation, we collaborated with the lab of Dr. Moritz Mall at DKFZ, where the doctoral researcher Elisa Heinzelmann performed a series of experiments for us. The Mall Lab uses a cerebral organoid (CO) model of the brain, growing from IPSC. This model allows to identify the role of individual proteins in tumor progression by modulating their expression *in vitro*. The Mall lab developed a tumor model with transient knockdown of key tumor suppressors downregulated via CRISPR/Cas9 technique. For analysis and quantification, in-frame mNeonGreen was used as a fluorescent reporter cloned into the PiggyBac transposon system plasmid (Q. Chen et al., 2020). Using multiple targeting plasmids for co-nucleofection, a double or triple KD of multiple genes can be obtained (Chicaybam et al., 2016). Targeting sequences were cloned into lentiCRISPRv2 backbone. Key drivers of GBM are non-functional mutations or deletions in tumor supressor genes *PTEN*, *p53* and *Nf1*. As described earlier, PTEN is a tumor suppressor, counteracting PI3K signaling by dephosphorylating PIP3 to PIP2, by this inhibiting the RAS signaling pathway (C. Y. Chen, Chen, He, & Stiles, 2018). P53 has multiple functional roles. It acts as a direct transcriptional activator, resulting in tumor suppressing pathway regulations (Sullivan, Galbraith, Andrysik, & Espinosa, 2018). Nf1 negatively regulates RAS pathway signaling. Increased RAS activity leads to downstream activity of MEK-ERK pathway as well as the PI3K-AKT-mTOR pathway. Both pathways are commonly activated in cancer (Figure 3) (Lobbous et al., 2020; Philpott, Tovell, Frayling, Cooper, & Upadhyaya, 2017). To investigate MEOX2 in the CO model I cloned a new MEOX2 OE plasmid. I inserted MEOX2 in-frame with mNeonGreen, for fluorescent based measurements. Elisa Heinzelmann nucleofected MEOX2 alone, or in the context of PTEN/p53 KD, which are commonly mutated or lost in GBM as they serve as tumor suppressing genes in healthy tissues. Additionally, we used a scramble vector as a negative control plasmid. For a positive control, we used a combination of PTEN/p53 KD with simultaneous Nf1 KD (Table 17). After one month of culture, organoids were analysed using microscopy and image analysis software (Figure 19). Fluorescence of nucleofected positive cells was measured at Day 2 and Day 28 (Figure 19). Quantified results based on fluorescence measurements show an increased cell proliferation after MEOX2 OE, however observed effect increases significantly after additional PTEN/p53 KD. The growth of the triple nucleofected

CO using MEOX2 OE/PTEN KD/p53 KD shows equal levels in growth to the positive control of Nf1 KD/PTEN KD/p53 KD (Figure 7A). PTEN/p53 KD alone, as well as MEOX2 OE alone, did not induce the same effect on proliferation as the mentioned triple nucleofections (Figure 7A). These results point out the tumorigenic potential of MEOX2 in a tumor background and the importance of further investigations of MEOX2 in context of cancer.

I observed the morphology of the nucleofected and MEOX2 positive cells within the CO using Confocal Laser Scanning Microscopy technique (CLSM). As shown in Figure 7 C, the MEOX2 positive cells of the triple nucleofected CO using MEOX2 OE/PTEN KD/p53 KD show a more elongated shape (Figure 7C, left) versus the single *MEOX2* OE nucleofected cells (Figure 7C, right) do not show an elongated phenotype. The morphological difference could point to a structural difference in the MEOX2 OE/PTEN KD/p53 KD cells switching to a more mesenchymal state. Elongation of the cells is a first indication pointing to a more mesenchymal state of the MEOX2 OE cells in context of tumor initiating PTEN/p53 KD in this model.

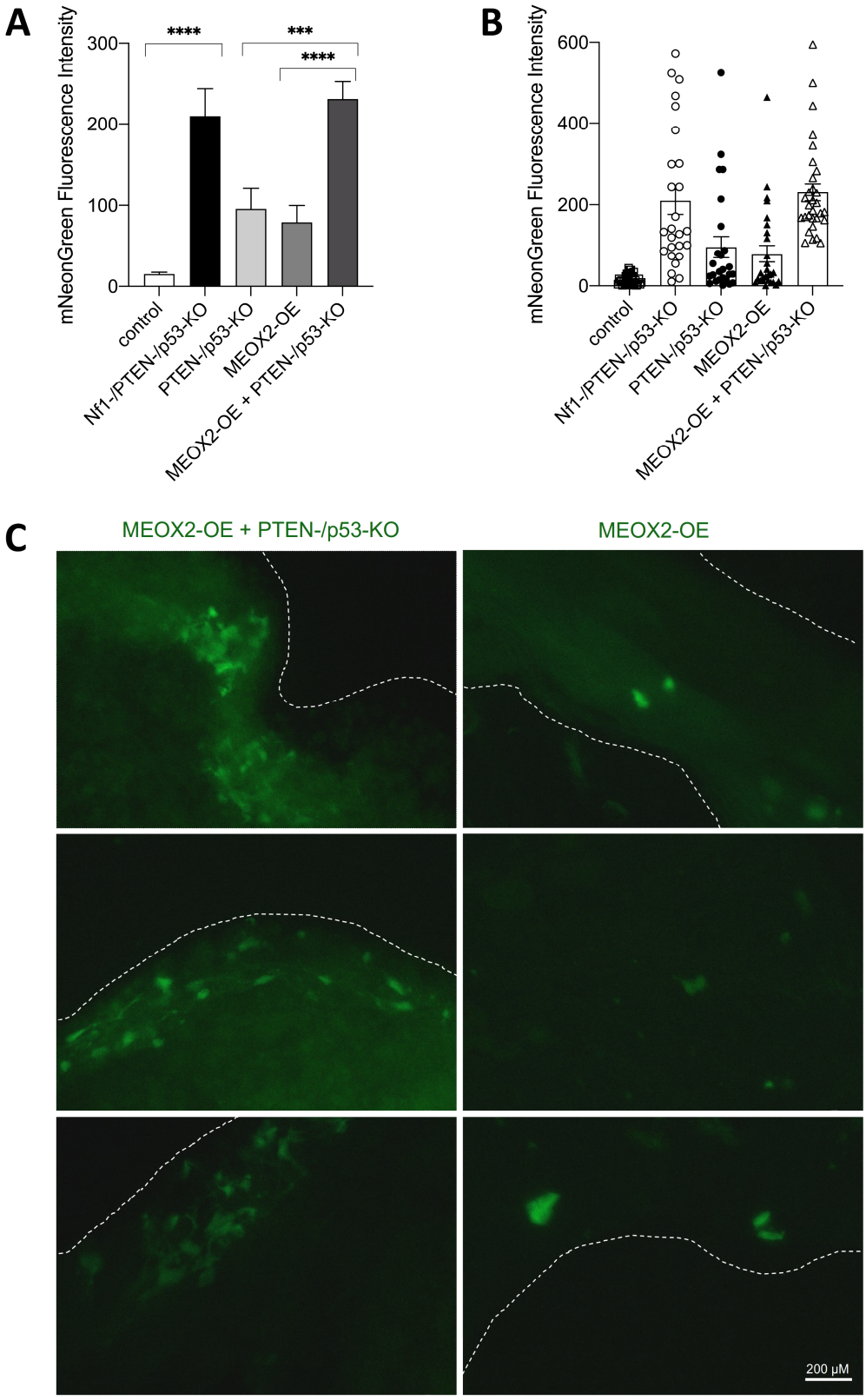

Figure 7: MEOX2 OE in cerebral organoids (CO).
A + B) mNeonGreen intensity measurement of CO after one month of culture post nucleofection using KO and/or MEOX2-OE plasmids. Samples shown from left to right: Control (n = 32), Nf1-/PTEN-/p53-KO (n = 26); PTEN-/p53-KO (n = 25); MEOX2-OE (n = 27), MEOX2-OE + PTEN-/p53-KO (n = 30); (mean ± SEM, unpaired T-test). C) Microscopy images of CO stained for MEOX2. MEOX2 OE + PTEN-/p53-KO (left) versus MEOX2-OE (right). Lines indicate outline of CO tissue. Bar size = 200 µM.

4.5 Mutagenesis of MEOX2 phosphorylation site S155 induces changes in MEOX2 nuclear localization *in vitro*

In addition to studies using MEOX2 expression to observe phenotypical changes in GBM correlating with MEOX2 *in vivo* and *in vitro*, I analysed phosphorylation sites of MEOX2 in context of GBM. Phosphorylation was reported to affect the activity of transcription factors on different levels (Holmberg, Tran, Eriksson, & Sistonen, 2002). It can enhance stability or degradation of a protein or affect the localization in the nucleus.

Phosphorylated sites of MEOX2 in GBM have not been identified before. I collaborated with the DKFZ mass spectrometry core facility to perform mass spectrometry analysis of MEOX2. I performed immunoprecipitation (IP) of FLAG-tagged exogenously overexpressed MEOX2 in HEK293TN cells, as well as IP of endogenously expressed MEOX2 in GBM cell line TS667. Mass spectrometry analysis revealed a novel phosphorylated site at S155, that was found to be phosphorylated in HEK293TN after MEOX2 OE as well as in GBM cell line TS667 (Table 21). This phosphosite is located at amino acid (AA) 155 of the protein sequence. The only known functional domain of the protein, the DNA binding homeobox domain, starts from AA 178 (Figure 8A) and is thus located 23 AA after the novel identified MEOX2 phosphorylation site. Following the serine (155) is a proline, leading to an SP pattern. The SP pattern is predicted to be phosphorylated by ERK kinases (Clark-Lewis, Sanghera, & Pelech, 1991; Gonzalez, Raden, & Davis, 1991). Since this site's phosphorylated state is conserved in GBM as well as in exogenously expressed MEOX2 in HEK293TN cells, I further investigated the importance of the described site. I cloned a phospho-mutant with an alanine substitution instead of serine at position 155, leading to an at all times non-phosphorylated site at this position. I observed protein degradation using a cycloheximide (CHX) induced assay. CHX inhibits protein synthesis by blocking eukaryotic translational elongation (Schneider-Poetsch et al., 2010). When MEOX2 or MEOX2-S155A were OE in HEK293TN, there was no difference to be observed in stability between both MEOX2 proteins after CHX treatment (Figure 8 B, C). Interestingly, in MEOX2-S155A transfected HEK293TN cells, there is a significant decrease in p21 expression observed 48 h after transient transfections (Figure 8 B, D). P21 is a known downstream target of MEOX2. The state of the phospho-site 155 affects the expression of the MEOX2 downstream target p21. Since phosphorylation status of the 155 site did not directly affect the stability of the MEOX2 protein, but still affected the expression of the downstream target p21, I next investigated the localization of MEOX2 protein within the cells. Phosphorylation of transcription factors can affect downstream activation not only by affecting protein stability, leading to longer activation state, but also by changing localization of the

transcription factor in the nucleus. Depending on nuclear localization, transcriptional activation of downstream targets, like p21 (Douville et al., 2011), can be affected (Grande, van der Kraan, de Jong, & van Driel, 1997; Vandromme, Gauthier-Rouvière, Lamb, & Fernandez, 1996). As MEOX2 is a transcription factor, it is important for the protein to be active in the nucleus to bind to its targets to induce or inhibit their transcription. When observing MEOX2 localization in MEOX2 and MEOX2-S155A transiently transfected HEK293TN cells using CLSM technique, I was able to observe a difference in MEOX2 localization when cells were transfected with MEOX2-S155A. I quantified the fluorescence labeled MEOX2 signal distribution within the nuclear envelope and nuclear laminar area to the distribution over the whole nucleus. For these analyses I was kindly provided a Fiji/ImageJ macro for analysis by the DKFZ imaging core facility. After analysis and quantification of both conditions, the wild-type MEOX2 protein was more evenly distributed within the whole nucleus, versus the distribution of the MEOX2-S155A phospho-mutant, which was located more towards the nuclear envelope (rim) of the nucleus. Wild-type MEOX2 protein showed a median rim/nucleus distribution of 106,2 % versus MEOX2-S155A phospho mutant showed a median of 123,1 %. These results indicate a significant increase in median distribution towards the rim of 15,9 % increased in MEOX2-S155A phospho mutant compared to wild-type MEOX2 protein distribution levels (Figure 8E, F). The role of the inner nuclear envelope, as a protein resting area for non activated transcription factors has been reported before (Heessen & Fornerod, 2007). Since MEOX2 is a transcription factor this shift could be connected to the activity of the protein binding to the open chromatin in the nucleus, leading to a less extensive activation of transcriptional downstream targets, as we observed from p21 as a MEOX2 downstream target.

Table 21: MEOX2 phosphorylation site

Position within protein	Amino acid	Phospho Probability
155	S	GRQALS(1)PAEAEKRSGGKRKSDSSDSQEGNY

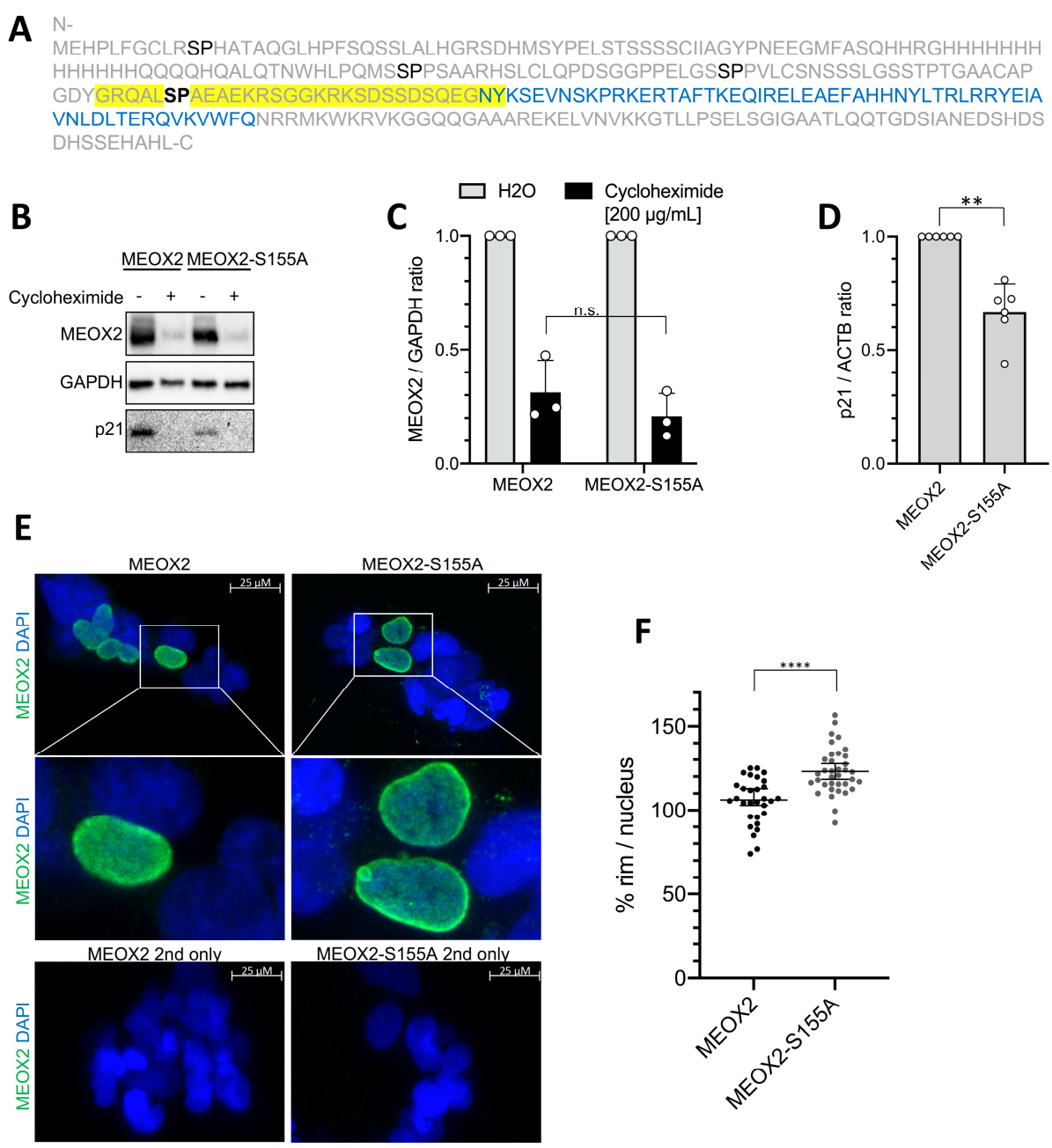

Figure 8: Effect of S155A mutation on MEOX2.
A) Structure of MEOX2. Yellow = region identified by mass spectrometry to be phosphorylated at S155 in HEK293TN and TS667 cell line after MEOX2 immunoprecipitation. SP indicates sites prognosed to be phosphorylated by ERK. Blue = homeobox domain of MEOX2. B) Stability of MEOX2 versus MEOX2-S155A in HEK293TN cells, 48 h after transient transfection and 24 h post cycloheximide treatment (200 µg/mL). C) MEOX2 (n = 3, 0,3 ± 0,14) and MEOX2-S155A (n = 3, 0,21 ± 0,1) levels normalised to GAPDH, 48 h after transient transfection and 24 h post cycloheximide treatment (200 µg/mL), Two-sided Welsh's test. D) p21 levels of MEOX2 (n = 6, 1 ± 0) versus MEOX2-S155A (n = 6, 0,67 ± 0,13) transfected HEK293TN cells, 48 h after transient transfection normalised to ACTB, Two-sided Welsh's test. E) MEOX2 (left) versus MEOX2-S155A (right) localization in HEK293TN cells 48 h after transient transfection. Immunofluorescence stainings using MEOX2 primary AB and Alexa488 secondary AB (top, middle) and secondary only (bottom), as a control. Blue = DAPI, green = MEOX2 signal. F), quantification of MEOX2 localization in HEK293TN cells 48 h after transient transfection with MEOX2 (black, n = 30 cells, median = 106,2 %) versus MEOX2-S155A (grey, n = 36 cells, median = 123,1 %). Localised signal in nuclear membrane (rim) divided by nuclear signal, median ± 95 % confidence interval, Two-sided Welsh's test.

4.6 RNA sequencing of *MEOX2* KD and *MEOX2* OE cell lines

4.6.1 RNA-seq of *MEOX2* KD cell lines

I focused further on the role of MEOX2 as a transcription factor to identify MEOX2 connected pathways in the GBM context. Therefore, I established MEOX2 KD cell lines using GBM with high endogenous MEOX2 levels and facilitating CRISPR/Cas9 technique to induce *MEOX2* KD. I used two individual CRISPR guides and a non-targeting control guide (Figure 17A, C). Experiment was performed in two different GBM cell lines (TS600 and TS667). I analysed changes in RNA transcription levels after RNA sequencing at the DKFZ genomics core facility and raw data analysis by Sevin Turcan, PhD.

After *MEOX2* KD using sg1 in TS667, 466 genes were significantly downregulated, and 503 genes were significantly upregulated. 556 genes were significantly downregulated, and 386 genes were significantly upregulated in TS667 cells after KD of *MEOX2* using sg2. The overlap between the downregulated genes cohorts of sg1 and sg2 datasets in TS667 cell line correlating with *MEOX2* KD is 230 genes (29 %) of all identified significantly downregulated genes. The overlap between the upregulated genes expression cohorts of sg1 and sg2 datasets in TS667 cell line negatively correlating with *MEOX2* KD is 125 genes (16,4 %) of all significantly identified upregulated genes from TS667 sg1 and sg2 data sets. After *MEOX2* KD using sg1 in TS600, 62 genes were significantly downregulated, and 68 genes were significantly upregulated. 99 genes were significantly downregulated, and 113 genes were significantly upregulated in TS600 cells after KD of *MEOX2* using sg2. The overlap between the downregulated genes cohorts of sg1 and sg2 datasets in TS600 cell line correlating with *MEOX2* KD is 22 genes (15,8 %) of all identified significantly downregulated genes. The overlap between the upregulated genes expression cohorts of sg1 and sg2 datasets in TS600 cell line negatively correlating with *MEOX2* KD is 19 genes (11,7 %) of all significantly identified upregulated genes from TS600 sg1 and sg2 data sets.

4.6.1.1 Identified deregulated pathways upon *MEOX2 KD* in GBM cell lines

I found several pathways to be significantly downregulated after *MEOX2* KD in GBM cell lines. Some pathways are downregulated in both analysed cell lines, despite their molecular differences: TS667 is a PDGFR amplified GBM cell line and TS600 is an EGFR amplified GBM cell line. Top deregulated pathways include: 1) Downregulation in hepatic fibrosis signalling pathway, 2) Downregulation of HOTAIR pathway, and 3) Regulation of epithelial to mesenchymal transition (EMT) in development (Figure 9A). Myofibroblast-mediated fibrotic

tissue remodeling can occur in most organs in end stages of diseases. This was reported in atherosclerosis, scleroderma, liver cirrhosis, renal fibrosis, heart failure, and also for cancer (Costa et al., 2018). HOTAIR is found overexpressed in multiple cancers, including GBM (Tang & Hann, 2018). The depletion of HOTAIR has been shown to inhibit GBM cell migration and invasion *in vivo*. Introduction of HOTAIR 5' domain induced β-catenin expression in human glioma-derived astrocytoma. Hence HOTAIR is a potential therapeutic target in GBM (Zhou et al., 2015). The EMT of cells is a crucial mechanism in development that is also appropriated by cancer cells. Increased secretion of extracellular matrix (ECM) components, such as collagens or β-catenin, increases cells‘ ability to further migrate and invade. EMT also increases resistance to apoptosis (Kalluri & Weinberg, 2009). Here I can demonstrate that multiple cancer associated pathways are dowenregulated upon MEOX2 KD in two different GBM cell lines *in vitro*.

4.6.1.2 Predicted upstream regulators

Using IPA, I also identified predicted upstream regulators in *MEOX2* KD cell lines using RNA-seq data described in 4.6.1. IPA upstream regulators are defined by multiple significantly up- or downregulated genes which can all be traced back to one common upstream target, being affected by *MEOX2* KD in the experimental setting, either by being inhibited or activated. Some MEOX2 upstream regulators were only identified in one of the cell lines (TS600 or TS667) after *MEOX2* KD.

ERK, a kinase involved in key pathways of cancer (Figure 3), NOTCH1, p38 MAPK, Snail, downstream targets were found deregulated in TS667 cell line (sg1, sg2) after MEOX2 KD, indicating them as inhibited upstream regulators of MEOX2. Estrogen receptor was predicted as an activated upstream regulator following MEOX2 KD (TS667-sg1, -sg2). EGFR and TGFB3 were predicted to be inhibited upstream regulators exclusively in TS600 cell line (sg1, sg2). As mentioned earlier, TS600 is an EGFR amplified cell line.

Some inhibited upstream regulators were predicted in both cell lines (TS600, TS667). PDGF BB (Figure 9C, TS667-sg1, -sg2, TS600-sg2) was identified. PDGF alterations are found in 15% - 20% of GBM, according to TCGA analysis (Farooqi & Siddik, 2015). p53 (Figure 9D, TS667-sg1, -sg2, TS600-sg1), is a known tumor suppressor. In PTEN/p53 KD organoid model, MEOX2 OE led to increased cell proliferation (Figure 7). NOTCH3 (TS667-sg2, TS600-sg2),

TWIST2 (TS667-sg1, -sg2, TS600-sg1), TP63 (TS667-sg1, -sg2, TS600-sg2) and TGFB1 (TS667-sg1, -sg2, TS600-sg2) were also identified.

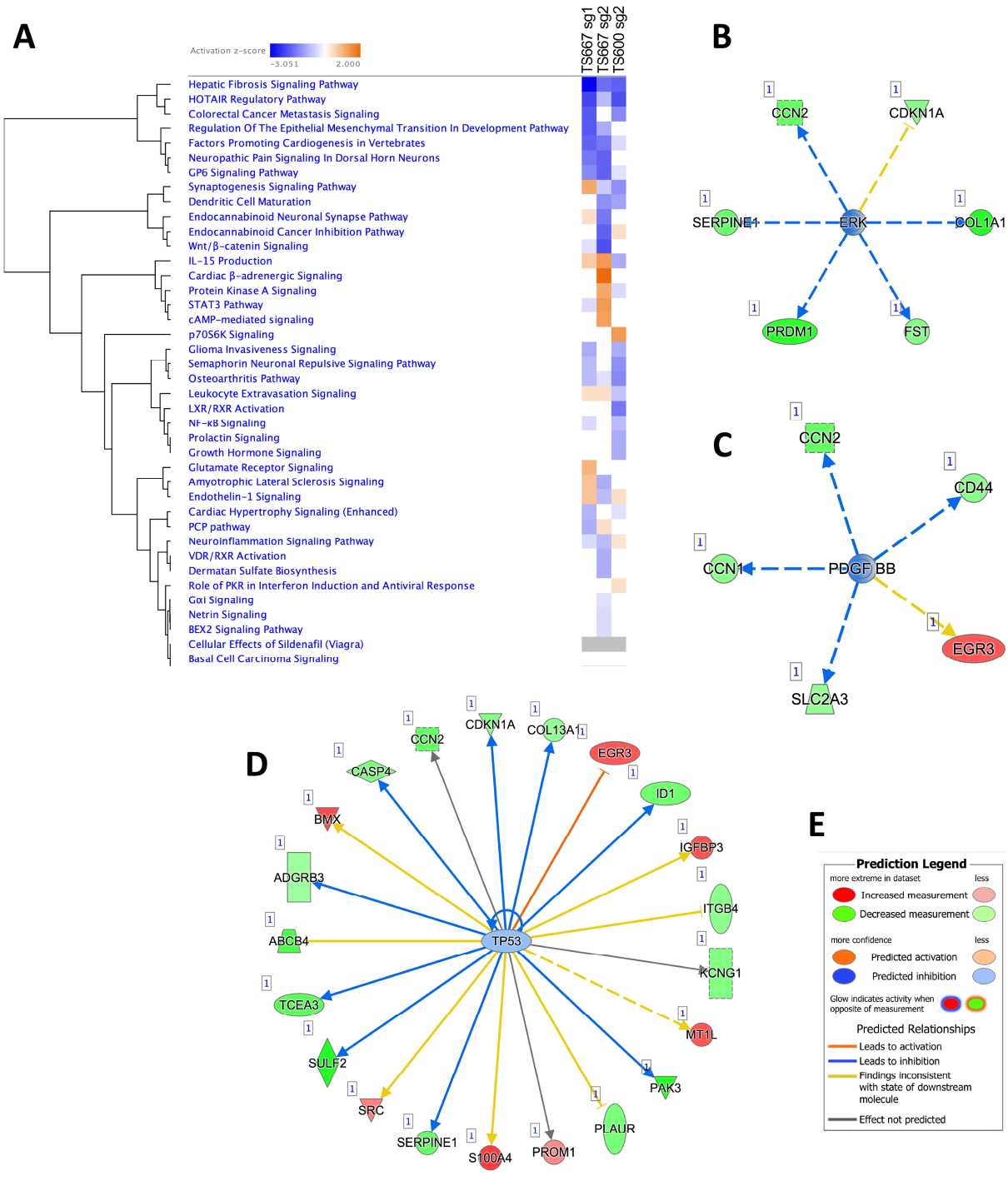

Figure 9: IPA analysis of MEOX2 KD RNA-seq data of GBM cell lines.
B–D: Upstream regulators identified in TS667 (and TS600) datasets, E: legend. A) Comparison analysis reveals common deregulated pathways between GBM cell lines TS667 and TS600 upon MEOX2 KD in both cell lines. Blue: downregulated pathways, orange: upregulated pathways, scale range from -3,051 to 2,0 z-score. B) ERK as potential upstream regulator of downstream regulated genes after MEOX2 KD in TS667-sg2. C) PDGF BB as potential upstream regulator of downstream regulated genes after MEOX2 KD in TS667-sg2. D) TP53as potential upstream regulator of downstream regulated genes after MEOX2 KD in TS667-sg2.

4.6.1.3 Predicted upstream regulator TGFB and identified associated pathways in cancer

An interesting upstream regulator found using IPA analysis on TS667 and TS600 RNA-seq data, is TGFB. TGFB is predicted to be an upstream regulator affected by *MEOX2* KD in both cell lines (TS667, TS600). TGFB1 deregulated multiple downstream targets that play roles in cell movement of melanoma cells (Figure 10C) where one partner is the estrogen receptor, which is a predicted activated upstream regulator itself identified in TS667 cell line (sg1, sg2). We also found the estrogen dependent gene expression to be a pathway deregulated after *MEOX2* KD in our TS600 ACT-seq data (Figure 14). TGFB1 downstream targets also regulate metabolism of polysaccharides (Figure 10D). It is known that TGFB induces metabolic reprogramming to drive EMT in cancer (W. Hua, ten Dijke, Kostidis, Giera, & Hornsveld, 2020). EMT in cancer favours cell's invasion capacity (Brabletz, Kalluri, Nieto, & Weinberg, 2018). Additionally I found the proliferation of stem cells (Figure 10 D), and binding of connective tissue cells / cell proliferation of squamous cell carcinoma cell lines via SMAD3, a TGFB downstream target itself, (Figure 10 E) to be pathways affected after MEOX2 KD in TS667 GBM cells (sg2). Multiple pathways found deregulated after *MEOX2* KD in TS667 cells, indicating TGFB to be a common upstream regulator, are known for their roles in cancer initiation and progression.

To confirm RNA-seq results on protein level I designed an experiment to determine, whether TGFβ stimulation affects downstream targets activation differently in the parental and the MEOX2-KD GBM cell lines *in vitro*. Preliminary data shows a difference in SMAD2 activation, measured by SMAD2 phosphorylation, correlating with MEOX2 expression. This response to TGFβ stimulation was observed in the TS600 cell line only.

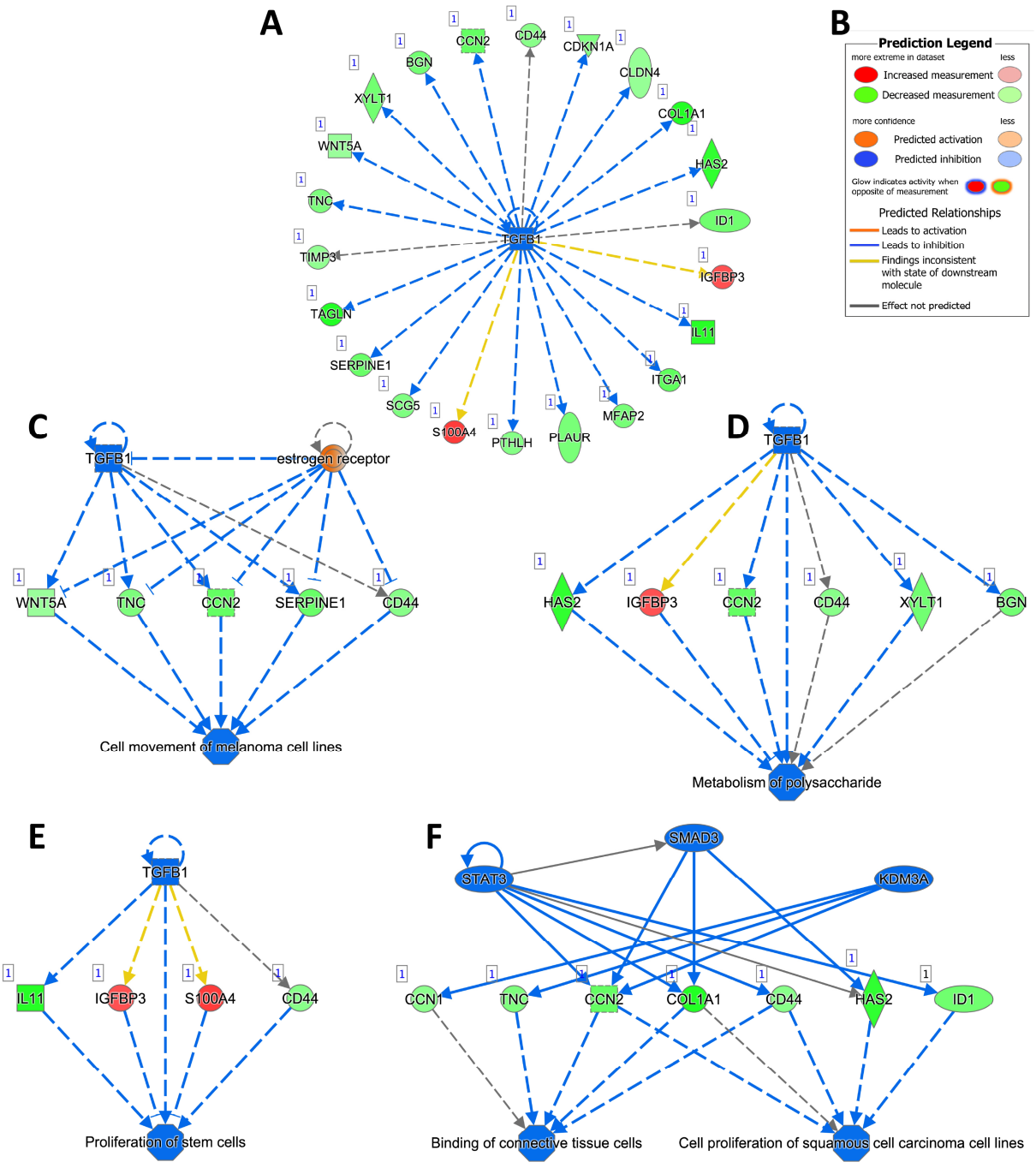

Figure 10: Predicted upstream regulator TGFB1 and associated pathways.
A–F: IPA analysis on TS667 GBM cell line after MEOX2 KD (sg2). A) TGFB1 predicted to be an upstream regulator after MEOX2 KD in TS667 GBM cell line. Map of downstream targets. B) IPA analysis legend. C) TGFB1 role in cell movement of melanoma cell lines. D) TGFB1 role in metabolism of polysaccharide. E) TGFB1 role in proliferation of stem cells. F) Role of SMAD3, TGFB1 downstream target, in binding of connective tissue cells and cell proliferation of squamous cell carcinoma cell lines.

4.6.2 RNA-seq of *MEOX2* OE cell lines

After performing RNA-seq analysis on TS667 and TS600 GBM cell lines with high endogenous MEOX2 expression after induced stable KD using CRISPR/Cas9, I next performed RNA-seq analysis on 080125 and 080512 cell lines with low endogenous MEOX2 expression levels, after stable viral transduction using a MEOX2 expression plasmid (Figure 6A). These two new model cell lines allow an observation of direct transcriptional changes induced by MEOX2 OE in GBM cell lines *in vitro*. Both cell lines were also xenograft transplanted *in vivo* into mice by me and my colleague Ashwin Narayanan, PhD where one of the lines (080125) showed phenotypically changes in cell growth *in vivo* upon MEOX2 OE (Figure 6B, C, D). I performed RNA-seq analysis comparing the MEOX2 OE model to vector only transduced cells using IPA program (Ingenuity pathway analysis–Quiagen). Sequencing was performed at the DKFZ genomics core facility and raw data analysis was performed by Sevin Turcan, PhD.

4.6.2.1 Identified deregulated pathways upon *MEOX2* OE in GBM cell lines

1602 genes were significantly downregulated after MEOX2 OE in 080125 cell line. 1212 genes were upregulated after MEOX2 OE in 080125. In 080512 cell line, 987 genes were downregulated after MEOX2 OE and 1402 genes were upregulated after MEOX2 OE. Overlap between downregulated genes found correlating with MEOX2 OE in 080125 and 080512 cell lines are 434 genes (19,9 %). Overlap of upregulated genes correlatong with MEOX2 OE in 080125 and 080512 cell line is a cohort of 646 genes (33,1 %).

Using IPA analysis software, I identified a clear pattern of coherent pathway deregulation. Top downregulated pathways upon MEOX2 OE include 1) Oxidative Phosphorylation, 2) PTEN Signaling, and 3) EIF2 Signaling. PTEN is a known tumor supressor often times downregulated or non-functional in cancers (Worby & Dixon, 2014). In our cerebral organoid experiments PTEN was identified as a key driver gene that lead to significant increase in cell proliferation upon double KD with p53 and parallel MEOX2 OE (Figure 7). As observed earlier, MEOX2 OE alone as well as PTEN, p53 KD alone could not induce a similar proliferative phenotype as the triple KD or combined PTEN/p53 loss and MEOX2 OE. Finding PTEN Signaling pathway downregulated upon exogenous MEOX2 OE in GBM cell lines strengthens MEOX2 role in tumor proliferation.

Top upregulated pathways correlating with MEOX2 OE include 1) Synaptogenesis Pathway, 2) GP6 Signalling Pathway, 3) Hepatic Fibrosis Signalling Pathway and 4) Glioblastoma

Multiforme Signaling (Figure 11). Interestingly two of these top upregulated pathways, after MEOX2 OE in GBM with low endogenous MEOX2 expression (080125, 080512) showed a correlation in reduced expression level after MEOX2 KD in GBM cell lines with high endogenous MEOX2 expression (TS600, TS667), highlighting MEOX2 connection to Hepatic Fibrosis Pathway and GP6 signaling. GP6 is a member of the immunoglobulin superfamily and is expressed in platelets and their precursors megakaryocytes. It is a major signaling receptor for collagens, activating the PI3K/AKT/mTOR pathway (Figure 3).

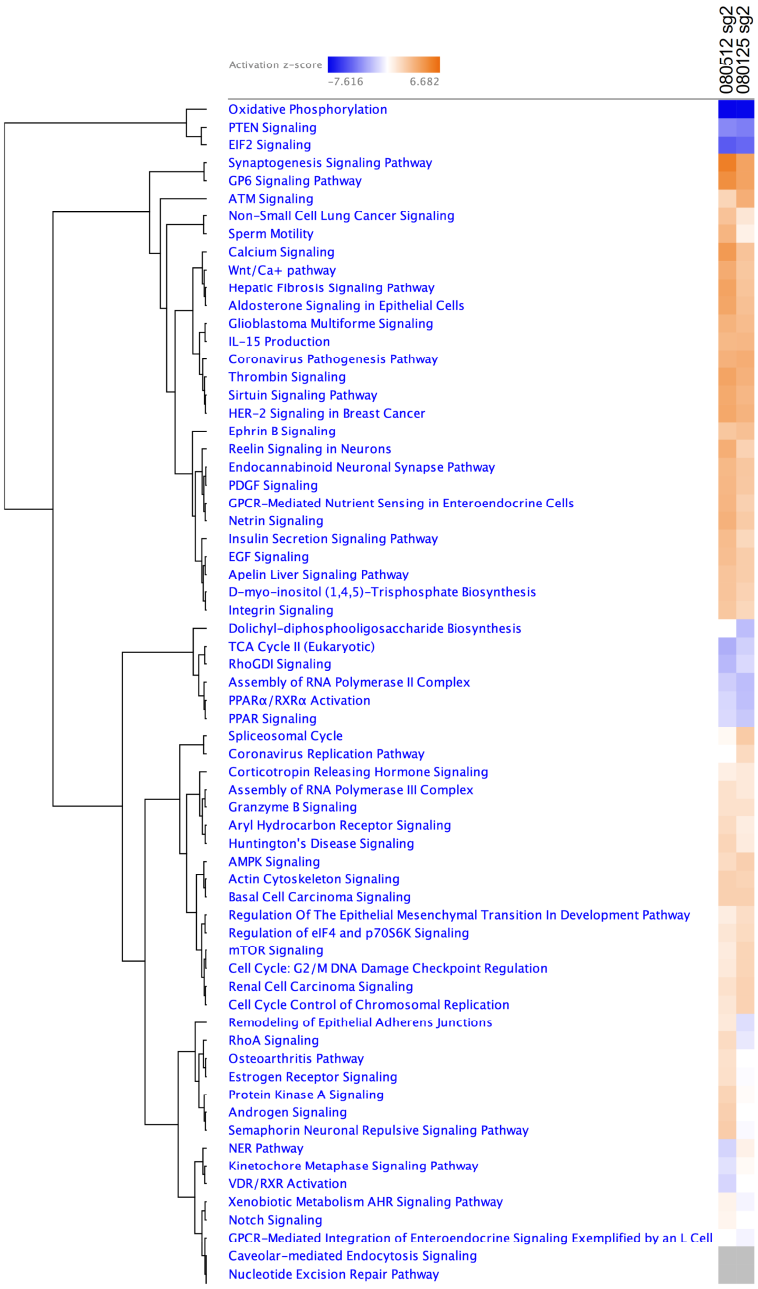

Figure 11: IPA analysis of MEOX2 OE RNA-seq data of GBM cell lines.
Comparison analysis reveals common deregulated pathways between GBM cell lines 080512 and 080125 upon MEOX2 OE in both cell lines. Blue: downregulated pathways, orange: upregulated pathways, grey: up– and downregulated genes identified, scale range from -7,616 to 6,682 z-score.

4.6.2.2 Predicted upstream regulator RICTOR

A common upstream regulator identified using the IPA software on the datasets of gene deregulation after MEOX2 OE in 080125 as well as 080512 cell lines was RICTOR. RICTOR activity is predicted to be upregulated correlating with MEOX2 OE in both datasets. RICTOR is part of the mTOR pathway (Figure 3), more precisely a core component of the mechanistic target of rapamycin complex 2 (mTORC2) signaling complex, which is a key player in proliferation and cell survival of tumor cells. It was reported that glucose or acetate are required for EGFR, the most commonly altered receptor in GBM (Table 20), to activate mTORC2. Glucose or acetate promoted signaling is facilitated through acetyl-CoA-dependent acetylation of RICTOR. When upstream components of EGFR signaling pathway are no longer active, RICTOR acetylation can be maintained in high glucose levels, forming an autoactivation loop of mTORC2. This can lead to the resistance of GBMs towards EGFR-, PI3K-, or AKT-targeted therapies. With this function of RICTOR, mTORC2 describes a central node between growth factor signaling and nutrient availability in GBM (Masui et al., 2015).

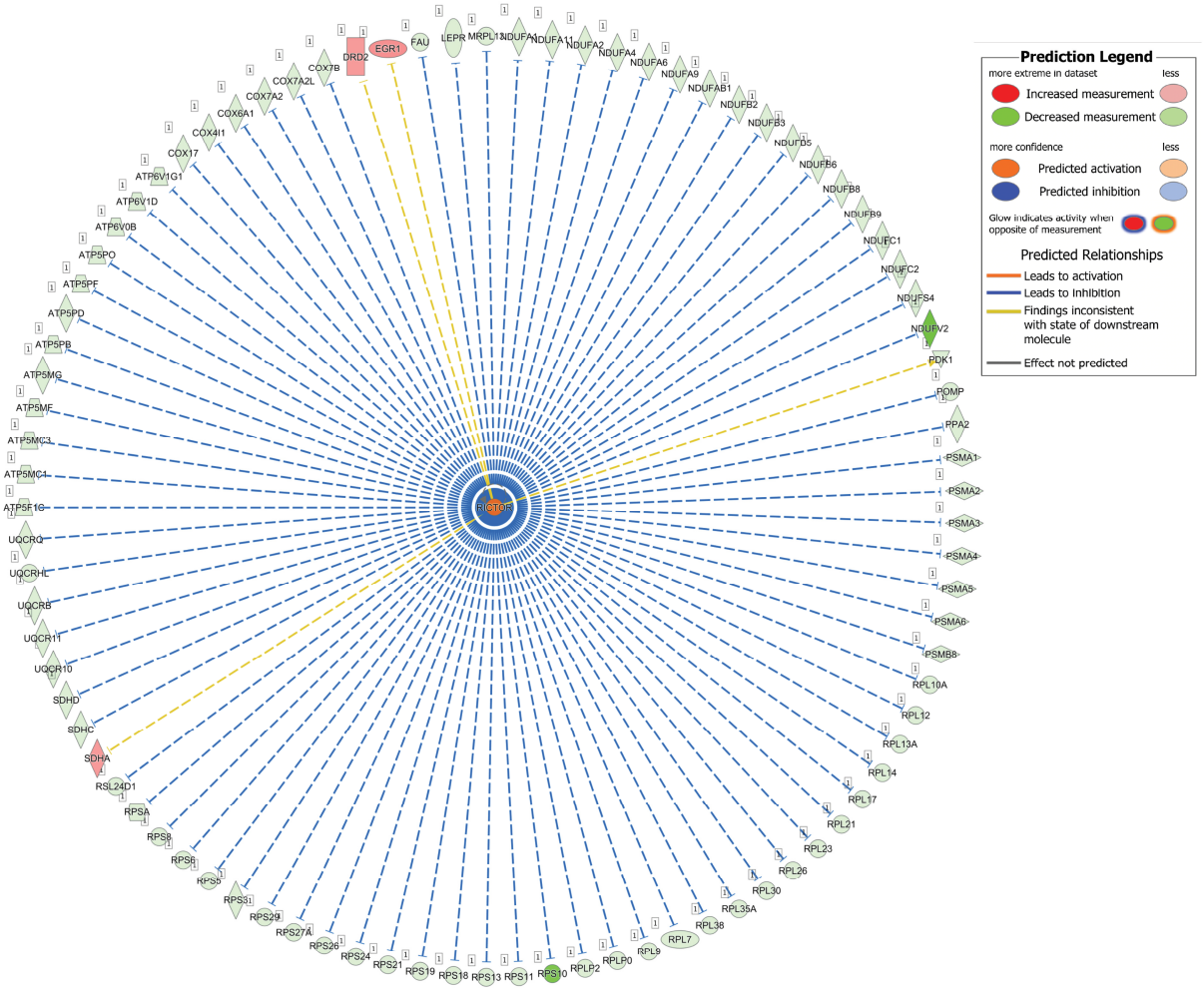

Figure 12: RICTOR predicted upstream regulator upon MEOX2 OE in 080125 and 080512.
Left: *RICTOR* activity is predicted to be upregulated upon MEOX2 OE in 080125 and 080512. Predicted as an upstream regulator of several genes. Right: Legend.

4.6.3 RNA-seq analyses comparison of *MEOX2* KD and *MEOX2* OE in GBM cell lines

Interestingly, I found an inverse correlation between transcriptional changes in TS667, TS600 cell lines, after MEOX2 KD, and 080125, 080512 cell lines, after MEOX2 OE. The significantly deregulated genes in common over all mentioned cell lines include: MEOX2, NOTCH3 and NRCAM. NOTCH3 and NRCAM were downregulated in TS667, TS600 after MEOX2 KD and upregulated in 080125, 080512 after MEOX2 OE. Both, NOTCH3 and NRCAM are involved in EMT. In line with these results, changes in multiple ECM genes like collagens can be observed in all cell lines after manipulation of MEOX2 expression.

4.7 Identification of MEOX2 DNA binding targets

4.7.1 ACT-seq on GBM cell lines TS600 and TS667

Following the RNA-seq analysis, which pointed out significant deregulation of several pathways by MEOX2 KD in GBM cell lines, I continued to identify the DNA binding targets of MEOX2 in GBM cell lines. Previously, no DNA binding targets of MEOX2 were identified *in vitro* using GBM cell lines. MEOX2 is expected to alter the transcription levels of its binding targets, either by activating or inhibiting them. I collaborated with Dr. Dieter Weichenhan and Marion Bähr to execute ACT-seq experiments under their supervision within the lab of Dr. Christoph Plass at the DKFZ Heidelberg. Analysis of raw data was performed by Sevin Turcan, PhD. The NTC samples showed generally a higher gene binding, measured by reads, than the MEOX2 KD cell lines used as control for the experiments (Figure 13 A, Figure 20 A). We were able to identify MEOX2 binding targets in TS600- and TS667-NTC when compared to two different CRISPR/Cas9 induced MEOX2 KD lines (sg1, sg2). In TS600, most DNA binding of MEOX2 was found in distal intergenic (39 %) and intronic regions (38 %). 17 % of peaks were found in promoter region, followed by 3 % in exons and 1,5 % in 3'UTR. Overall, <1 % of peaks were located in either 5'UTR and downstream regions (Figure 13 B). TS667 had a lower promoter binding coverage. The binding distribution showed 47 % peaks in intronic and 45 % distal intergenic, followed by 3,6 % promoter binding and 2 % Exon binding. 3'UTR had 1,2 % binding. Downstream and 5'UTR had both <1 % binding (Figure 20 B).

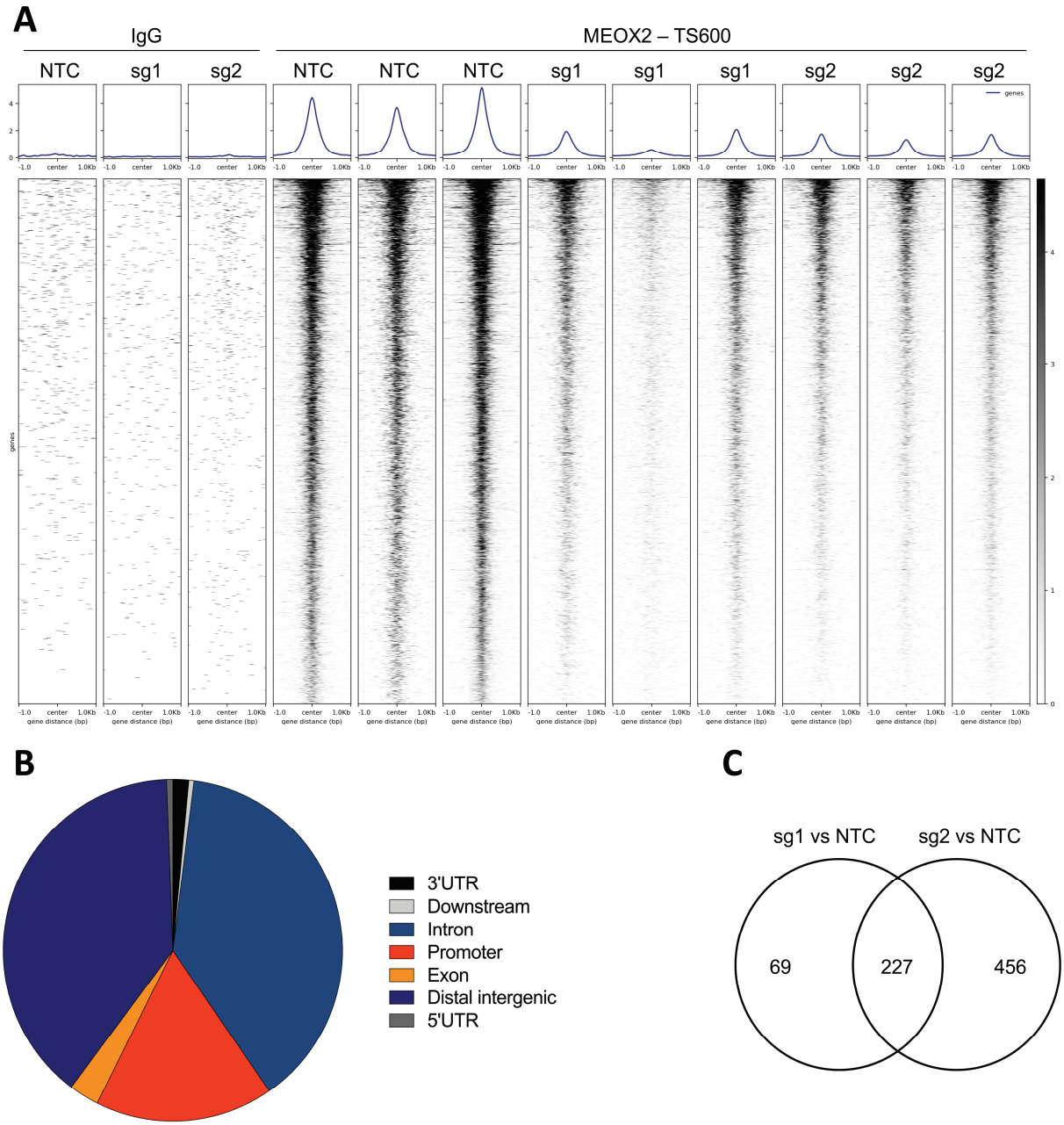

Figure 13: MEOX2 binding targets identified using ACT-seq in TS600 patient derived tumorsphere cell line.
A) IgG controls (lane 1–3) and MEOX2 binding reads in TS600 NTC control GBM cell line (lane 4–6) versus two individual CRISPRcas9 sg KD lines (lane 7–9, lane 10–12). B) Binding of MEOX2 analysed by DNA region. 3'UTR: 1,5 %, Downstream: <1 %, Intron: 38 %, Promoter: 17 %, Exon: 3 %, Distal intergenic: 39 %, 5'UTR: <1 %. UTR = untranslated region. C) Overlap (227) of promoter bound target genes identified in NTC versus sg1 (296, left) and NTC versus sg2 (683, right).

4.7.1.1 MEOX2 regulated pathways identified by ACT-seq in GBM cell line

We further analyzed the TS600 cell line that showed higher percentage of promoter binding. We identified an overlapping cohort of 227 genes after normalising NTC binding over sg1 or sg2 KD (Figure 13C). Pathway analysis of this cohort shows significant downregulation of p53-related DNA target binding, such as NDRG1 (Figure 14), indicating p53 as the top deregulated pathway after MEOX2 KD (Figure 14A). Interestingly, we also identified a connection between MEOX2 and p53 signaling on RNA level (Figure 9) and in context of organoid experiments

(Figure 7), as described earlier. Other deregulated pathways identified from our ACT-seq dataset include signaling by nuclear receptors, ESR-mediated signaling, Estrogen-dependent gene expression (related to cancer), and others. One of the deregulated pathways is the MAPK targets / Nuclear events mediated by MAP kinases (Figure 14). This goes in line with our earlier finding of ERK being one of the upstream regulators identified by IPA analysis (Figure 11).

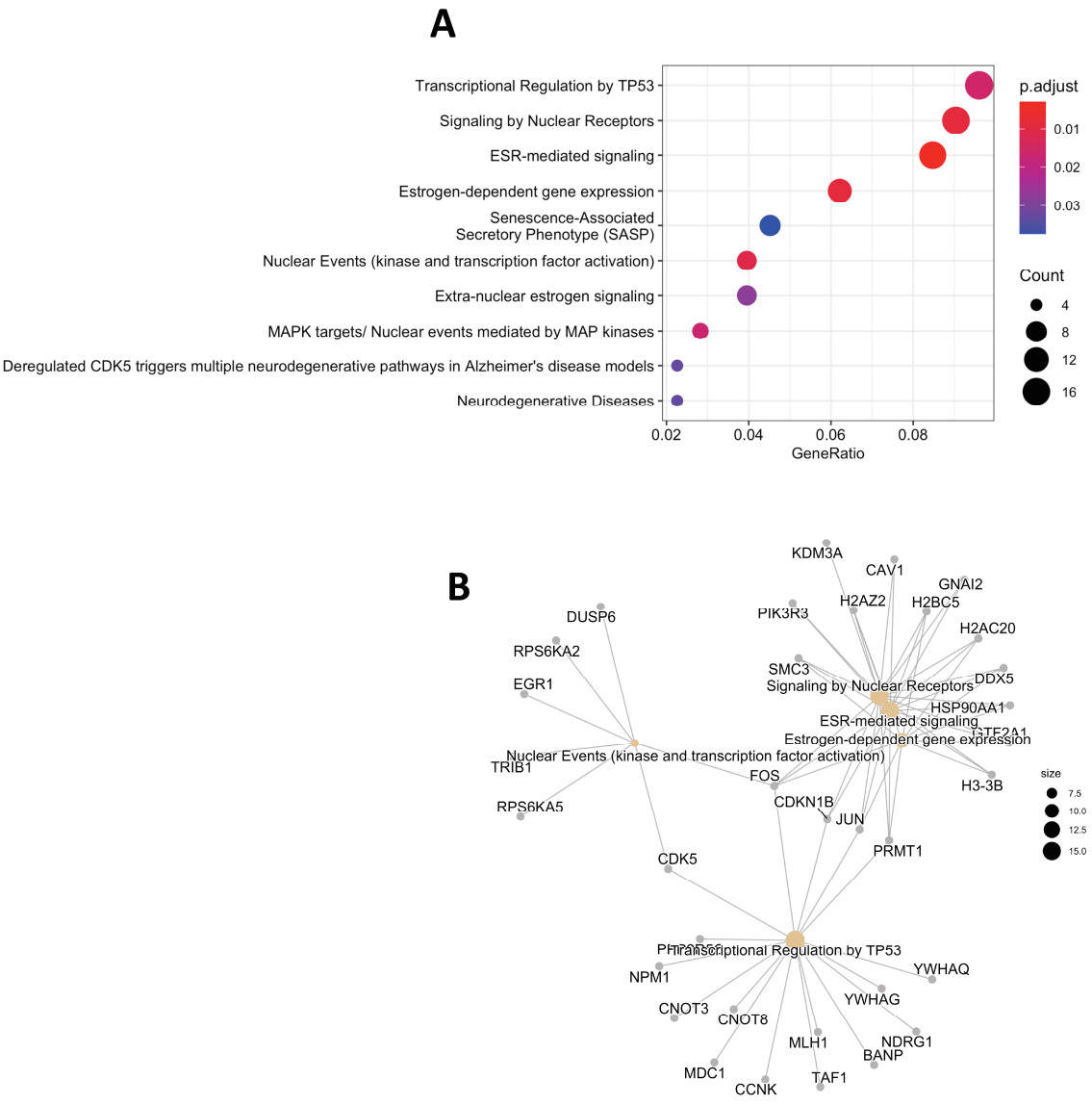

Figure 14: Deregulated pathways upon *MEOX2* KD in GBM cell line TS600 identified by ACT-seq analysis of MEOX2 DNA binding targets.
A) Deregulated pathways sorted by adjusted p–value, Gene ratio between control and KD cell lines and gene counts. B) String diagram of deregulated pathways and associated MEOX2 binding genes identified in TS600 cell line.

4.7.1.2 MEOX2 binding targets identified by ACT-seq in GBM cell lines

In TS600 cell line, 315 genes showed significant binding of MEOX2 over sg-2 KD control in their promoter region. Direct binding targets of interest include DUSP6, a negative regulator of the mitogen-activated protein (MAP) kinase, inactivating ERK by dephosphorylating the phosphoserine/threonine and phosphotyrosine residues. Also ETV4 and ETV5, which belong to the ETS-family of proteins, a well-known family of oncogenic transcription factors that has been reported to be less active by increased p53 activity as p53 increase decreases ETV protein degradation (Sizemore, Pitarresi, Balakrishnan, & Ostrowski, 2017). Lastly, SPRY4, an inhibitor of MAPK signaling, was also identified as a direct binding target of MEOX2. In TS667 cell line only 40 genes showed significant binding of MEOX2 in promoter region normalised to sg2-KD as a control. Direct binding targets include DUSP16, which has similarly to DUSP6 a function as negative regulator of ERK.

When I compared direct binding targets identified in TS600 and TS667 cell lines and identified an overlap of five genes, that were affected in their binding to the promoter region after MEOX2 KD (LARS2-AS, TM4SF, BBS9, BHLHE40-AS1, SNHG10).

4.7.2 MEOX2 DNA binding targets transcriptionally downregulated upon *MEOX2* KD

Significant downregulation of genes transcription after *MEOX2* KD in GBM cell lines indicates their potential regulation via MEOX2. Additional identification of same genes as direct binding targets of MEOX2 in the same cell line strengthens the hypothesis of *MEOX2* as a direct regulator of these targets.

When comparing the TS667 ACT-seq findings to TS667 RNA-seq results, I observe TAGLN3 gene to be bound by MEOX2 in the promoter region as well as being downregulated in TS667 cell line after *MEOX2* KD (using sg1 or sg2 KD). This indicates a regulation of TAGLN3 by MEOX2 transcription factor. TAGLN3 is an early marker for post-mitotic neurons (Ratié, Ware, Jagline, David, & Dupé, 2014). It is shown to bind filamentous actin (F-actin) an well as intracellular actin in neural cells (Mori et al., 2004). Additionally, I identified genes that are bound in other DNA regions than promoter regions, and deregulated on RNA level, as this can still indicate a direct effect of MEOX2 binding on gene expression. Identified genes in TS667 ACT-seq findings correlating with TS667 RNA-seq results include a cohort of 28 genes, deregulated after sg1 and sg2 *MEOX2* KD and ACT-seq dataset, as well as additional 48 genes

overlapping between sg1 KD with ACT-seq results and 33 genes overlapping between sg2 KD and ACT-seq results.

When comparing the newly found DNA binding sites of MEOX2 in TS600 cells to the TS600 RNA-seq results, I identified two genes that show correlation between ACT-seq binding in the promoter region and RNA level downregulation after *MEOX2* KD (using sg1 or sg2 KD). These genes include S100A6 and LTBP1. S100A6 is a Ca^{2+}-binding protein, involved in cellular functions like cell cycle progression, differentiation, apoptosis, cytosceletal dynamics and stress response (Donato, Sorci, & Giambanco, 2017). It is expressed in normal adult tissue and in several tumor types (H. Chen, Xu, Jin, & Liu, 2014; X. Chen et al., 2015; Lyu et al., 2015; Tamai et al., 2014; Tamai et al., 2012; M. Zhao et al., 2016). It can be released by certain cell types, pointing to extracellular functions of the protein, and dosage of serum S100A6 levels might aid in diagnosis in oncology (Cross, Hamdy, Deloulme, & Rehman, 2005; Ito et al., 2005).

Latent Transforming Growth Factor Beta Binding Protein 1 (LTBP1) codes for a protein that can activate latent complexes of TGFβ so they can move to the extracellular matrix, where the latent cytokine becomes activated. LTBP1 has been shown to be involved in tumorenvironment regulation in tumor cells and specifically in GBM cells where gene expression also correlates with GBM patient survival by TCGA data analysis (Liu et al., 2019). LTBP1 downregulation was shown to decrease mesenchymal phenotypes and inhibited TGFβ-induced EMT in esophageal squamous cell carcinoma where studies suggest an oncogenic role of LTBP1 (Cai et al., 2020). Studies also identified LTBP2 silencing, a paralog of LTBP1, to suppress proliferation, migration, invasion and EMT in gastric cancer cells which makes LTBP2 a promising prognostic biomarker and potential therapeutic target (J. Wang et al., 2018).

Additionally, as described for TS667 cell line, I identified genes that are bound in DNA regions other than promoter regions, and deregulated on RNA level, as this can still indicate a direct effect of MEOX2 binding on gene expression. The identified correlating genes between TS600 ACT-seq findings and TS600 RNA-seq results after sg2 *MEOX2* KD include a cohort of 28 genes, including NRCAM, which was found downregulated in both, TS600 and TS667 cell line upon MEOX2 sg2 KD and upregulated in 080125 and 080512 upon MEOX2 OE. Comparing RNA-seq data of sg1 *MEOX*2 KD to ACT-seq results identified a cohort of 10 overlapping genes. Additionally, three genes are found downregulated in RNA-seq datasets of both sg1 and

sg2 KD in TS600 correlating with a non-promoter located binding of MEOX2 in ACT-seq data. These genes include CLU, EGFLAM, and interestingly, EGFR.

4.7.3 Identified MEOX2 DNA binding targets *in vivo*

4.7.3.1 CUT&Tag on patient GBM samples

To identify *in vivo* MEOX2 DNA binding sites in GBM, we received fresh frozen tumor samples of GBM patients from Dr. K. Ozduman. A. Narayanan performed CUT&Tag experiements and identified one tumor sample with high MEOX2 expression. We identified 2187 binding targets of MEOX2 that were statistically enriched over the IgG CUT&Tag from the same sample. Most DNA binding of MEOX2 was found in intronic region (42 %) and distal intergenic region (29,5 %). 24,5 % of peaks were found in promoter region, which is the most relevant for transcriptional activation, followed by 1,7 % in exon region and 1,3 % in 3'UTR and <1 % in downstream and 5'UTR. Similar distribution was found in our *in vitro* ACT-seq experiments using TS600 patient derived GBM cell line (Figure 13).

4.7.4 Comparison of *in vitro* and *in vivo* binding targets of MEOX2

Previous ACT-seq of TS600 sg2 over NTC revealed 1855 genes bound to MEOX2 (315 in promoter region). Overlap between CUT&Tag and TS600 ACT-seq sg2 reveals 184 genes (6 %), of which 19 are bound in promoter region. ACT-seq of TS667 sg2 over NTC revealed 1116 genes bound to MEOX2 (40 in promoter region). Overlap between CUT&Tag and TS667 ACT-seq sg2 reveals 178 genes (7,2 %), of which 10 are bound in promoter region. 49 genes are found in both ACT-seq cohorts (TS667 and TS600) as well as CUT&Tag cohort. Two of which were found bound in the promoter region in in all three experiments, using TS600, TS667 and patient material (LARS2-AS, BHLHE40-AS1). A cohort of 17 overlapping genes bound in promoter region was identified between ACT-seq of TS600 and CUT&Tag, and a cohort of 8 overlapping genes bound in promoter region was identified between ACT-seq of TS667 and CUT&Tag results.

All three cohorts show significant binding of DUSP10, ETV1, ETV5, SPRY 2 and MAP2, even though not all cohorts bind these targets specifically in the promoter region, a regulatory role of MEOX2 binding is possible. Additionally, TS600 ACT-seq and CUT&Tag results show binding of NRCAM, which was identified as one of two genes deregulated upon MEOX2 KD in TS600 and TS667 cell lines as well as MEOX2 OE in 080125 and 080512 cell lines. Further

binding targets in common between these two cohorts are EGFR, which was also identified to be downregulated in RNA-seq data of TS600 cell line (sg1, sg2) and EGFR-AS1, which might not be identified in TS667 cell line due to the lack of EGFR amplification. Also, ARID1A member of the SWI/SNF family, was identified. DUSP6, negative regulator of ERK, was also identified as well as MEOX1.

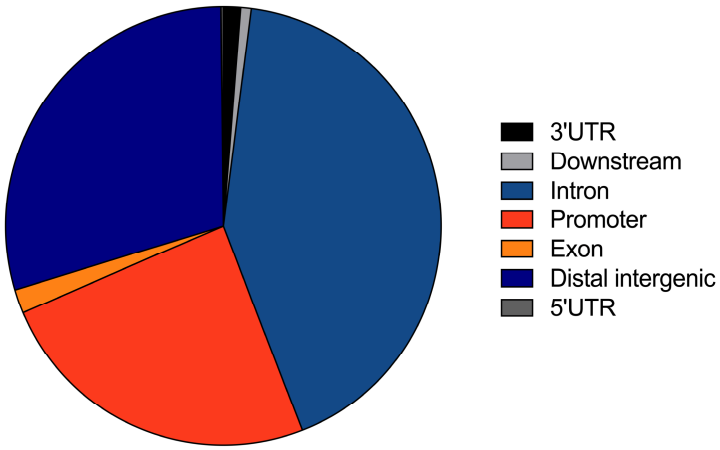

Figure 15: *In vivo* binding of MEOX2 analysed by DNA region.
3'UTR: 1,3 %, Downstream: <1 %, Intron: 42 %, Promoter: 24,5 %, Exon: 1,7 %, Distal intergenic: 29,5 %, 5'UTR: <1 %.
UTR = untranslated region.

4.8 MEOX2 induces phosphorylation of ERK *in vitro*

I identified ERK as a predicted MEOX2 upstream regulator of multiple significantly deregulated genes, using RNA-seq data of *MEOX2* KD (Figure 9), as well as identified a functional phosphorylated site in MEOX2 that is predicted to be phosphorylated by ERK (SP pattern, Figure 8A) and finally identified the MAPK pathway to be downregulated after *MEOX2* KD in ACT-seq results (Figure 14), indicating binding of MEOX2 to MAPK pathway genes. Therefore, I further investigated the effect of MEOX2 on ERK pathway activation. ERK pathway is a known pathway to often times be deregulated in cancer (Figure 3), leading to increased proliferation of tumor cells. It is also upstream of ETV4, which is part of the ETS family of transcription factors. Multiple ETS members (ETV1, ETV4, ETV5) were identified as MEOX2 binding targets in ACT-seq and CUT&Tag results. ERK pathway is also regulated by p53, which we found necessary to be knocked down in our CO model to unravel the fast proliferating phenotype induced by MEOX2 expression in IPSC (Figure 7). P53 was also the top pathway affected by MEOX2 KD from ACT-seq results (Figure 14).

I designed an experiment to elucidate if MEOX2 expression can affect the activation of ERK. Therefore, I overexpressed MEOX2 and MEOX2-S155A phospho-mutant, that I showed to be distributed differently within the nucleus than the naïve MEOX2 protein before (Figure 8E, F), in HEK293TN cells. Interestingly, I observed significant increase of phosphorylation of ERK after MEOX2 OE (Figure 16A, B). The MEOX2-S155A phospho-mutant showed significantly reduced activation of ERK, as measured by reduced ERK phosphorylation. With the MEK inhibitor trametinib, I additionally showed that these observations are rooted within the MAPK pathway, as the effect of activation was reversed by use of MEK inhibitor (Figure 16 A). MEK kinase being upstream of ERK. Interestingly, I once again observed the decrease in p21 activation after MEOX2-S155A OE versus MEOX2 OE (Figure 16A, C). Moreover, the activation of p21 by MEOX2 OE can also be observed to be regulated via MEK, as the use of MEK inhibitor trametinib reversed the p21 expression levels significantly (Figure 16A, C). As the HEK293TN cell line has an SV40 promoter, connected to p53 deregulation, and as it is commonly used for virus production for transduction, I performed MEOX2 OE in HEK293 cells, too, where I observed the same effect of increased ERK phosphorylation after MEOX2 OE as well as increased p21 activation. Both effects were reversed by the MEK inhibitor trametinib (Figure 22).

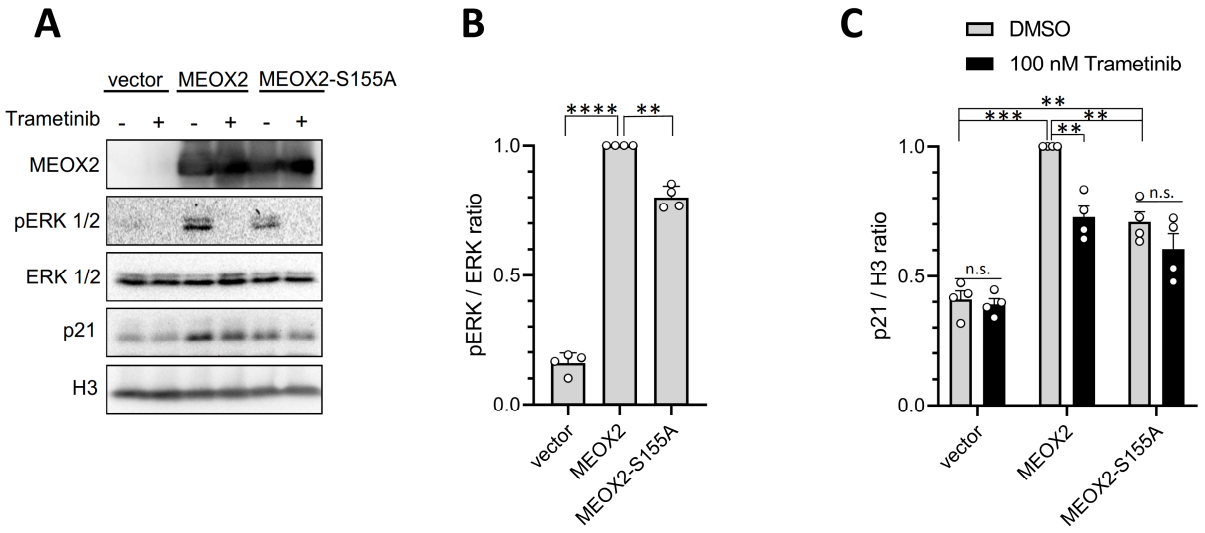

Figure 16: Phosphorylation of ERK induced by MEOX2 in HEK293TN cells.
A) Western Blot of MEOX2 (lane 2, 3), MEOX2-S155A (lane 4, 5) and control (lane 1, 2) transfected HEK293TN cells. 48 h after transient transfection and 24 h after trametinib treatment (+ = 100 nM) or DMSO treatment for control (-). B) Quantification of pERK to ERK expression in vector (n = 4, mean + SD), MEOX2 (n = 4, mean + SD) and MEOX2-S155A (n = 4, mean + SD) expressing HEK293TN cells. Two-sided Welsh's test. C) Quantification of p21 to H3 expression in vector + Trametinib (n = 4, mean + SD), – Trametinib (n = 4, mean + SD); MEOX2 + Trametinib (n = 4, mean + SD), – Trametinib (n = 4, mean + SD) and MEOX2-S155A + Trametinib (n = 4, mean + SD), – Trametinib (n = 4, mean + SD) expressing HEK293TN cells (n = 4, mean + SD, Two-sided Welsh's test.

To project these findings into the GBM context, I used the cell lines TS667 and TS600, to investigate the effect of MEOX2 on ERK phosphorylation. As basal phospho-ERK (pERK) levels are low in both parental cell lines (Figure 17), I induced the MAPK pathway by starving the TS667-NTC /TS667-sg1/TS667-sg2 as well as TS600-NTC/TS600-sg1/TS600-sg2 cell lines of EGF for 48 hours, followed by the addition of EGF in the media (50 ng/mL). EGF is a known factor binding to, and activating, the most upstream target of the MAPK pathway, the EGFR. To observe whether there is a difference in ERK activation correlated with MEOX2 expression levels, indicated by change in phosphorylation status of ERK, I harvested cells at different time points after EGF treatment. Interestingly, I found a significant difference in ERK activation when comparing the TS667-NTC cell line to the each of the two individual MEOX2 KD TS667 cell lines, inducing a MEOX2 KD after CRISPR/Cas9 single guide transductions (Figure 17A, B). The TS667-NTC cell line shows significantly higher ERK activation compared to the KD cell lines after 10 min and 30 min of treatment. In the other line used, TS600, there was no such effect to be observed (Figure 17C, D). MEOX2 can affect the signalling intensity of MAPK pathway within GBM cell line *in vitro.*

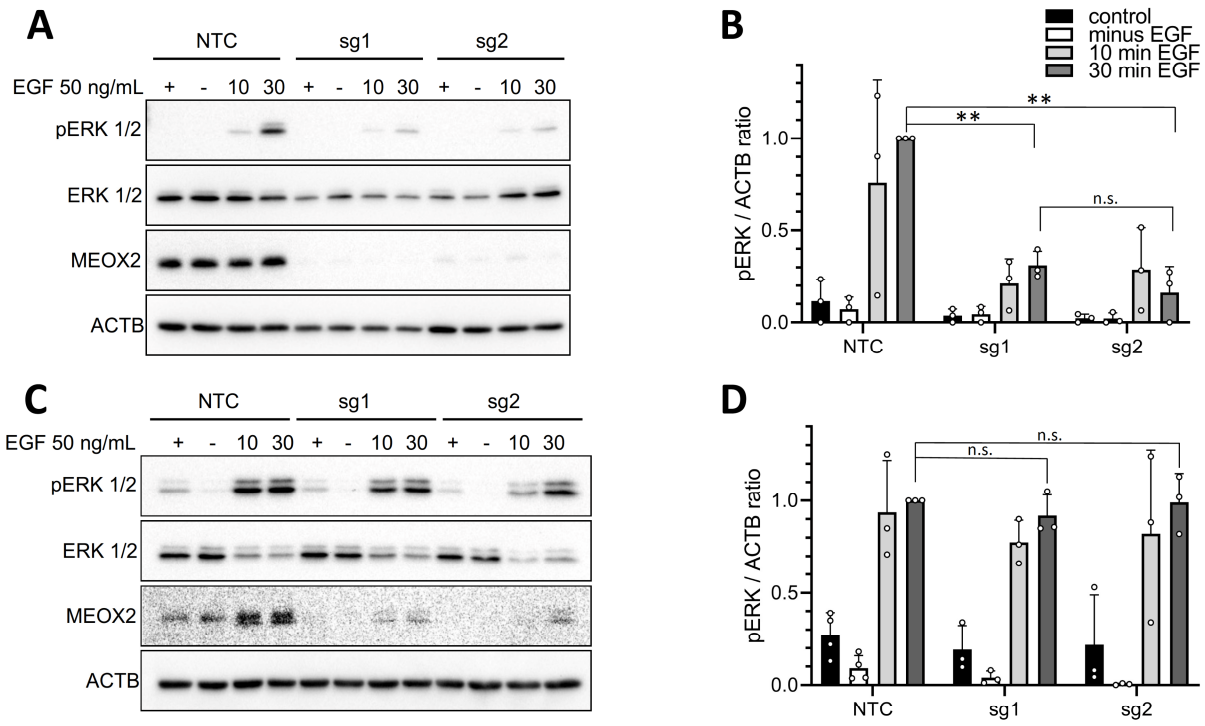

Figure 17: Phosphorylation of ERK induced by MEOX2 in TS667 patient derived tumorsphere cell line.
A–D: Cells were either kept under normal conditions (+) or starved off EGF / FGF for 48 h (-, 10, 30) followed by EGF treatment for 10 min or 30 min (10, 30) for pathway activation. A) pERK expression in TS667 cell line control (NTC) and sg1, sg2 (CRISPR/Cas9 modified to lose MEOX2 expression). B) Quantification of pERK to ACTB expression in TS667 cell line control (NTC) and sg1, sg2 (CRISPR/Cas9 modified to lose MEOX2 expression). Control (+) = black, starved (-) = white, 10 min treatment (10) = light grey, 30 min treatment (30) = dark grey; n = 3, mean ± SD, Two-sided Welsh's test. C) pERK expression in TS600 cell line control (NTC) and sg1, sg2 (CRISPR/Cas9 modified to lose MEOX2 expression). D) Quantification of pERK to ACTB expression in TS600 cell line control (NTC) and sg1, sg2 (CRISPR/Cas9 modified to lose MEOX2 expression). Control (+) = black, starved (-) = white, 10 min treatment (10) = light grey, 30 min treatment (30) = dark grey; n = 3, mean + SD. Two-sided Welsh's test.

4.9 *In vitro* growth and drug treatments of GBM cell lines

To understand the reason for the difference in ERK activation between both used cell lines (TS667, TS600), I investigated drug sensitivity of both cell lines (TS667, TS600) to learn if there is generally a different sensitivity towards drug treatment between them, and within each line and the established CRISPR/Cas9 single guide KD cell lines. Therefore, I facilitated an MTT assay setup. Interestingly, over all tested cell lines, cells did not show an altered metabolism after Galunisertib treatment, a TGFB inhibitor. Even though TGFB is one of the top predicted upstream regulators from RNA-seq analysis (Figure 10). After Erlotinib (EGFR inhibitor) treatments there was a similar inhibition of metabolism observed in TS600 and in TS667 cells. The TS667 cell line is shown here to be generally more sensitive towards AC710, a PDGFR inhibitor, than the TS600 cell line. TS667 cell line also showed a delayed inhibition after Trametinib, a MEK inhibitor, treatment. A reduction in metabolism similar to the reduction achieved in TS600 after 24 h already (Figure 23 G, ~30 % reduction), was observed in TS667 only after 48 h of treatment (Figure 23D). However no significant changes were observed within each cell line when comparing inhibitory effects on metabolism of endogenously MEOX2 expressing GBM cell lines (TS667-NTC, TS600-NTC) to *MEOX2* KD cells (TS667-sg1, TS667-sg2, TS600-sg1, TS600-sg2). Only trends could be observed (Figure 23C, D, G, H). Additionally, no difference in in vitro growth was observed between control and MEOX2-KD in TS667 or TS600 (Figure 23B, F).

5 Discussion

GBM exhibits an invasive and fast-growing phenotype. Due to this characteristic, GBMs are hard to treat and cannot be completely removed using surgical measures. Overall survival averages at 15 months. Despite intense research in the field, no therapy for GBM has yet been identified that increases survival. Only limited extension of survival time can be obtained by surgery, radiotherapy or chemotherapy (Stupp et al., 2005). New attempts to therapy follow a targeted approach, where deregulated activity of genes is directly targeted using antibody or inhibitor treatments. An obstacle with targeted therapies, is the adaptive capability of tumor cells and tissue. Once a pathway gets blocked, the tumor usually compensates for it by upregulation of different pathways.

5.1 *MEOX2* – a potential oncogene in gliomas

MEOX2 is a transcription factor that is activated during embryonic development and is not expressed in the adult brain. Recently, it was shown that *MEOX2* expression directly correlates with tumor grade in gliomas. A role for *MEOX2* in gliomas has not been described before. Interestingly, *MEOX2* expression is highly upregulated in GBM, and shows low or no expression in LGG. As LGG has a better prognosis than GBM, it is of interest to understand the potential role of *MEOX2* as an oncogene and a contributor to malignant transformation of tumor cells in gliomas.

5.2 *MEOX2* induces an oncogenic phenotype *in vivo* and *in vitro*

In this study we identified *MEOX2* as a potential oncogene in gliomas. We orthotopically implanted patient derived GBM cell lines with high *MEOX2* expression levels (TS00, TS667), representative of the average *MEOX2* expression in GBM in immunocompromised mice. No difference in cell proliferation was observed *in vivo* after knockdown of *MEOX2* in these models. Both cell lines proliferated rapidly *in vivo* leading to early tumor-burden symptoms. However, *MEOX2* overexpression in a GBM cell line with slower *in vivo* growth kinetics, led to a significant increase of cell proliferation compared to the control. The MEOX2-induced growth phenotype was statistically significant 8 weeks after implantation (080125, Figure 6B). Implanted cell lines varied significantly in baseline growth kinetics, increased cell proliferation with MEOX2 overexpression was only observed in the slower growing line (Figure 6B, E). Taken together, these results suggest a role of *MEOX2* in inducing cell proliferation *in vivo*. As cell proliferation was not reduced by *MEOX2* knockdown in fast growing GBM lines with high endogenous *MEOX2* levels, we assume that once a rapid growth phenotype is established in

gliomas, it cannot be reversed by *MEOX2* depletion. These results indicate an initiation of permanent deregulatory effects by *MEOX2*.

To support our hypothesis, we performed experiments on cerebral orgenoids (CO) to further investigate the role of *MEOX2* in early glioma development. Therefore, we collaborated with the Mall lab at DKFZ, where Elisa Heinzelmann performed CO experiments. We were successful to identify *MEOX2* as a key driver of cell proliferation in an CO cancer model. Cell proliferation was significantly increased after *MEOX2* OE in the tumor model with simultaneous *p53* and *PTEN* KO (Figure 7A, B). *P53* and *PTEN* both act as tumor suppressor genes and are frequently mutated or downregulated in cancer cells (Table 20), increasing cell proliferation and survival. The increase in cell proliferation observed in the organoid experiment following *MEOX2* OE with simultaneous *p53* and *PTEN* KO was significantly higher than cell proliferation induced by individual *MEOX2* OE or *p53*, *PTEN* double-KO (Figure 7A, B). This result highlights not only *MEOX2* effect on general cell proliferation but also how this effect is amplified in a background of already deregulated tumor suppressor genes like *p53* and *PTEN*.

It is not reported how MEOX2 and p53, PTEN interact. A shared downstream target of *MEOX2* and *p53* are p21 and p16 CDK inhibitors, that regulate cell cycle arrest and induce cell senescence (Terzi et al., 2016). *MEOX2* OE leads to increased p21 and p16 expression (Douville et al., 2011). *P53* has a similar regulatory effect on p21. It upregulates expression to inhibit cell cycle for DNA damage repair, preventing genome instability (J. Chen et al., 2006; Mijit, Caracciolo, Melillo, Amicarelli, & Giordano, 2020; Sharpless & Sherr, 2015). It is not reported why *MEOX2* OE, upregulating p21 and p16, could increase tumorigenic potential in *p53* and *PTEN* double-KO cell lines. A possible hypothesis could be the adoption of EMT by cancer cells, where upregulation of senescence markers like p21 and p16 can lead to a mesenchymal cell phenotype (Hu, Wu, Chang, Cheng, & Wu, 2008; Vega et al., 2004). Mesenchymal cells show more infiltrative potential, which is a characteristic observed in GBM. From our data we observed a more elongated shape of cells, when comparing the organoids' morphology after *MEOX2* OE + *PTEN*, *p53* KO versus *MEOX2* OE alone (Figure 7C), which hints to a potential role for both genes in EMT. Also, *p53* loss can lead to decreased expression of p53-miR-200c pathway in mammary epithelial cells, by activating the EMT programme. It was reported how EMT-associated cancer stem cells can potentially be suppressed through *p53*

KO (Chang et al., 2011). *MEOX2* OE might further increase the EMT phenotype in a *p53* KO, tumor environment.

5.3 MEOX2 protein localization depends on S155 phosphorylation

We identified a novel phosphorylation site in MEOX2 after performing mass spectrometry analysis on MEOX2 IP in patient derived GBM cell line TS667 and MEOX2 OE in HEK293TN cells. MEOX2 showed a phosphorylation of serine at position 155 which is located before the functional DNA-binding homeobox-domain (Table 21). The SP motif was identified in this position and predicts a phosphorylation of serine via ERK. ERK is a kinase downstream of MEK, in the RAS/RAF/MAPK pathway. This pathway is regularly found altered in cancer, leading to increased proliferation and cell survival of tumor cells (Figure 3, (Santarpia, Lippman, & El-Naggar, 2012)). Inhibition of S155 phosphorylation by serine to alanine mutation (S155A) changed localization of MEOX2 in HEK293TN cells (Figure 8E). Wild-type MEOX2 protein is expressed in the nucleus, where it binds to chromatin to regulate transcription of genes. With the S155A mutation, the localisation of MEOX2 protein was shifted from an even distribution in the whole nucleus, to the nuclear envelope (rim) with a measured increase of 15,9 % (Figure 8E, F). A functional phosphorylation of MEOX2 has not been reported in GBM cells before. Phosphorylation of transcription factors however is known to alter transcriptional activity of DNA binding targets. As an example, increase- or decrease of transcription factor activity of p53 is observed depending on phosphorylated sites. ERK2 has been reported to phosphorylate p53 in Thr55, activating p53's effect on apoptosis signaling (Yeh et al., 2004).

We identified that protein stability of MEOX2 is not affected by S155A mutation (Figure 8B, C). However, we observed decreased p21 expression, a downstream target of MEOX2, after MEOX2-S155A OE in HEK293TN cells versus wt MEOX2 (Figure 8D). Hence lack of phosphorylation does not affect MEOX2 protein stability, the shift in protein localization could potentially be the source of transcriptional deregulation of MEOX2 downstream targets. This might be due to reduced chromatin accessibility at the nuclear envelope location or due to lack of direct activation of MEOX2 by serine phosphorylation. We hypothesize that MEOX2 is phosphorylated at serine 155 by ERK, leading to even protein localization, and increased transcription factor activity resulting in activation/repression of downstream targets.

Interestingly, we were also able to show that phosphorylation of ERK depends on MEOX2 expression in HEK293, HEK293TN and one GBM cell line (TS667). In HEK and HEK293TN cells, we observed significant increase in ERK phosphorylation upon MEOX2 OE, which was completely reversed with MEK inhibition (Figure 16A, B; Figure 22A, B). Additionally, we observed less phosphorylation of ERK upon MEOX2 S155A overexpression versus MEOX2 wt (Figure 16A, B). In both cases, ERK phosphorylation was inhibited by MEK inhibitor, pointing to a direct phosphorylation of ERK via MEK in a MEOX2 dependent manner. MEOX2 downstream target p21 expression was also reduced by MEK inhibitor use, whereas MEOX2 levels did not change (Figure 16A, C; Figure 22A, C). This points to a pERK dependent p21 activation. If MEOX2 is phosphorylated at S155 by ERK, increasing transcriptional activity of MEOX2 without affecting protein stability, and MEOX2 activates ERK phosphorylation via MEK, these results taken together could implicate p21 transcription relies on MEOX2 expression and activity, induced by phosphorylation of MEOX2 via ERK. Our hypothesis is that MEOX2 may be activated by S155 phosphorylation via ERK, resulting in a feedback loop of increased ERK phosphorylation via MEK, in HEK293 and HEK293 TN cells. In this hypothesis it is not determined whether MEOX2 is phosphorylated directly via ERK or by an additional kinase. In TS667 cells, we initiated the MAPK pathway by starvation of cells for 48 h of EFG and FGF followed by initiation of pathway signaling using high dose of EGF (50 ng/mL). We observed a fast increase in ERK phosphorylation after 10 min of cell incubation. Interestingly, this response of increased ERK phosphorylation was lost after MEOX2 KD using either sg1 or sg2 MEOX2 KD (Figure 17A, B). In TS600 cell line we did not observe this effect (Figure 17C, D), however the baseline level of phosphorylated ERK, indicating activated MAPK pathway, was higher than in TS667, where we observed a response to pathway initiation (Figure 17A, C). GBM cell lines show high heterogeneity, and differences in gene amplifications. TS667 cell line is PDGFR amplified whereas TS600 cell line is EGFR amplified. It is possible that ERK phosphorylation via MEOX2 is not activated in TS600 by external pathway initiation due to these molecular differences.

5.4 Transcriptional changes induced by *MEOX2* expression

Facilitating newest sequencing techniques, we identified pathways and individual genes deregulated by *MEOX2*. Our results were generated using patient derived GBM cell lines either overexpressing *MEOX2* in case of low endogenous expression or knocking down *MEOX2* in case of high endogenous expression, to gain a comprehensive understanding of *MEOX2*'s role as a transcription factor. Additionally, we analysed MEOX2's DNA binding targets *in vitro*,

using GBM cells and ACT-seq technique, and *in vivo*, using a patient sample and CUT&Tag technique. Our RNA-seq results highlight multiple cancer related pathways to be downregulated upon *MEOX2* KD. We identified correlation between *MEOX2* expression and hepatic fibrosis pathway activation in all four sequenced cell lines, indicating a regulatory effect of *MEOX2* on hepatic fibrosis pathway (Figure 9A, Figure 11). Hepatic fibrosis marks a chronic inflammation of tissue, inducing excessive scar matrix as a wound-healing response. This leads to an imbalance between production and resorption of ECM (Kocabayoglu & Friedman, 2013). In cancer cells, fibrosis regulation hints to a role of *MEOX2* in ECM regulation. Increased ECM expression enables an easy escape from the cell structure for tumor cells, promoting migration of cells and a more infiltrative tumor phenotype (Eble & Niland, 2019). Therefore, we hypothesize that *MEOX2* plays a role in ECM regulation in gliomas, inducing a more infiltrative phenotype in GBM. In line with our hypothesis, we identified TGFβ1 as a top upstream regulator in our experiments (Figure 10). TGFβ1 signaling can affect the tumor microenvironment, and is reported to induce fibrosis and EMC remodeling, promoting metastasis in cancer (Caja et al., 2018; Drabsch & ten Dijke, 2012). Interestingly, we also identified the local sequester of TGF-β, latent-transforming growth factor beta-binding protein 1 (LTBP1), as a direct DNA binding target of MEOX2. From our data we also identified LTBP1 transcription to correlated with *MEOX2* expression (4.7.2), indicating a potential direct regulation of LTBP1 by MEOX2. LTBP are multidomain glycoproteins which consist of tandem arrays of epidermal growth factor–like domains, that are calcium-binding. LTBP1 forms a complex with TGF-β (and LAP), large latent complex (LLC), which localizes to the ECM, where TGF-β gets activated (Robertson & Rifkin, 2016). In normal epithelial cells, TGFβ acts as a tumor suppressor antagonizing mitogenic RAS signaling, but TGF-β and RAS can act collaboratively in driving tumor progression (Matsuzaki, 2011). Additionally, an important mechanism for non-Smad TGF-β signaling is described by regulation of MAPK signaling by TGF-β (Derynck & Zhang, 2003).

Mammalian TOR (mTOR) is a large protein kinase which exists in two distinct complexes: one contains mTOR, mLST8 and RPTOR (mTOR Complex1) and the other contains mTOR, MAPKAP1, mLST8 and RPTOR Independent Companion Of mTOR Complex2 (RICTOR; mTOR Complex2). The RPTOR-containing complex, mTOR Complex1, is sensitive to the drug rapamycin and regulates cell growth and proliferation. The RICTOR-containing complex, mTOR Complex2, is not rapamycin-sensitive (H. Hua et al., 2019). RICTOR has been shown to activate AKT/protein kinase B (PKB) via phosphorylation on Ser473. AKT/PKB has been

implicated in cancer and its cellular function. Additionally, an essential role in embryonic growth and development were identified (actin cytoskeleton organization) (Sarbassov, Guertin, Ali, & Sabatini, 2005). We identified RICTOR as a positively correlating upstream regulator upon *MEOX2* OE in two GBM cell lines (Figure 12). AKT/protein kinase B (PKB) pathway, which is implicated in cancer pathogenesis and activated by RICTOR, is also opposed by PTEN tumor suppressor gene. Hence mTORC2 is a potential drug target in tumors that have lost the expression of PTEN. Finally, RICTOR downstream targets' transcription levels exhibit inverse correlation with MEOX2 expression levels after *MEOX2* OE but not after *MEOX2* KD in GBM cell lines. This leads us to the hypothesis, that the regulatory potential *MEOX2* potentially has on mTORC2 (RICTOR) is activated upon *MEOX2* OE but not retracted after *MEOX2* KD, once initiated. Interestingly, we did not identify *RICTOR* transcription upregulated in our data, however significant downregulation of multiple downstream targets.

Our experiments provide only limited direct links between DNA binding and transcriptional regulation via MEOX2. We assume that regulation via MEOX2 is a sensitive system that will provide different regulatory effects *in vitro* versus *in vivo* studies, as cultured cells do not possess the full tumor microenvironment. Especially as we identify a potential role of MEOX2 in ECM and EMT regulation, supporting a more infiltrative cell phenotype in gliomas, the *in vivo* microenvironment of glioma cells cannot be neglected. For our experiments, we cultured GBM cell lines as spheroids, which provides no attachment possibility for the cells except from bulk formation. Using our experimental approach, we gained valuable and novel insights into the genes potentially regulated by MEOX2. Hence, we can provide a clear correlation between MEOX2 binding and transcriptional activation, indicating a direct regulation via MEOX2 for a set of genes. These genes are potential targets for further glioma research.

One newly identified MEOX2 target of interest is Neuronal Cell adhesion molecule (NRCAM), which was identified as a direct DNA binding target to MEOX2 in our *in vitro* and *in vivo* binding studies (4.7.4). NRCAM transcription levels were also found correlating in both our experimental setups of *MEOX2* KD or *MEOX2* OE, with *MEOX2* expression (4.6.3). NRCAM is a member of the immunoglobulin superfamily, and highest expression levels are found in the CNS (Grumet, 1997). NRCAM has a role in neuronal outgrowth and guidance (Sakurai, 2012). Overexpression of NRCAM has previously been reported in cancer, but not in glioma. For example, it was described as a potential predictor of worse recurrence-free survival in prostate cancer (Ling et al., 2019) and a marker of poor prognosis for advanced colorectal cancer patients

(Chan, Ong, & Salto-Tellez, 2011). NRCAM overexpression in fibroblasts induced cell motility and tumorigenesis. In addition to homophilic cell-cell adhesion, NRCAM can mediate heterophilic adhesion with ECM receptors. NRCAM was also shown to prevent cell apoptosis by activation of MAPK/ERK and PI3K/AKT pathways. Activation of both pathways is initiated via NRCAM ectodomain shedding and EGFR binding as well as binding to α4β1 integrins (Conacci-Sorrell et al., 2005; Zhang et al., 2017). A positive feedback loop has been identified in thyroid cancer cells where these MAPK/ERK and PI3K/AKT pathways activated NRCAM overexpression through GSK3β/β-catenin pathway signaling axis, which is a serine threonine kinase (Zhang et al., 2017).

EGFR transcription was downregulated with MEOX2 KD (TS600 sg1, sg2). Additionally, EGFR was predicted to be an upstream regulator inhibited with MEOX2 KD, in the same cell line (4.6.1.2). Additionally, we identified EGFR and EGFR-AS1 (EGFR Antisense RNA 1) as direct binding targets of MEOX2 in an EGFR amplified GBM cell line *in vitro* (TS600) and *in vivo* (both times within non-promoter regions, 4.7.4). EGFR-AS1 is an RNA gene, meaning it is not translated into protein. In renal and bladder cancer EGFR-AS1 was reported to inhibit EGFR mRNA degradation by directly binding, and stabilizing, EGFR mRNA. In conclusion, EGFR-AS1 promoted expression of EGFR *in vitro* and *in vivo* (A. Wang et al., 2019; A. Wang et al., 2020). The EGFR signaling pathway is well characterized and reported to increase cell proliferation and invasion in cancer (Sigismund, Avanzato, & Lanzetti, 2018). EGFR is the most upstream target of AKT and RAS pathways (Figure 3). In gliomas, and specifically GBM, EGFR is one of the most altered genes (Table 20). Amplification of EGFR and increased pathway activation results in poor prognosis for glioma patients (Saadeh, Mahfouz, & Assi, 2018). Because of these characteristics, EGFR was an attractive target in targeted therapy research, however the biological complexity provided prevented the find of a favorable drug candidate (Westphal, Maire, & Lamszus, 2017). Previous research in gliomas identified EGFR-AS1 knockdown to suppress cell proliferation, migration, and invasion of cells, suggesting a direct role in cancer associated pathway activation of EGFR-AS1 via miR-133b/RACK1 regulation (Dong, Guo, & Xie, 2019). We identified MEOX2 as a direct binding partner, and a potential transcriptional regulator of EGFR and EGFR-AS1. Our results suggest MEOX2 might amplify cell proliferation via EGFR signaling in gliomas.

In this work we identified multiple levels of correlation between MEOX2 with tumor protein p53. P53 is a well characterized oncogene. It has multiple functional roles. It acts as a direct

transcriptional activator, resulting in tumor suppressing pathway regulations (Sullivan et al., 2018). Loss or mutation of p53 tumor suppressor function is a common driver of cancer. P53 mutation is more common in secondary GBM than in primary GBM, highlighting the accumulation of additional genetic alterations in malignant transformation of cancer (Table 20). Functional correlations between MEOX2 and p53 have not been described in gliomas before. Our analysis of RNA-seq data identified p53 as an inhibited upstream regulator of transcriptionally downregulated targets with MEOX2 KD (Figure 9D, TS667-sg1, -sg2, TS600-sg1). Additionally, pathway analysis of our ACT-seq data indicated p53 the top deregulated pathway after MEOX2 KD, by significant downregulation of p53-related DNA target binding, such as NDRG1 with MEOX2 loss (Figure 14A). These results indicate direct binding and transcriptional correlations between p53 pathway targets and MEOX2.

For our organoid experiments, p53 KO was used to simulate a tumor environment to elucidate the role of *MEOX2* upregulation in CO. Interestingly, in this setting we identified MEOX2 OE or PTEN/p53 KO both induced a comparable significant increase of cell proliferation. However, we observed a significant increase between individual MEOX2 OE or PTEN/p53 KO and a condition of concomitant MEOX2 + PTEN/p53 KO. The latter increased cell proliferation comparably to a Nf1/PTEN/p53 KO model (Figure 7A, B). PTEN is a known tumor supressor often times downregulated or non-functional in cancers (Worby & Dixon, 2014) (Table 20). In our cerebral organoid experiments PTEN was identified as a key driver gene that lead to significant increase in cell proliferation upon double KD with p53 and parallel MEOX2 OE (Figure 7A, B). PTEN signaling pathway was identified top downregulated pathway upon MEOX2 OE in GBM cell lines (Figure 11, 080125, 080512). With these results, we hypothesize the oncogenic role of MEOX2 benefits, and potentially to a certain extent regulates, downregulation of tumor suppressor pathways to advance tumorigenesis in gliomas. A collective mode of action between loss of tumor suppressors and MEOX2 OE could explain the correlation of *MEOX2* expression with tumor grade (Figure 4), and supports hypotheses claimed in this work, for MEOX2 as a player in malignant transformation from LGG to GBM in gliomas. The direct mode of action is not identified and might include several indirect/additional players.

6 Outlook

With this work, we identify MEOX2 as a novel potential oncogene in glioma that might be involved in the malignant transformation of tumor cells. We highlight MEOX2 as a regulator of gliomagenesis. Newly identified MEOX2 targets decribed in this work provide new insights and starting points for ongoing glioma research. The characterization of MEOX2 as a potential regulator of ECM formation and EMT of cells will hopefully lead to fruitful research for glioma therapy, to potentially keep glioma in a lower grade, and less infiltrative state, that can be treated as a chronic disease.

7 Appendix

7.1 Supplemental figures and tables

Table 22: *MEOX2* gene expression in normal human brain.
Data aquired from GTEx portal.

Tissue (human)	**pTPM**
Cerebral cortex	0,4
Cerebellum	0,2
Hippocampal formation	0,1
Amygdala	0,3
Basal ganglia	0,3
Hypothalamus	0,5
Midbrain	0,3
Spinal cord	0,5

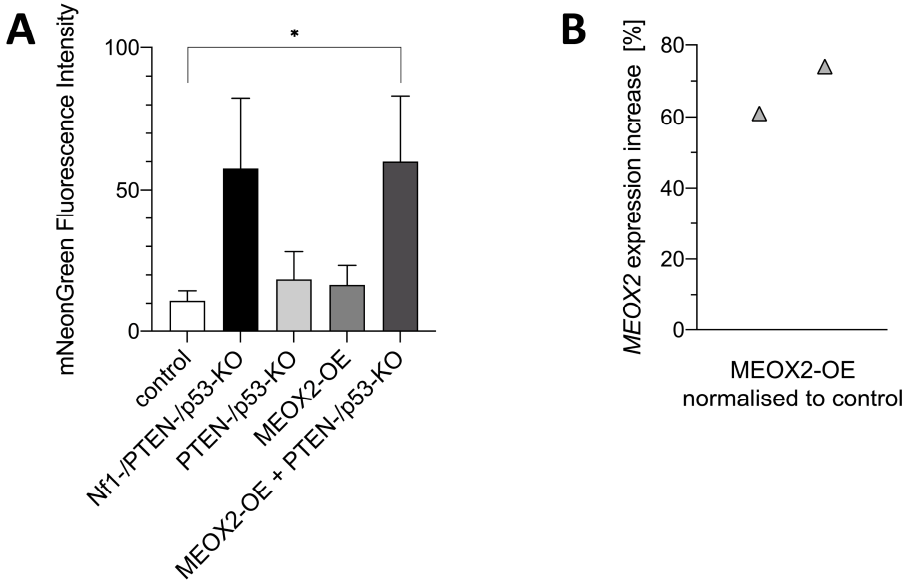

Figure 18: Validation of *MEOX2* OE in cerebral organoids (CO).
A) mNeonGreen intensity measurement of CO after one month of culture post nucleofection using KO and/or MEOX2-OE plasmids. Samples shown from left to right: Control (n = 24), Nf1-/PTEN-/p53-KO (n = 23); PTEN-/p53-KO (n = 15); MEOX2-OE (n = 10), MEOX2-OE + PTEN-/p53-KO (n = 16); (mean ± SEM, unpaired T-test). B) qPCR validating *MEOX2* expression in organoids 28 days after nucleofection using MEOX2-OE plasmid nucleofected CO (n = 2) normalised to *MEOX2* expression in control nucleofected CO (n = 2), qPCR results were first normalised to 18s.

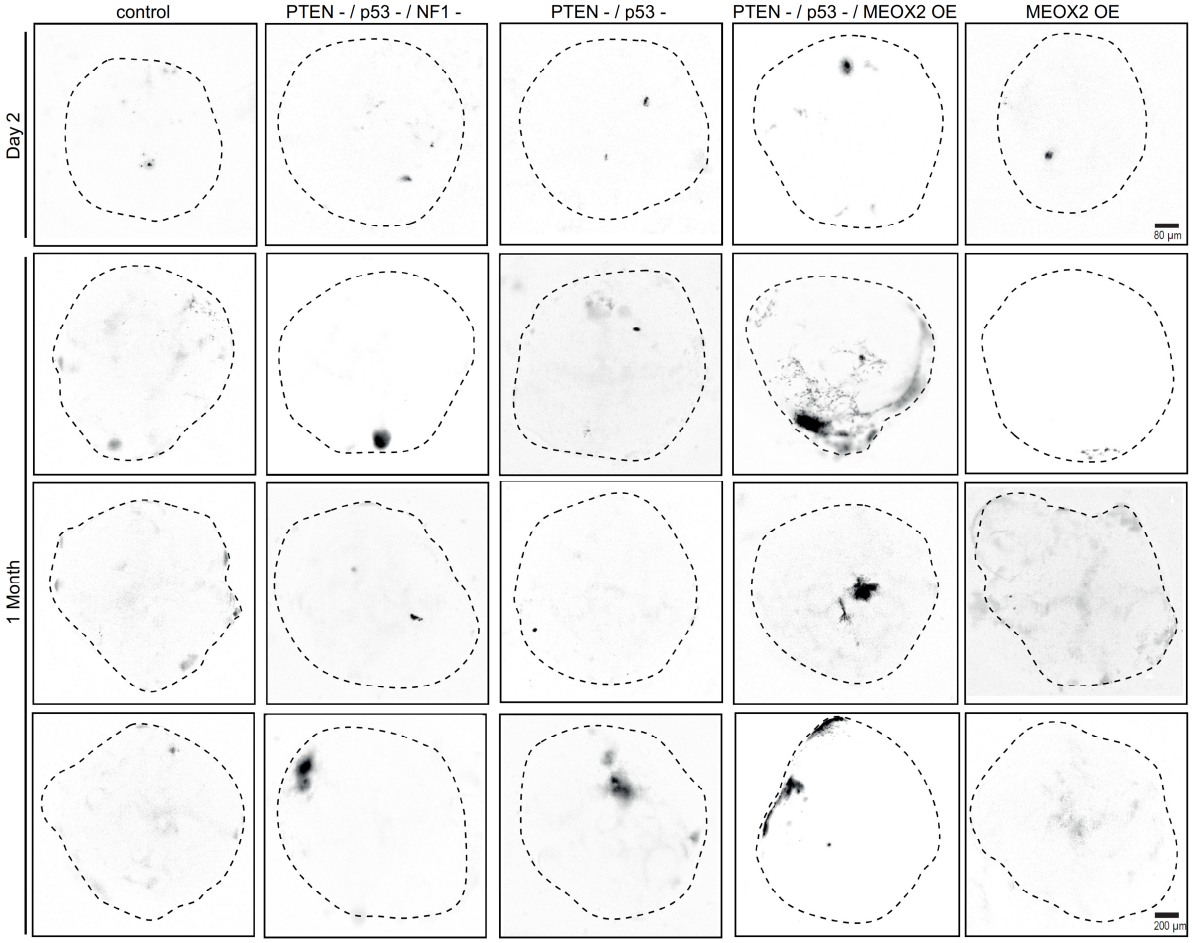

Figure 19: Images of organoids.
Images taken by Elisa Heinzelmann. Black colour indicating growth initiated after nucleofection using KD and/or MEOX2 OE plasmids. Samples shown from left to right: control; Nf1 loss + PTEN loss + p53 loss; PTEN loss + p53 loss; MEOX2 OE + PTEN loss + p53 loss; MEOX2 OE. Growth measured via mNeonGreen signal after one day (top row) and one month (row two, three, four).

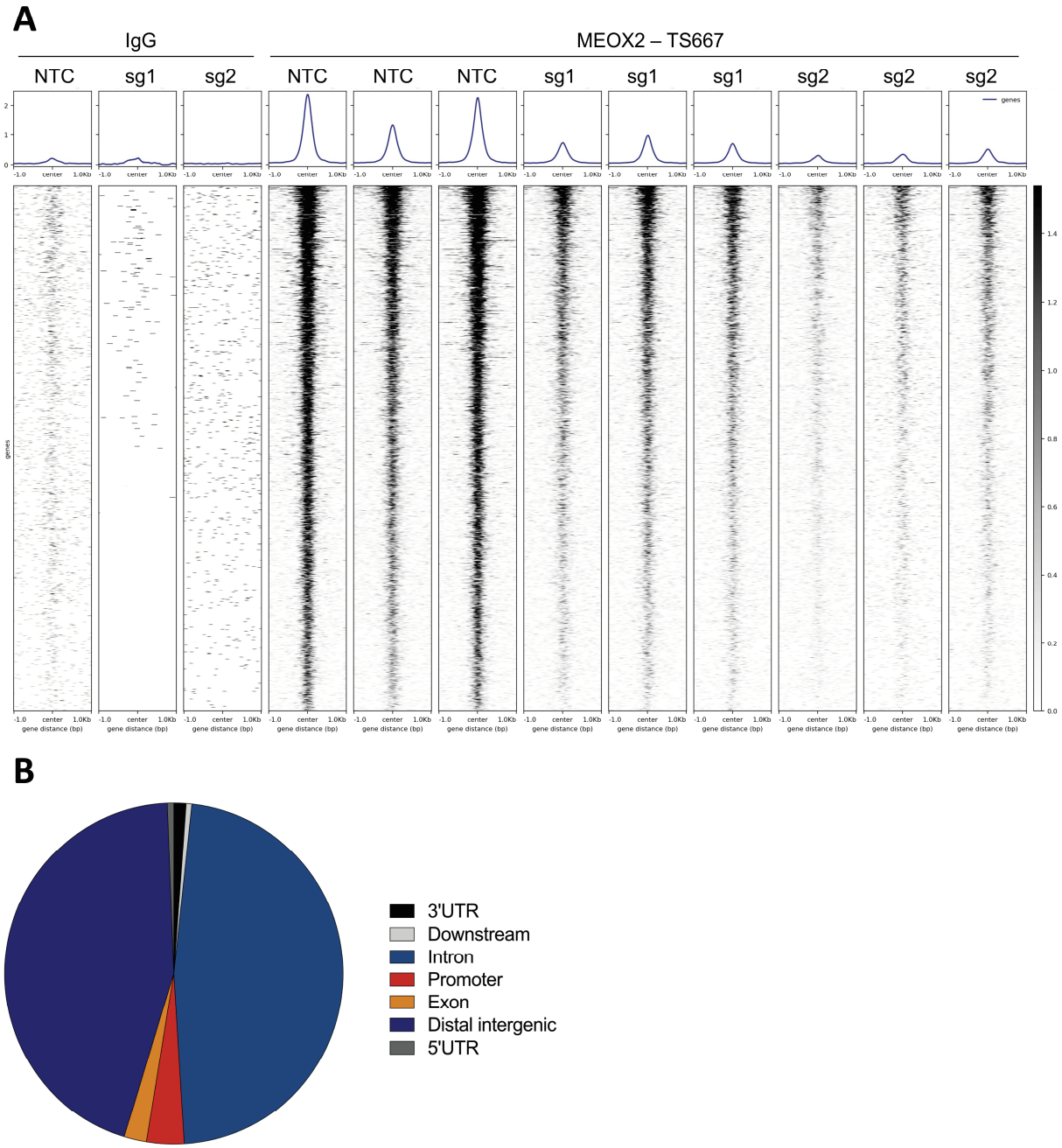

Figure 20: MEOX2 binding targets identified using ACT seq in TS667 patient derived tumorsphere cell line.
A) IgG controls (lane 1–3) and MEOX2 binding reads in TS667 NTC control GBM cell line (lane 4–6) versus two individual CRISPR/Cas9 sg KD lines (lane 7–9, lane 10–12). B) Binding of MEOX2 analysed by DNA region in NTC over sg2 KD. 3'UTR: 1,2 %, Downstream: <1 %, Intron: 47 %, Promoter: 3,6 %, Exon: 2 %, Distal intergenic: 45 %, 5'UTR: <1 %. UTR = untranslated region.

A

TS600

Rank	Target	PWM	Motif ID	Raw score	P-value	In top motifs
7	MAX		M1889_1.02	1.14	0	32 %
7	BATF::JUN		BATF::JUN	12.2	0	44 %
7	FOS		FOS	17.5	0	48 %
7	FOSL1		FOSL1	21.1	0	48 %
7	FOSL2		FOSL2	19.9	0	47 %
7	JUN (var.2)		JUN (var.2)	22.6	0	47 %
7	JUNB		JUNB	19.5	0	47 %
7	JUND		JUND	19.9	0	51 %
7	AP1		AP1	4.06	0	48 %
7	JDP2		Hsapiens-jolma2013-JDP2	15.4	0	41 %

B

TS667

Rank	Target	PWM	Motif ID	Raw score	P-value	In top motifs
1	NKX6-1		Hsapiens-jolma2013-NKX6-1	2.2	1.66e-205	12 %
2	BATF::JUN		BATF::JUN	2.8	8.12e-157	19 %
3	MAX		M1889_1.02	1.13	6.85e-146	19 %
4	MEOX1		Hsapiens-jolma2013-MEOX1	1.95	2.31e-143	15 %
5	MEOX2		Hsapiens-jolma2013-MEOX2	1.93	5.77e-139	15 %
6	LHX4		LHX4	1.99	1.66e-135	12 %
7	PDX1		Hsapiens-jolma2013-PDX1-2	2.06	1.82e-131	8 %
8	HOXA2		Hsapiens-jolma2013-HOXA2	1.68	9.71e-126	16 %
9	FOXA1		FOXA1	3.45	2.45e-125	15 %
10	HOXA1		Hsapiens-jolma2013-HOXA1	1.82	4e-125	12 %

C

Rank	Target	PWM	Cell line	Motif ID	Raw score	P-value	In top motifs
781	MEOX2		TS600	Hsapiens-jolma2013-MEOX2	1.03	6.44e-09	4 %
5	MEOX2		TS667	Hsapiens-jolma2013-MEOX2	1.93	5.77e-139	15 %

Figure 21: Binding motifs identified from ACT-seq experiments.
A) Most frequent MEOX2 binding motifs identified in TS600 cell line. B) Most frequent MEOX2 binding motifs identified in TS667 cell line. C) MEOX2 binding motife identified from TS600 and TS667 ACT-seq data.

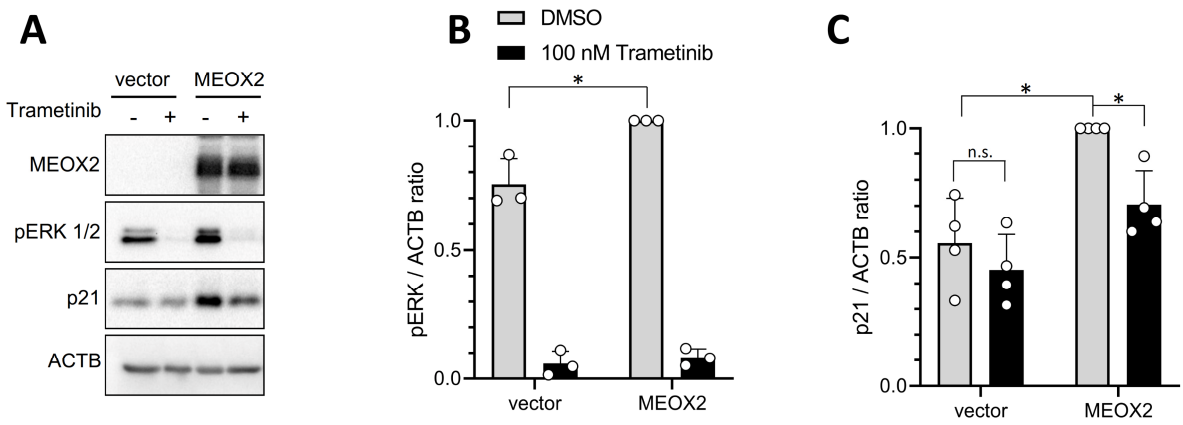

Figure 22: Phosphorylation of ERK induced by MEOX2 in HEK293 cells.
A) Western Blot of MEOX2 (right), and control (left) transfected HEK293 cells. 48 h after transient transfection and 24 h after trametinib treatment (+, 100 nM) or DMSO treatment for control (-). B) Quantification of pERK to ACTIN expression (n = 3, mean + SD, Two-sided Welsh's test). C) Quantification of p21 to ACTIN expression (n = 4, mean + SD, Two-sided Welsh's test).

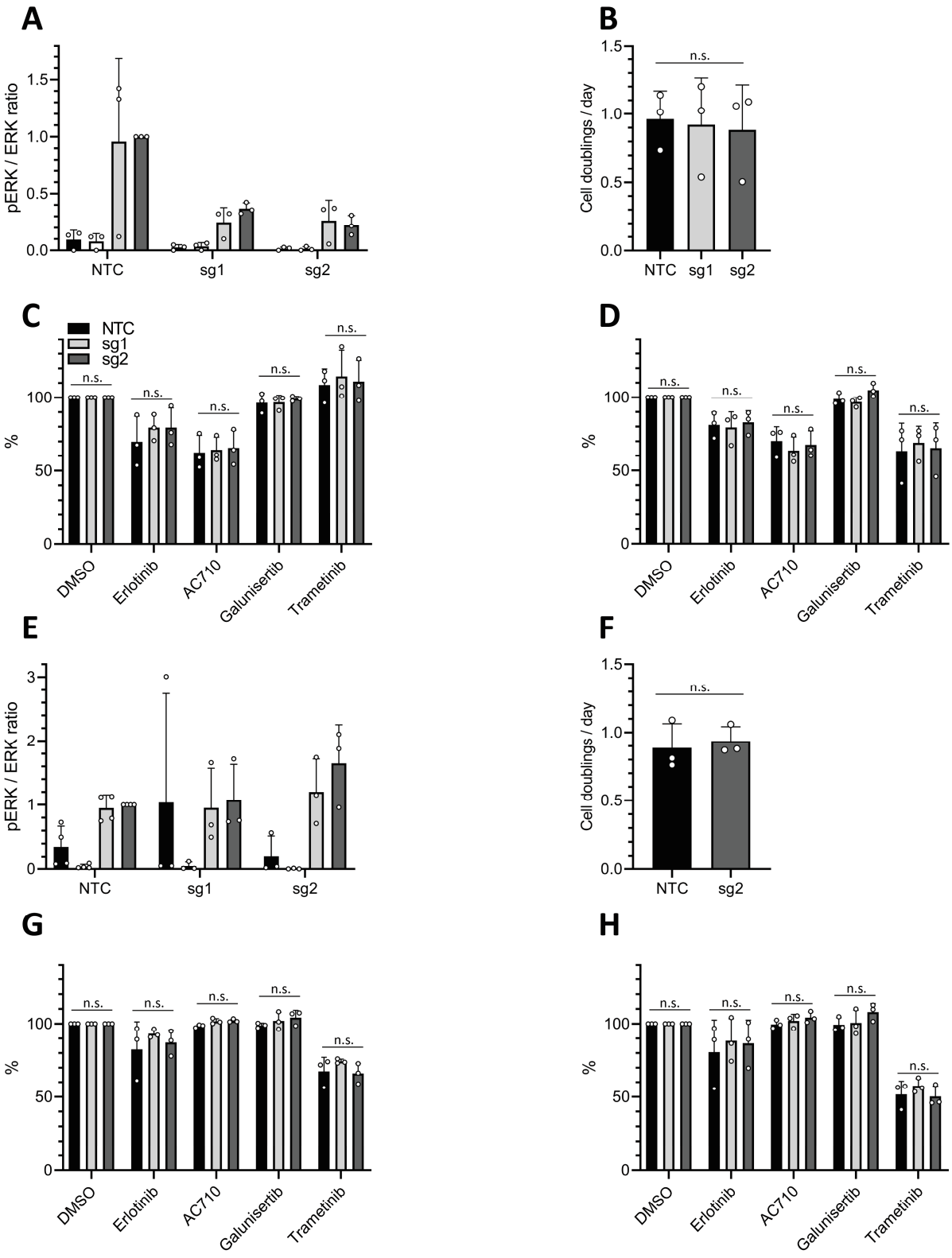

Figure 23: Growth and drug resistance in TS667 and TS600 patient derived tumorsphere cell lines.
A–D: TS667, E–H: TS600. A) Quantification of pERK to ERK expression in TS667 cell line control (NTC) and sg1 *MEOX2* KD, sg2 *MEOX2* KD. Cells were either kept under normal conditions (control) or starved off EGF / FGF for 48 h (minus EGF, 10 min EGF, 30 min EGF) followed by EGF treatment for 10 min or 30 min (10 min EGF, 30 min EGF) for pathway activation. Control = black, starved (minus EGF) = white, 10 min treatment (10 min EGF) = light grey, 30 min treatment (30 min EGF) = dark grey; n = 3, mean + SD, Two-sided Welsh's test). B) Growth of TS667 cell line *in vitro* observed by cell doublings per day in control (NTC) and sg1 *MEOX2* KD, sg2 *MEOX2* KD modified TS667 cells (n = 3, mean + SD, Two-sided Welsh's test). C + D) Drug resistance measured by MTT assay on TS667 cell line control (NTC = black) and sg1 *MEOX2* KD (light grey), sg2 *MEOX2* KD (dark grey). Drug treatments using DMSO (control), Erlotinib (10 µM), AC710 (150 nM), Galunisertib (10 µM) or Trametinib (100 nM). C) Measurements after 24 h of drug treatment. D) Measurements after 48 h of drug treatment.

E) Quantification of pERK to ERK expression in TS600 cell line control (NTC) and sg1 *MEOX2* KD, sg2 *MEOX2* KD. Cells were either kept under normal conditions (control) or starved off EGF / FGF for 48 h (minus EGF, 10 min EGF, 30 min EGF) followed by EGF treatment for 10 min or 30 min (10 min EGF, 30 min EGF) for pathway activation. Control = black, starved (minus EGF) = white, 10 min treatment (10 min EGF) = light grey, 30 min treatment (30 min EGF) = dark grey; n = 3, mean + SD, Two-sided Welsh's test). F) Growth of TS600 cell line *in vitro* observed by cell doublings per day in control (NTC) and sg1 *MEOX2* KD, sg2 *MEOX2* KD modified TS600 cells (n = 3, mean + SD, Two-sided Welsh's test). G + H) Drug resistance measured by MTT assay on TS600 cell line control (NTC = black) and sg1 *MEOX2* KD (light grey), sg2 *MEOX2* KD (dark grey). Drug treatments using DMSO (control), Erlotinib (10 µM), AC710 (150 nM), Galunisertib (10 µM) or Trametinib (100 nM). G) Measurements after 24 h of drug treatment. H) Measurements after 48 h of drug treatment.

Table 23: RNA-seq of *MEOX2* OE in IHA versus control.

Symbol	Expression Log Ratio	Expression p-value	Expression False Discovery Rate (q-value)	Expression Intensity/ RPKM/FPKM/Counts
RRBP1	-0,712	1,27E-29	2,14E-26	17346,167
COL4A2	-0,562	2,22E-17	1,68E-14	101539,554
TCOF1	-0,552	4,5E-20	4,01E-17	4807,877
NEFH	-0,529	1,23E-16	8,89E-14	7228,221
ANKRD11	-0,496	1,76E-12	8,87E-10	3071,748
HSPA6	-0,453	1,35E-08	0,000004	95,898
MYH11	-0,449	3,93E-08	1,03E-05	217,414
ZC3H13	-0,439	1,43E-09	5,05E-07	1236,142
COL6A2	-0,42	1,2E-09	4,34E-07	23194,523
COL18A1	-0,408	5,37E-13	2,81E-10	11514,743
COL5A1	-0,404	3,59E-14	2,01E-11	48986,554
MT-ND3	0,401	3,92E-10	1,52E-07	10070,682
CLDN4	0,403	0,000000326	6,49E-05	92,933
GABRE	0,406	0,000000483	9,13E-05	223,069
EFNA1	0,409	0,000000464	8,89E-05	111,705
NPPB	0,412	0,000000163	3,48E-05	79,881
SFPQ	0,416	1,87E-09	6,39E-07	814,879
ALOXE3	0,425	4,04E-08	1,04E-05	81,905
GATA2	0,428	0,000000093	2,18E-05	241,244
GUSBP11	0,429	0,000000119	2,71E-05	115,591
NGFR	0,447	2,55E-08	6,9E-06	106,589
SMPD4BP	0,452	4,12E-09	1,3E-06	426,152
PTGES	0,46	1,16E-10	4,74E-08	55,23
SNAPC1	0,468	1,94E-15	1,18E-12	2372,407
CDKN1C	0,474	2,25E-09	7,39E-07	95,31
SNHG12	0,484	7,84E-12	3,6E-09	661,997
MALAT1	0,514	1,74E-16	1,2E-13	1517,625
MT-RNR1	0,533	2,24E-19	1,88E-16	18332,609
VGF	0,562	6,33E-12	3E-09	222,706
NFKBIZ	0,563	5,35E-16	3,52E-13	702,821
LRRC15	0,568	1,36E-15	8,57E-13	50,224
AQP3	0,581	2,23E-14	1,3E-11	565,99
CEACAM1	0,594	1,15E-13	6,21E-11	319,352
MT-ND6	0,634	3,58E-21	3,39E-18	7291,454
MT-RNR2	0,635	4,58E-27	6,3E-24	62175,649
MT-CYB	0,678	6,79E-25	7,34E-22	42271,751
MT-ND2	0,684	1,06E-25	1,24E-22	20871,69
MT-ND5	0,689	8,45E-27	1,07E-23	26681,602
MT-ATP8	0,705	6,52E-23	6,58E-20	4193,276
MT-CO3	0,707	1,13E-28	1,7E-25	74115,012
ARC	0,709	1,75E-18	1,4E-15	276,548
MT-ND4L	0,75	1,2E-30	2,27E-27	9208,525
MT-ATP6	0,755	1,13E-30	2,27E-27	31927,478
MT-CO2	0,797	6,25E-37	1,58E-33	61556,656
MT-CO1	0,798	1,36E-39	5,13E-36	122151,616
MT-ND1	0,824	1,73E-38	5,23E-35	19306,562
MT-ND4	0,829	4,71E-40	2,37E-36	93881,132
AQP1	1,117	8,86E-43	6,71E-39	203,932
MEOX2	5,82	0	0	117011,156

Table 24: Top 50 *MEOX2* correlating genes taken from TCGA.

Symbol	Expression Log Ratio	Expression p-value	Expression False Discovery Rate (q-value)
GMO	0,772	3,75E-29	7,47E-25
VAV3	0,743	5,53E-26	5,51E-22
ETV4	0,721	7,21E-24	4,79E-20
ELOVL2	0,707	1,19E-22	5,93E-19
SPRY2	0,698	6,65E-22	2,65E-18
SPRY1	0,681	1,54E-20	5,10E-17
RHOJ	0,66	5,85E-19	1,66E-15
RAB34	0,654	1,45E-18	3,61E-15
ACSL3	0,649	3,34E-18	7,40E-15
PIPOX	0,647	4,13E-18	8,22E-15
EPHB4	0,647	4,59E-18	8,31E-15
DUSP6	0,646	5,27E-18	8,74E-15
LRATD1	0,643	7,79E-18	1,13E-14
SHROOM3	0,643	8,15E-18	1,13E-14
ETV5	0,643	8,49E-18	1,13E-14
SPRY4	0,629	6,59E-17	8,20E-14
CREB3L1	0,623	1,62E-16	1,90E-13
ADAM19	0,614	5,51E-16	5,94E-13
ANXA5	0,614	5,67E-16	5,94E-13
DMRTA2	0,611	8,13E-16	8,10E-13
CARMIL1	0,61	1,04E-15	9,64E-13
ARNTL	0,609	1,07E-15	9,64E-13
SPRED1	0,608	1,32E-15	1,14E-12
SLC27A3	0,605	1,84E-15	1,53E-12
IER5	0,598	4,76E-15	3,79E-12
EYA2	0,597	5,79E-15	4,42E-12
DENND2A	0,596	6,00E-15	4,42E-12
ZNF521	0,596	6,52E-15	4,64E-12
PDGFA	0,594	7,82E-15	5,20E-12
CPNE4	0,594	7,83E-15	5,20E-12
BCL2L12	0,594	8,10E-15	5,20E-12
FAM3C	0,592	1,12E-14	7,00E-12
DLC1	0,588	1,88E-14	1,14E-11
SPRED2	0,586	2,16E-14	1,26E-11
TLK1	0,584	3,03E-14	1,72E-11
DBX2	0,583	3,39E-14	1,88E-11
LHFPL6	0,578	5,84E-14	3,14E-11
CDCA7L	0,577	6,58E-14	3,39E-11
BLM	0,577	6,63E-14	3,39E-11
SLC2A10	0,574	9,55E-14	4,75E-11
EPHA2	0,572	1,21E-13	5,87E-11
ZFHX4-AS1	0,568	1,95E-13	9,26E-11
SLC2A4RG	0,567	2,27E-13	1,05E-10
CAMK2D	0,567	2,33E-13	1,05E-10
TNN	0,567	2,37E-13	1,05E-10
THSD1	0,566	2,53E-13	1,08E-10
TGIF1	0,566	2,56E-13	1,08E-10
ADGRE5	0,564	3,19E-13	1,32E-10
MEIS1	0,563	3,52E-13	1,42E-10
CDH6	0,563	3,56E-13	1,42E-10

8 Contributions

Mall Lab: Dr. Moritz Mall, Elisa Heinzelmann

Massspectrometry Core Facility at DKFZ

Light Microscopy Core Facility at DKFZ

Plass Lab: Dr. Dieter Weichenhan, Marion Bähr

Turcan Lab: Dr. Sevin Turcan, PhD, Dr. Ashwin Narayanan, PhD, Bianca Steffl

9 Acknowledgments

First, I would like to thank Prof. Dr. Wolfgang Wick for the opportunity to persue my PhD project as a member of the Clinical Cooperation Unit Neurooncology of DKFZ and Heidelberg University Hospital.

I want to sincerely thank my direct supervisor and group leader Dr. Sevin Turcan, PhD for the endless support throughout the years. Thank you for the scientific supervision, the continuous interest in my project and the trust in me and my work. I am incredibly grateful for the enjoyable working atmosphere and the continuous support and room for growth I was given at all times. Thank you! I want to thank Prof. Dr. Stefan Wiemann for his scientific interest and valuable feedback for my project during our Thesis Advisory Commitee meetings, and for the time spent in reading this thesis and evaluating my dissertation and thesis defence as first examiner. I also want to thank Prof. Dr. Carmen Ruiz de Almodóvar for scientific advice and participation in our Thesis Advisory Committee meetings. I want to thank Prof. Dr. Peter Angel and Prof. Dr. Benedikt Brors for their participation in my thesis defense. I am also extremely thankful for the admission to the Helmholtz International Graduate School for Cancer Research. Thank you for the excellent training. I would also like to thank our collaborators at DKFZ and former and current Clinical Coorperation Unit members for their support. Thank you to Dr. Moritz Mall and Elisa Heinzelmann for your interest in the project and your contributions to further elucidate MEOX2's function in organoids. Thank you, Prof. Dr. Christoph Plass, for the opportunity, and Dr. Dieter Weichenhan for the scientific and technical guidance to perform ACT-seq in your lab. Also, thank you to the Light Microscopy Core Facility and the Massspectrometry Core Facility at DKFZ for training and collaboration.

A big thank you goes to current and former lab members of the Turcan Lab and our second-floor colleagues at the National Center for Tumor Diseases, that provided scientific and moral support throughout the last four years. Special thanks go to Dr. Sevin Turcan and Dr. Ashwin Narayanan for help and company during mouse surgeries and mouse farewells. Thank you, Bianca Steffl, for your outstanding technical support and for partaking in the seemingly never-ending Western Blot journey with me. Also thank you to Prof. Dr. Ricarda Diem for the opportunity and Kira Pichi for moral support for after-hours Western Blot fun at the Diem Lab. Lastly, I want to thank my family and my partner for their support throughout these years. Thank you, Julius, for your understanding and endless support throughout this whole journey.

10 Bibliography

Armas-López, L., Piña-Sánchez, P., Arrieta, O., de Alba, E. G., Ortiz-Quintero, B., Santillán-Doherty, P., . . . Ávila-Moreno, F. (2017). Epigenomic study identifies a novel mesenchyme homeobox2-GLI1 transcription axis involved in cancer drug resistance, overall survival and therapy prognosis in lung cancer patients. *Oncotarget, 8*(40), 67056-67081. doi:10.18632/oncotarget.17715

Brabletz, T., Kalluri, R., Nieto, M. A., & Weinberg, R. A. (2018). EMT in cancer. *Nat Rev Cancer, 18*(2), 128-134. doi:10.1038/nrc.2017.118

Brat, D. J., Aldape, K., Colman, H., Figrarella-Branger, D., Fuller, G. N., Giannini, C., . . . Weller, M. (2020). cIMPACT-NOW update 5: recommended grading criteria and terminologies for IDH-mutant astrocytomas. *Acta Neuropathol, 139*(3), 603-608. doi:10.1007/s00401-020-02127-9

Brennan, C. W., Verhaak, R. G., McKenna, A., Campos, B., Noushmehr, H., Salama, S. R., . . . Chin, L. (2013). The somatic genomic landscape of glioblastoma. *Cell, 155*(2), 462-477. doi:10.1016/j.cell.2013.09.034

Cai, R., Wang, P., Zhao, X., Lu, X., Deng, R., Wang, X., . . . Lin, J. (2020). LTBP1 promotes esophageal squamous cell carcinoma progression through epithelial-mesenchymal transition and cancer-associated fibroblasts transformation. *J Transl Med, 18*(1), 139. doi:10.1186/s12967-020-02310-2

Caja, L., Dituri, F., Mancarella, S., Caballero-Diaz, D., Moustakas, A., Giannelli, G., & Fabregat, I. (2018). TGF-β and the Tissue Microenvironment: Relevance in Fibrosis and Cancer. *Int J Mol Sci, 19*(5). doi:10.3390/ijms19051294

Candia, A. F., Kovalik, J. P., & Wright, C. V. (1993). Amino acid sequence of Mox-2 and comparison to its Xenopus and rat homologs. *Nucleic Acids Res, 21*(21), 4982. doi:10.1093/nar/21.21.4982

Carter, B., Ku, W. L., Kang, J. Y., Hu, G., Perrie, J., Tang, Q., & Zhao, K. (2019). Mapping histone modifications in low cell number and single cells using antibody-guided chromatin tagmentation (ACT-seq). *Nat Commun, 10*(1), 3747. doi:10.1038/s41467-019-11559-1

Chan, J. Y., Ong, C. W., & Salto-Tellez, M. (2011). Overexpression of neurone glial-related cell adhesion molecule is an independent predictor of poor prognosis in advanced colorectal cancer. *Cancer Sci, 102*(10), 1855-1861. doi:10.1111/j.1349-7006.2011.02021.x

Chang, C. J., Chao, C. H., Xia, W., Yang, J. Y., Xiong, Y., Li, C. W., . . . Hung, M. C. (2011). p53 regulates epithelial-mesenchymal transition and stem cell properties through modulating miRNAs. *Nat Cell Biol, 13*(3), 317-323. doi:10.1038/ncb2173

Chen, C. Y., Chen, J., He, L., & Stiles, B. L. (2018). PTEN: Tumor Suppressor and Metabolic Regulator. *Front Endocrinol (Lausanne), 9*, 338. doi:10.3389/fendo.2018.00338

Chen, H., Xu, C., Jin, Q., & Liu, Z. (2014). S100 protein family in human cancer. *Am J Cancer Res, 4*(2), 89-115.

Chen, J., Huang, X., Halicka, D., Brodsky, S., Avram, A., Eskander, J., . . . Goligorsky, M. S. (2006). Contribution of p16INK4a and p21CIP1 pathways to induction of premature senescence of human endothelial cells: permissive role of p53. *Am J Physiol Heart Circ Physiol, 290*(4), H1575-1586. doi:10.1152/ajpheart.00364.2005

Chen, Q., Luo, W., Veach, R. A., Hickman, A. B., Wilson, M. H., & Dyda, F. (2020). Structural basis of seamless excision and specific targeting by piggyBac transposase. *Nat Commun, 11*(1), 3446. doi:10.1038/s41467-020-17128-1

Chen, X., Liu, X., Lang, H., Zhang, S., Luo, Y., & Zhang, J. (2015). S100 calcium-binding protein A6 promotes epithelial-mesenchymal transition through β-catenin in

pancreatic cancer cell line. *PLoS One, 10*(3), e0121319. doi:10.1371/journal.pone.0121319
Chicaybam, L., Barcelos, C., Peixoto, B., Carneiro, M., Limia, C. G., Redondo, P., . . . Bonamino, M. H. (2016). An Efficient Electroporation Protocol for the Genetic Modification of Mammalian Cells. *Front Bioeng Biotechnol, 4*, 99. doi:10.3389/fbioe.2016.00099
Clark-Lewis, I., Sanghera, J. S., & Pelech, S. L. (1991). Definition of a consensus sequence for peptide substrate recognition by p44mpk, the meiosis-activated myelin basic protein kinase. *J Biol Chem, 266*(23), 15180-15184.
Conacci-Sorrell, M., Kaplan, A., Raveh, S., Gavert, N., Sakurai, T., & Ben-Ze'ev, A. (2005). The shed ectodomain of Nr-CAM stimulates cell proliferation and motility, and confers cell transformation. *Cancer Res, 65*(24), 11605-11612. doi:10.1158/0008-5472.Can-05-2647
Costa, A., Kieffer, Y., Scholer-Dahirel, A., Pelon, F., Bourachot, B., Cardon, M., . . . Mechta-Grigoriou, F. (2018). Fibroblast Heterogeneity and Immunosuppressive Environment in Human Breast Cancer. *Cancer Cell, 33*(3), 463-479.e410. doi:10.1016/j.ccell.2018.01.011
Crespo, I., Vital, A. L., Gonzalez-Tablas, M., Patino Mdel, C., Otero, A., Lopes, M. C., . . . Tabernero, M. D. (2015). Molecular and Genomic Alterations in Glioblastoma Multiforme. *Am J Pathol, 185*(7), 1820-1833. doi:10.1016/j.ajpath.2015.02.023
Cross, S. S., Hamdy, F. C., Deloulme, J. C., & Rehman, I. (2005). Expression of S100 proteins in normal human tissues and common cancers using tissue microarrays: S100A6, S100A8, S100A9 and S100A11 are all overexpressed in common cancers. *Histopathology, 46*(3), 256-269. doi:10.1111/j.1365-2559.2005.02097.x
de Vries, N. A., Buckle, T., Zhao, J., Beijnen, J. H., Schellens, J. H., & van Tellingen, O. (2012). Restricted brain penetration of the tyrosine kinase inhibitor erlotinib due to the drug transporters P-gp and BCRP. *Invest New Drugs, 30*(2), 443-449. doi:10.1007/s10637-010-9569-1
Derynck, R., & Zhang, Y. E. (2003). Smad-dependent and Smad-independent pathways in TGF-beta family signalling. *Nature, 425*(6958), 577-584. doi:10.1038/nature02006
Diaz, R. J., Ali, S., Qadir, M. G., De La Fuente, M. I., Ivan, M. E., & Komotar, R. J. (2017). The role of bevacizumab in the treatment of glioblastoma. *J Neurooncol, 133*(3), 455-467. doi:10.1007/s11060-017-2477-x
Donato, R., Sorci, G., & Giambanco, I. (2017). S100A6 protein: functional roles. *Cell Mol Life Sci, 74*(15), 2749-2760. doi:10.1007/s00018-017-2526-9
Dong, Z. Q., Guo, Z. Y., & Xie, J. (2019). The lncRNA EGFR-AS1 is linked to migration, invasion and apoptosis in glioma cells by targeting miR-133b/RACK1. *Biomed Pharmacother, 118*, 109292. doi:10.1016/j.biopha.2019.109292
Douville, J. M., Cheung, D. Y., Herbert, K. L., Moffatt, T., & Wigle, J. T. (2011). Mechanisms of MEOX1 and MEOX2 regulation of the cyclin dependent kinase inhibitors p21 and p16 in vascular endothelial cells. *PLoS One, 6*(12), e29099. doi:10.1371/journal.pone.0029099
Drabsch, Y., & ten Dijke, P. (2012). TGF-β signalling and its role in cancer progression and metastasis. *Cancer Metastasis Rev, 31*(3-4), 553-568. doi:10.1007/s10555-012-9375-7
Eble, J. A., & Niland, S. (2019). The extracellular matrix in tumor progression and metastasis. *Clin Exp Metastasis, 36*(3), 171-198. doi:10.1007/s10585-019-09966-1
Farooqi, A. A., & Siddik, Z. H. (2015). Platelet-derived growth factor (PDGF) signalling in cancer: rapidly emerging signalling landscape. *Cell Biochem Funct, 33*(5), 257-265. doi:10.1002/cbf.3120
Fujisawa, H., Reis, R. M., Nakamura, M., Colella, S., Yonekawa, Y., Kleihues, P., & Ohgaki, H. (2000). Loss of heterozygosity on chromosome 10 is more extensive in primary (de

novo) than in secondary glioblastomas. *Lab Invest, 80*(1), 65-72. doi:10.1038/labinvest.3780009
Gonzalez, F. A., Raden, D. L., & Davis, R. J. (1991). Identification of substrate recognition determinants for human ERK1 and ERK2 protein kinases. *J Biol Chem, 266*(33), 22159-22163.
Gorski, D. H., LePage, D. F., Patel, C. V., Copeland, N. G., Jenkins, N. A., & Walsh, K. (1993). Molecular cloning of a diverged homeobox gene that is rapidly down-regulated during the G0/G1 transition in vascular smooth muscle cells. *Mol Cell Biol, 13*(6), 3722-3733. doi:10.1128/mcb.13.6.3722
Grande, M. A., van der Kraan, I., de Jong, L., & van Driel, R. (1997). Nuclear distribution of transcription factors in relation to sites of transcription and RNA polymerase II. *J Cell Sci, 110 (Pt 15)*, 1781-1791.
Grigoriou, M., Kastrinaki, M. C., Modi, W. S., Theodorakis, K., Mankoo, B., Pachnis, V., & Karagogeos, D. (1995). Isolation of the human MOX2 homeobox gene and localization to chromosome 7p22.1-p21.3. *Genomics, 26*(3), 550-555. doi:10.1016/0888-7543(95)80174-k
Grumet, M. (1997). Nr-CAM: a cell adhesion molecule with ligand and receptor functions. *Cell Tissue Res, 290*(2), 423-428. doi:10.1007/s004410050949
Haas-Kogan, D. A., Prados, M. D., Tihan, T., Eberhard, D. A., Jelluma, N., Arvold, N. D., . . . Stokoe, D. (2005). Epidermal growth factor receptor, protein kinase B/Akt, and glioma response to erlotinib. *J Natl Cancer Inst, 97*(12), 880-887. doi:10.1093/jnci/dji161
Hanahan, D., & Weinberg, R. A. (2011). Hallmarks of cancer: the next generation. *Cell, 144*(5), 646-674. doi:10.1016/j.cell.2011.02.013
Heessen, S., & Fornerod, M. (2007). The inner nuclear envelope as a transcription factor resting place. *EMBO Rep, 8*(10), 914-919. doi:10.1038/sj.embor.7401075
Holmberg, C. I., Tran, S. E., Eriksson, J. E., & Sistonen, L. (2002). Multisite phosphorylation provides sophisticated regulation of transcription factors. *Trends Biochem Sci, 27*(12), 619-627. doi:10.1016/s0968-0004(02)02207-7
Hu, C. T., Wu, J. R., Chang, T. Y., Cheng, C. C., & Wu, W. S. (2008). The transcriptional factor Snail simultaneously triggers cell cycle arrest and migration of human hepatoma HepG2. *J Biomed Sci, 15*(3), 343-355. doi:10.1007/s11373-007-9230-y
Hua, H., Kong, Q., Zhang, H., Wang, J., Luo, T., & Jiang, Y. (2019). Targeting mTOR for cancer therapy. *J Hematol Oncol, 12*(1), 71. doi:10.1186/s13045-019-0754-1
Hua, W., ten Dijke, P., Kostidis, S., Giera, M., & Hornsveld, M. (2020). TGFβ-induced metabolic reprogramming during epithelial-to-mesenchymal transition in cancer. *Cellular and Molecular Life Sciences, 77*(11), 2103-2123. doi:10.1007/s00018-019-03398-6
Ito, Y., Yoshida, H., Tomoda, C., Uruno, T., Miya, A., Kobayashi, K., . . . Miyauchi, A. (2005). Expression of S100A2 and S100A6 in thyroid carcinomas. *Histopathology, 46*(5), 569-575. doi:10.1111/j.1365-2559.2005.02137.x
Jiao, Y., Killela, P. J., Reitman, Z. J., Rasheed, A. B., Heaphy, C. M., de Wilde, R. F., . . . Yan, H. (2012). Frequent ATRX, CIC, FUBP1 and IDH1 mutations refine the classification of malignant gliomas. *Oncotarget, 3*(7), 709-722. doi:10.18632/oncotarget.588
Jin, J. Z., & Ding, J. (2006). Analysis of Meox-2 mutant mice reveals a novel postfusion-based cleft palate. *Dev Dyn, 235*(2), 539-546. doi:10.1002/dvdy.20641
Kalluri, R., & Weinberg, R. A. (2009). The basics of epithelial-mesenchymal transition. *J Clin Invest, 119*(6), 1420-1428. doi:10.1172/jci39104

Kim, T. Y., Park, J. K., Prasad Aryal, Y., Lee, E. S., Neupane, S., Sung, S., . . . Kim, J. Y. (2020). Facilitation of Bone Healing Processes Based on the Developmental Function of Meox2 in Tooth Loss Lesion. *Int J Mol Sci, 21*(22). doi:10.3390/ijms21228701

Kocabayoglu, P., & Friedman, S. L. (2013). Cellular basis of hepatic fibrosis and its role in inflammation and cancer. *Front Biosci (Schol Ed), 5*, 217-230. doi:10.2741/s368

Le Rhun, E., Preusser, M., Roth, P., Reardon, D. A., van den Bent, M., Wen, P., . . . Weller, M. (2019). Molecular targeted therapy of glioblastoma. *Cancer Treat Rev, 80*, 101896. doi:10.1016/j.ctrv.2019.101896

Lin, J., Friesen, M. T., Bocangel, P., Cheung, D., Rawszer, K., & Wigle, J. T. (2005). Characterization of Mesenchyme Homeobox 2 (MEOX2) transcription factor binding to RING finger protein 10. *Molecular and Cellular Biochemistry, 275*(1), 75-84. doi:10.1007/s11010-005-0823-3

Ling, X. H., Fu, H., Chen, Z. Y., Lu, J. M., Zhuo, Y. J., Chen, J. H., . . . Jia, Z. (2019). miR-505 suppresses prostate cancer progression by targeting NRCAM. *Oncol Rep, 42*(3), 991-1004. doi:10.3892/or.2019.7231

Liu, Y., Li, X., Zhang, Y., Wang, H., Rong, X., Peng, J., . . . Peng, Y. (2019). An miR-340-5p-macrophage feedback loop modulates the progression and tumor microenvironment of glioblastoma multiforme. *Oncogene, 38*(49), 7399-7415. doi:10.1038/s41388-019-0952-x

Lobbous, M., Bernstock, J. D., Coffee, E., Friedman, G. K., Metrock, L. K., Chagoya, G., . . . Nabors, L. B. (2020). An Update on Neurofibromatosis Type 1-Associated Gliomas. *Cancers (Basel), 12*(1). doi:10.3390/cancers12010114

Lopez-Gines, C., Cerda-Nicolas, M., Gil-Benso, R., Pellin, A., Lopez-Guerrero, J. A., Callaghan, R., . . . Barbera, J. (2005). Association of chromosome 7, chromosome 10 and EGFR gene amplification in glioblastoma multiforme. *Clin Neuropathol, 24*(5), 209-218.

Louis, D. N., Perry, A., Reifenberger, G., von Deimling, A., Figarella-Branger, D., Cavenee, W. K., . . . Ellison, D. W. (2016). The 2016 World Health Organization Classification of Tumors of the Central Nervous System: a summary. *Acta Neuropathol, 131*(6), 803-820. doi:10.1007/s00401-016-1545-1

Lyu, X. J., Li, H. Z., Ma, X., Li, X. T., Gao, Y., Ni, D., . . . Zhang, X. (2015). Elevated S100A6 (Calcyclin) enhances tumorigenesis and suppresses CXCL14-induced apoptosis in clear cell renal cell carcinoma. *Oncotarget, 6*(9), 6656-6669. doi:10.18632/oncotarget.3169

Mankoo, B. S., Collins, N. S., Ashby, P., Grigorieva, E., Pevny, L. H., Candia, A., . . . Pachnis, V. (1999). Mox2 is a component of the genetic hierarchy controlling limb muscle development. *Nature, 400*(6739), 69-73. doi:10.1038/21892

Masui, K., Tanaka, K., Ikegami, S., Villa, G. R., Yang, H., Yong, W. H., . . . Mischel, P. S. (2015). Glucose-dependent acetylation of Rictor promotes targeted cancer therapy resistance. *Proc Natl Acad Sci U S A, 112*(30), 9406-9411. doi:10.1073/pnas.1511759112

Matsuzaki, K. (2011). Smad phosphoisoform signaling specificity: the right place at the right time. *Carcinogenesis, 32*(11), 1578-1588. doi:10.1093/carcin/bgr172

McCubrey, J. A., Steelman, L. S., Chappell, W. H., Abrams, S. L., Wong, E. W., Chang, F., . . . Franklin, R. A. (2007). Roles of the Raf/MEK/ERK pathway in cell growth, malignant transformation and drug resistance. *Biochim Biophys Acta, 1773*(8), 1263-1284. doi:10.1016/j.bbamcr.2006.10.001

Mijit, M., Caracciolo, V., Melillo, A., Amicarelli, F., & Giordano, A. (2020). Role of p53 in the Regulation of Cellular Senescence. *Biomolecules, 10*(3). doi:10.3390/biom10030420

Montano, N., D'Alessandris, Q. G., Izzo, A., Fernandez, E., & Pallini, R. (2016). Biomarkers for glioblastoma multiforme: status quo. *J Clin Transl Res, 2*(1), 3-10.
Mori, K., Muto, Y., Kokuzawa, J., Yoshioka, T., Yoshimura, S., Iwama, T., . . . Sakai, N. (2004). Neuronal protein NP25 interacts with F-actin. *Neurosci Res, 48*(4), 439-446. doi:10.1016/j.neures.2003.12.012
Narayanan, A., Blanco-Carmona, E., Demirdizen, E., Sun, X., Herold-Mende, C., Schlesner, M., & Turcan, S. (2020). Nuclei Isolation from Fresh Frozen Brain Tumors for Single-Nucleus RNA-seq and ATAC-seq. *J Vis Exp*(162). doi:10.3791/61542
Neftel, C., Laffy, J., Filbin, M. G., Hara, T., Shore, M. E., Rahme, G. J., . . . Suvà, M. L. (2019). An Integrative Model of Cellular States, Plasticity, and Genetics for Glioblastoma. *Cell, 178*(4), 835-849.e821. doi:10.1016/j.cell.2019.06.024
Nobusawa, S., Watanabe, T., Kleihues, P., & Ohgaki, H. (2009). IDH1 mutations as molecular signature and predictive factor of secondary glioblastomas. *Clin Cancer Res, 15*(19), 6002-6007. doi:10.1158/1078-0432.Ccr-09-0715
Noizet, M., Lagoutte, E., Gratigny, M., Bouschbacher, M., Lazareth, I., Roest Crollius, H., . . . Dugast-Darzacq, C. (2016). Master regulators in primary skin fibroblast fate reprogramming in a human ex vivo model of chronic wounds. *Wound Repair Regen, 24*(2), 247-262. doi:10.1111/wrr.12392
Ohgaki, H., Dessen, P., Jourde, B., Horstmann, S., Nishikawa, T., Di Patre, P. L., . . . Kleihues, P. (2004). Genetic pathways to glioblastoma: a population-based study. *Cancer Res, 64*(19), 6892-6899. doi:10.1158/0008-5472.Can-04-1337
Ohgaki, H., & Kleihues, P. (2013). The definition of primary and secondary glioblastoma. *Clin Cancer Res, 19*(4), 764-772. doi:10.1158/1078-0432.Ccr-12-3002
Pearson, J. R. D., & Regad, T. (2017). Targeting cellular pathways in glioblastoma multiforme. *Signal Transduct Target Ther, 2*, 17040. doi:10.1038/sigtrans.2017.40
Philpott, C., Tovell, H., Frayling, I. M., Cooper, D. N., & Upadhyaya, M. (2017). The NF1 somatic mutational landscape in sporadic human cancers. *Hum Genomics, 11*(1), 13. doi:10.1186/s40246-017-0109-3
Quinn, L. M., Latham, S. E., & Kalionis, B. (2000). The homeobox genes MSX2 and MOX2 are candidates for regulating epithelial-mesenchymal cell interactions in the human placenta. *Placenta, 21 Suppl A*, S50-54. doi:10.1053/plac.1999.0514
Rasmussen, B. K., Hansen, S., Laursen, R. J., Kosteljanetz, M., Schultz, H., Nørgård, B. M., . . . Gradel, K. O. (2017). Epidemiology of glioma: clinical characteristics, symptoms, and predictors of glioma patients grade I-IV in the the Danish Neuro-Oncology Registry. *J Neurooncol, 135*(3), 571-579. doi:10.1007/s11060-017-2607-5
Ratié, L., Ware, M., Jagline, H., David, V., & Dupé, V. (2014). Dynamic expression of Notch-dependent neurogenic markers in the chick embryonic nervous system. *Front Neuroanat, 8*, 158. doi:10.3389/fnana.2014.00158
Regad, T. (2015). Targeting RTK Signaling Pathways in Cancer. *Cancers (Basel), 7*(3), 1758-1784. doi:10.3390/cancers7030860
Reifenberger, G., Wirsching, H. G., Knobbe-Thomsen, C. B., & Weller, M. (2017). Advances in the molecular genetics of gliomas - implications for classification and therapy. *Nat Rev Clin Oncol, 14*(7), 434-452. doi:10.1038/nrclinonc.2016.204
Robertson, I. B., & Rifkin, D. B. (2016). Regulation of the Bioavailability of TGF-β and TGF-β-Related Proteins. *Cold Spring Harb Perspect Biol, 8*(6). doi:10.1101/cshperspect.a021907
Saadeh, F. S., Mahfouz, R., & Assi, H. I. (2018). EGFR as a clinical marker in glioblastomas and other gliomas. *Int J Biol Markers, 33*(1), 22-32. doi:10.5301/ijbm.5000301
Sakurai, T. (2012). The role of NrCAM in neural development and disorders--beyond a simple glue in the brain. *Mol Cell Neurosci, 49*(3), 351-363. doi:10.1016/j.mcn.2011.12.002

Santarpia, L., Lippman, S. M., & El-Naggar, A. K. (2012). Targeting the MAPK-RAS-RAF signaling pathway in cancer therapy. *Expert Opin Ther Targets, 16*(1), 103-119. doi:10.1517/14728222.2011.645805

Sarbassov, D. D., Guertin, D. A., Ali, S. M., & Sabatini, D. M. (2005). Phosphorylation and regulation of Akt/PKB by the rictor-mTOR complex. *Science, 307*(5712), 1098-1101. doi:10.1126/science.1106148

Schmidt, F., Fischer, J., Herrlinger, U., Dietz, K., Dichgans, J., & Weller, M. (2006). PCV chemotherapy for recurrent glioblastoma. *Neurology, 66*(4), 587-589. doi:10.1212/01.wnl.0000197792.73656.c2

Schneider-Poetsch, T., Ju, J., Eyler, D. E., Dang, Y., Bhat, S., Merrick, W. C., . . . Liu, J. O. (2010). Inhibition of eukaryotic translation elongation by cycloheximide and lactimidomycin. *Nat Chem Biol, 6*(3), 209-217. doi:10.1038/nchembio.304

Sharpless, N. E., & Sherr, C. J. (2015). Forging a signature of in vivo senescence. *Nat Rev Cancer, 15*(7), 397-408. doi:10.1038/nrc3960

Sigismund, S., Avanzato, D., & Lanzetti, L. (2018). Emerging functions of the EGFR in cancer. *Mol Oncol, 12*(1), 3-20. doi:10.1002/1878-0261.12155

Sizemore, G. M., Pitarresi, J. R., Balakrishnan, S., & Ostrowski, M. C. (2017). The ETS family of oncogenic transcription factors in solid tumours. *Nat Rev Cancer, 17*(6), 337-351. doi:10.1038/nrc.2017.20

Skopicki, H. A., Lyons, G. E., Schatteman, G., Smith, R. C., Andrés, V., Schirm, S., . . . Walsh, K. (1997). Embryonic expression of the Gax homeodomain protein in cardiac, smooth, and skeletal muscle. *Circ Res, 80*(4), 452-462. doi:10.1161/01.res.80.4.452

Smith, R. C., Branellec, D., Gorski, D. H., Guo, K., Perlman, H., Dedieu, J. F., . . . Walsh, K. (1997). p21CIP1-mediated inhibition of cell proliferation by overexpression of the gax homeodomain gene. *Genes Dev, 11*(13), 1674-1689. doi:10.1101/gad.11.13.1674

Stupp, R., Mason, W. P., van den Bent, M. J., Weller, M., Fisher, B., Taphoorn, M. J., . . . Mirimanoff, R. O. (2005). Radiotherapy plus concomitant and adjuvant temozolomide for glioblastoma. *N Engl J Med, 352*(10), 987-996. doi:10.1056/NEJMoa043330

Sullivan, K. D., Galbraith, M. D., Andrysik, Z., & Espinosa, J. M. (2018). Mechanisms of transcriptional regulation by p53. *Cell Death Differ, 25*(1), 133-143. doi:10.1038/cdd.2017.174

Tachon, G., Masliantsev, K., Rivet, P., Petropoulos, C., Godet, J., Milin, S., . . . Karayan-Tapon, L. (2019). Prognostic significance of MEOX2 in gliomas. *Mod Pathol, 32*(6), 774-786. doi:10.1038/s41379-018-0192-6

Tamai, H., Miyake, K., Yamaguchi, H., Shimada, T., Dan, K., & Inokuchi, K. (2014). Inhibition of S100A6 induces GVL effects in MLL/AF4-positive ALL in human PBMC-SCID mice. *Bone Marrow Transplant, 49*(5), 699-703. doi:10.1038/bmt.2014.18

Tamai, H., Miyake, K., Yamaguchi, H., Takatori, M., Dan, K., Inokuchi, K., & Shimada, T. (2012). AAV8 vector expressing IL24 efficiently suppresses tumor growth mediated by specific mechanisms in MLL/AF4-positive ALL model mice. *Blood, 119*(1), 64-71. doi:10.1182/blood-2011-05-354050

Tang, Q., & Hann, S. S. (2018). HOTAIR: An Oncogenic Long Non-Coding RNA in Human Cancer. *Cell Physiol Biochem, 47*(3), 893-913. doi:10.1159/000490131

Terzi, M. Y., Izmirli, M., & Gogebakan, B. (2016). The cell fate: senescence or quiescence. *Mol Biol Rep, 43*(11), 1213-1220. doi:10.1007/s11033-016-4065-0

Tian, L., Tao, Z. Z., Ye, H. P., Li, G. Y., Zhan, Z. F., & Tuo, H. W. (2018). Over-expression of MEOX2 promotes apoptosis through inhibiting the PI3K/Akt pathway in laryngeal cancer cells. *Neoplasma, 65*(5), 745-752. doi:10.4149/neo_2018_171218N824

Tomczak, K., Czerwińska, P., & Wiznerowicz, M. (2015). The Cancer Genome Atlas (TCGA): an immeasurable source of knowledge. *Contemp Oncol (Pozn), 19*(1a), A68-77. doi:10.5114/wo.2014.47136

Tuncel, G., & Kalkan, R. (2018). Receptor tyrosine kinase-Ras-PI 3 kinase-Akt signaling network in glioblastoma multiforme. *Med Oncol, 35*(9), 122. doi:10.1007/s12032-018-1185-5

Turcan, S., Makarov, V., Taranda, J., Wang, Y., Fabius, A. W. M., Wu, W., . . . Chan, T. A. (2018). Mutant-IDH1-dependent chromatin state reprogramming, reversibility, and persistence. *Nat Genet, 50*(1), 62-72. doi:10.1038/s41588-017-0001-z

Uhlén, M., Fagerberg, L., Hallström, B. M., Lindskog, C., Oksvold, P., Mardinoglu, A., . . . Pontén, F. (2015). Proteomics. Tissue-based map of the human proteome. *Science, 347*(6220), 1260419. doi:10.1126/science.1260419

Valcourt, U., Thuault, S., Pardali, K., Heldin, C. H., & Moustakas, A. (2007). Functional role of Meox2 during the epithelial cytostatic response to TGF-beta. *Mol Oncol, 1*(1), 55-71. doi:10.1016/j.molonc.2007.02.002

Vandromme, M., Gauthier-Rouvière, C., Lamb, N., & Fernandez, A. (1996). Regulation of transcription factor localization: fine-tuning of gene expression. *Trends Biochem Sci, 21*(2), 59-64.

Vega, S., Morales, A. V., Ocaña, O. H., Valdés, F., Fabregat, I., & Nieto, M. A. (2004). Snail blocks the cell cycle and confers resistance to cell death. *Genes Dev, 18*(10), 1131-1143. doi:10.1101/gad.294104

Wang, A., Bao, Y., Wu, Z., Zhao, T., Wang, D., Shi, J., . . . Qu, L. (2019). Long noncoding RNA EGFR-AS1 promotes cell growth and metastasis via affecting HuR mediated mRNA stability of EGFR in renal cancer. *Cell Death Dis, 10*(3), 154. doi:10.1038/s41419-019-1331-9

Wang, A., Jiang, A., Gan, X., Wang, Z., Huang, J., Dong, K., . . . Chen, M. (2020). EGFR-AS1 Promotes Bladder Cancer Progression by Upregulating EGFR. *Biomed Res Int, 2020*, 6665974. doi:10.1155/2020/6665974

Wang, J., Liang, W. J., Min, G. T., Wang, H. P., Chen, W., & Yao, N. (2018). LTBP2 promotes the migration and invasion of gastric cancer cells and predicts poor outcome of patients with gastric cancer. *Int J Oncol, 52*(6), 1886-1898. doi:10.3892/ijo.2018.4356

Weller, M., van den Bent, M., Preusser, M., Le Rhun, E., Tonn, J. C., Minniti, G., . . . Wick, W. (2021). EANO guidelines on the diagnosis and treatment of diffuse gliomas of adulthood. *Nat Rev Clin Oncol, 18*(3), 170-186. doi:10.1038/s41571-020-00447-z

Weller, M., Wick, W., Aldape, K., Brada, M., Berger, M., Pfister, S. M., . . . Reifenberger, G. (2015). Glioma. *Nat Rev Dis Primers, 1*, 15017. doi:10.1038/nrdp.2015.17

Wen, P. Y., & Kesari, S. (2008). Malignant gliomas in adults. *N Engl J Med, 359*(5), 492-507. doi:10.1056/NEJMra0708126

Westphal, M., Maire, C. L., & Lamszus, K. (2017). EGFR as a Target for Glioblastoma Treatment: An Unfulfilled Promise. *CNS Drugs, 31*(9), 723-735. doi:10.1007/s40263-017-0456-6

Worby, C. A., & Dixon, J. E. (2014). PTEN. *Annu Rev Biochem, 83*, 641-669. doi:10.1146/annurev-biochem-082411-113907

Yan, H., Parsons, D. W., Jin, G., McLendon, R., Rasheed, B. A., Yuan, W., . . . Bigner, D. D. (2009). IDH1 and IDH2 mutations in gliomas. *N Engl J Med, 360*(8), 765-773. doi:10.1056/NEJMoa0808710

Yeh, P. Y., Chuang, S. E., Yeh, K. H., Song, Y. C., Chang, L. L., & Cheng, A. L. (2004). Phosphorylation of p53 on Thr55 by ERK2 is necessary for doxorubicin-induced p53 activation and cell death. *Oncogene, 23*(20), 3580-3588. doi:10.1038/sj.onc.1207426

Yin, H., He, H., Cao, X., Shen, X., Han, S., Cui, C., . . . Zhu, Q. (2020). MiR-148a-3p Regulates Skeletal Muscle Satellite Cell Differentiation and Apoptosis via the PI3K/AKT Signaling Pathway by Targeting Meox2. *Front Genet, 11*, 512. doi:10.3389/fgene.2020.00512

Zhang, Y., Sui, F., Ma, J., Ren, X., Guan, H., Yang, Q., . . . Hou, P. (2017). Positive Feedback Loops Between NrCAM and Major Signaling Pathways Contribute to Thyroid Tumorigenesis. *J Clin Endocrinol Metab, 102*(2), 613-624. doi:10.1210/jc.2016-1677

Zhao, M., Wang, K. J., Tan, Z., Zheng, C. M., Liang, Z., & Zhao, J. Q. (2016). Identification of potential therapeutic targets for papillary thyroid carcinoma by bioinformatics analysis. *Oncol Lett, 11*(1), 51-58. doi:10.3892/ol.2015.3829

Zhao, Z., Zhang, K. N., Wang, Q., Li, G., Zeng, F., Zhang, Y., . . . Jiang, T. (2021). Chinese Glioma Genome Atlas (CGGA): A Comprehensive Resource with Functional Genomic Data from Chinese Gliomas. *Genomics Proteomics Bioinformatics*. doi:10.1016/j.gpb.2020.10.005

Zhou, X., Ren, Y., Zhang, J., Zhang, C., Zhang, K., Han, L., . . . Kang, C. (2015). HOTAIR is a therapeutic target in glioblastoma. *Oncotarget, 6*(10), 8353-8365. doi:10.18632/oncotarget.3229